

Ab-initio investigation of the interplay between the hyperfine interaction and complex magnetism at the nanoscale

Sufyan Rateb Saleem Shehada

Schlüsseltechnologien / Key Technologies Band / Volume 272 ISBN 978-3-95806-718-9



Forschungszentrum Jülich GmbH Peter Grünberg Institut (PGI) Quanten-Theorie der Materialien (PGI-1/IAS-1)

Ab-initio investigation of the interplay between the hyperfine interaction and complex magnetism at the nanoscale

Sufyan Rateb Saleem Shehada

Schriften des Forschungszentrums Jülich Reihe Schlüsseltechnologien / Key Technologies Bibliografische Information der Deutschen Nationalbibliothek. Die Deutsche Nationalbibliothek verzeichnet diese Publikation in der Deutschen Nationalbibliografie; detaillierte Bibliografische Daten sind im Internet über http://dnb.d-nb.de abrufbar.

Herausgeber Forschungszentrum Jülich GmbH

und Vertrieb: Zentralbibliothek, Verlag

52425 Jülich

Tel.: +49 2461 61-5368 Fax: +49 2461 61-6103 zb-publikation@fz-juelich.de

www.fz-juelich.de/zb

Umschlaggestaltung: Grafische Medien, Forschungszentrum Jülich GmbH

Druck: Grafische Medien, Forschungszentrum Jülich GmbH

Copyright: Forschungszentrum Jülich 2023

Schriften des Forschungszentrums Jülich Reihe Schlüsseltechnologien / Key Technologies, Band / Volume 272

D 82 (Diss. RWTH Aachen University, 2023)

ISSN 1866-1807 ISBN 978-3-95806-718-9

Vollständig frei verfügbar über das Publikationsportal des Forschungszentrums Jülich (JuSER) unter www.fz-juelich.de/zb/openaccess.



This is an Open Access publication distributed under the terms of the <u>Creative Commons Attribution License 4.0</u>, which permits unrestricted use, distribution, and reproduction in any medium, provided the original work is properly cited.

Abstract

Groundbreaking advances in quantum technologies have recently been achieved through the use of innovative scanning tunneling microscopy techniques that demonstrate nuclear magnetometry of single magnetic adatoms. The weak hyperfine interaction between the nuclear and electron spins is atomically resolved, representing a significant step towards realizing quantum devices based on well-shielded individual nuclear spins that are impervious to environmental disturbances. Such nuclear spins could represent an ideal realization of qubits constructed atom-by-atom on surfaces. Notably, these experimental works have so far only yielded successful measurements on the hyperfine interaction for a selection of few chemical species adsorbed on twolayer thick MgO deposited on a Ag surface. This represents a rather unexplored topic of interest to the broad quantum computational and experimental community aimed at exploring hyperfine interactions and nuclear spins to encode quantum information. To broaden the scope of this emergent topic, we present an extensive first-principles computational study of the hyperfine interaction of the complete series of 3d transition-metal adatoms deposited on diverse thicknesses of insulating thin films of experimental interest, including MgO, NaF, NaCl, h-BN, and Cu₂N films. The investigation identifies the atoms and substrates that trigger the most efficient hyperfine interactions and uncovers the relevant trends. Physical mechanisms are meticulously analyzed, and a valuable map of the hyperfine interactions that will guide corresponding experimental and theoretical communities is summarized.

Furthermore, we explore the correlation between the hyperfine interaction and the magnetic state of a multi-atomic nanostructure. We choose Fe dimers and investigate both cases: free-standing and deposited dimers on a bilayer of MgO(001), and compare them to the case of Fe single adatoms. Fe-adatom is a prototypical atom that carries a large hyperfine interaction with a minimal nuclear spin, offering several advantages over the rest of potential 3d transition metal atoms. Our findings indicate that the magnitude of the hyperfine interaction can be controlled by switching the magnetic state of the dimers. The antiferromagnetic state enhances the hyperfine interaction with respect to that of the ferromagnetic state for short Fe-Fe distances. A transition towards the opposite behavior is observed by increasing the distance between the magnetic atoms. Furthermore, we demonstrate the ability to substantially modify the hyperfine interaction by atomic control of the location of the adatoms on the substrate. Our results establish the limits of applicability of the usual hyperfine Hamiltonian, and therefore, we propose an extension based on multiple-scattering theory.

Designing systems with large magnetic anisotropy energy (MAE) is crucial for nanoscale magnetic devices since it defines the energy barrier that would protect a magnetic bit to flip its orientation. However, the MAE per atom in single-molecule magnets and ferromagnetic films remains typically one to two orders of magnitude below the theoretical limit imposed by the atomic spin-orbit interaction. Experimentally, the maximum MAE for a 3d transition metal atom was recently achieved by coordinating a single Co atom to the O site of a MgO(100) surface. Theoretically, conventional density functional theory (DFT) calculations do not recover the large MAE of this system. Here, including a Hubbard-U correction and spin-orbit coupling, we reproduce the large MAE of an individual Co adatom on a MgO (001) surface and unveil the underlying mechanism. More importantly, we take one step further by investigating the possibility of enhancing the MAE of 3d transition metal adatoms by considering various structural geometries of 3d-O molecules deposited on MgO. In one of the structures, where the molecules are perpendicular to the surface, the MAE can be enhanced while reducing the interaction with the substrate, which should minimize spin fluctuations and enhance the magnetic stability. Additionally, we provide evidence of the ability to substantially modify the MAE by atomic control of the 3d-O molecules location on the substrate and inspect the underlying hyperfine interactions.

Zusammenfassung

Bahnbrechende Fortschritte in der Quantentechnologie wurden kürzlich durch den Einsatz innovativer Rastertunnelmikroskopietechniken erzielt, die die Kernmagnetometrie einzelner magnetischer Adatome demonstrieren. Die schwache Hyperfeinwechselwirkung zwischen den Kern- und Elektronenspins wird atomar aufgelöst, was einen bedeutenden Schritt in Richtung der Realisierung von Quantengeräten darstellt, die auf gut abgeschirmten individuellen Kernspins basieren, die unempfindlich gegen Störungen aus der Umgebung sind. Solche Kernspins könnten eine ideale Realisierung von Qubits darstellen, die Atom für Atom auf Oberflächen aufgebaut sind. Bemerkenswerterweise haben diese experimentellen Arbeiten bisher nur erfolgreiche Messungen der Hyperfeinwechselwirkung für eine Auswahl einiger weniger chemischer Spezies erbracht, die auf zweischichtigem MgO adsorbiert sind, das auf einer Ag-Oberfläche abgeschieden wurde. Dies ist ein eher unerforschtes Thema, das für die breite Gemeinschaft der Quantencomputer und -experimentatoren von Interesse ist, die Hyperfeinwechselwirkungen und Kernspins zur Verschlüsselung von Quanteninformationen erforschen wollen. Um den Umfang dieses aufstrebenden Themas zu erweitern, präsentieren wir eine umfangreiche First-Principles-Rechenstudie der Hyperfeinwechselwirkung der kompletten Reihe von 3d Übergangsmetall-Atomen, die auf verschiedenen Dicken von isolierenden dünnen Filmen von experimentellem Interesse abgeschieden sind, einschließlich MgO, NaF, NaCl, h-BN und Cu₂N-Filmen. Die Untersuchung identifiziert die Atome und Substrate, die die effizientesten Hyperfeinwechselwirkungen auslösen, und deckt die relevanten Trends auf. Die physikalischen Mechanismen werden sorgfältig analysiert, und es wird eine wertvolle Karte der Hyperfeinwechselwirkungen erstellt, die den entsprechenden experimentellen und theoretischen Gemeinschaften als Leitfaden dienen wird.

Darüber hinaus untersuchen wir die Korrelation zwischen der Hyperfeinwechselwirkung und dem magnetischen Zustand einer mehratomigen Nanostruktur. Wir wählen Fe-Dimere und untersuchen beide Fälle: freistehende und abgeschiedene Dimere auf einer Doppelschicht aus MgO(001) und vergleichen sie mit dem Fall von Fe-Einzelatomen. Das Fe-Atom ist ein prototypisches Adatom, das eine große Hyperfeinwechselwirkung mit einem minimalen Kernspin aufweist, was mehrere Vorteile gegenüber dem Rest der potentiellen 3d-Übergangsmetallatome bietet. Unsere Ergebnisse zeigen, dass die Größe der Hyperfeinwechselwirkung durch Umschalten des magnetischen Zustands der Dimere gesteuert werden kann. Der antiferromagnetischen Zustand verstärkt die Hyperfeinwechselwirkung im Vergleich zum ferromagnetischen Zustand bei kurzen Fe-Fe-Abständen. Ein Übergang zum entgegengesetzten Verhalten wird beobachtet, wenn der Abstand zwischen den magnetischen Atomen ver-

größert wird. Darüber hinaus zeigen wir, dass die Hyperfeinwechselwirkung durch atomare Kontrolle der Position der Adatome auf dem Substrat erheblich verändert werden kann. Unsere Ergebnisse zeigen die Grenzen der Anwendbarkeit des üblichen Hyperfein-Hamiltonian auf und wir schlagen daher eine Erweiterung auf der Grundlage der Theorie der Vielfachstreuung.

Die Entwicklung von Systemen mit großer magnetischer Anisotropieenergie (MAE) ist für magnetische Geräte im Nanomaßstab von entscheidender Bedeutung, da sie die Energiebarriere definiert, die ein magnetisches Bit davor schützt, seine Ausrichtung zu ändern. Die MAE pro Atom in Einzelmolekülmagneten und ferromagnetischen Filmen liegt jedoch in der Regel ein bis zwei Größenordnungen unter der theoretischen Grenze, die durch die atomare Spin-Bahn-Wechselwirkung gesetzt wird. Experimentell wurde die maximale MAE für ein 3d-Übergangsmetallatom kürzlich durch die Koordinierung eines einzelnen Co-Atoms an die O-Stelle einer MgO(100)-Oberfläche erreicht Theoretische Berechnungen mit der konventionellen Dichtefunktionaltheorie (DFT) können die große MAE dieses Systems nicht reproduzieren. Unter Einbeziehung einer Hubbard-U-Korrektur und der Spin-Bahn-Kopplung reproduzieren wir hier die große MAE eines einzelnen Co-Atoms auf einer MgO(001)-Oberfläche und enthüllen ihren Mechanismus. Noch wichtiger ist, dass wir einen Schritt weiter gehen, indem wir die Möglichkeit untersuchen, die MAE von 3d-Übergangsmetall-Adatomen zu erhöhen, indem wir verschiedene strukturelle Geometrien von 3d-O-Molekülen betrachten, die auf MgO abgeschieden sind. Bei einer der Strukturen, bei der die Moleküle senkrecht zur Oberfläche stehen, kann die MAE verbessert werden, während die Wechselwirkung mit dem Substrat reduziert wird, was Spin-Fluktuationen minimieren und die magnetische Stabilität erhöhen sollte. Darüber hinaus weisen wir nach, dass sich die MAE durch atomare Kontrolle der Lage der 3d-O-Moleküle auf dem Substrat erheblich verändern lässt, und untersuchen die zugrunde liegenden Hyperfeinwechselwirkungen.

Acknowledgements

I am extremely grateful for the opportunity to have worked with Prof. Dr. Samir Lounis, who has been an exceptional mentor to me. I cannot thank him enough for always being willing to answer my questions and offering guidance whenever I needed it. His unwavering support has helped me believe in myself, and his encouragement has motivated me to push through any challenges I encountered during my work. It was an honor to be part of his team, and I am forever grateful for the knowledge and skills I gained through this experience.

I want to express my sincere gratitude to Prof. Dr. Markus Morgenstern for agreeing to be the second referee for my thesis. His dedication to the academic community and expertise in my field is truly an honor. I appreciate his valuable feedback and contributions to improving my work. Thank you, Prof. Dr. Morgenstern, for your invaluable support.

I would like to thank Prof. Dr. Stefan Blügel for giving me the opportunity to write my thesis at his institute, "Quantum Theory of Materials," located at the Peter Grünberg Institut and the Institute for Advanced Simulation. His steady support and encouragement have been instrumental in my scientific journey. Through stimulating discussions, he has deepened my understanding of solid-state physics and helped me to focus on the relevant aspects of the problems at hand.

Dr. Muayd AbuSaa is representative of the Arab American University Palestine and the Palestinian partner within the funding scheme of my thesis. I am deeply grateful for his support and expertise in this journey. This work was funded by the German Federal Ministry of Education and Research (BMBF) through the Palestinian German Scientific Bridge (PGSB), and I would like to express my sincere gratitude to them for their support. Without their funding, this research would not have been possible. Thank you all for your contributions to this project.

I am grateful to Dr. Manuel dos Santos Dias for his relentless support from the beginning of my work. His extensive knowledge, particularly in the theoretical background and programming, has greatly benefited my thesis. His contributions are invaluable and cannot be overstated. Moreover, I would like to thank Dr. Filipe Guimarães for enormous support and guidance at the start of the PhD. I extend my heartfelt gratitude to Dr. Juba Bouaziz for his invaluable help, support, and fruitful discussions throughout my research journey. And also I would like to thank the members of the Funsilab group.

I would like to extend a special thanks to Mrs. Ute Winkler for her outstanding administrative support. Her prompt and reliable assistance has been invaluable in helping me overcome any administrative issues. I cannot express enough how grateful I am for her consistent dedication and exceptional service. Thank you, Mrs. Winkler, for your incredible support!

I would like to express my deepest gratitude to my family for their unshakable support throughout my academic journey. Their love, encouragement, and belief in me have been a constant source of inspiration and motivation. I am truly blessed to have such a supportive family, who have always been there for me through thick and thin. Thank you for your unwavering support, which has made this accomplishment possible.

Contents

1.	Intro	oduction	1
2.	Den	sity Functional Theory	6
	2.1.	The Many-body Schrödinger Equation	6
	2.2.	Born-Oppenheimer Approximation	7
	2.3.	Hohenberg-Kohn Theorems	7
	2.4.	Kohn-Sham Formulation	8
	2.5.	Spin polarized DFT	9
	2.6.	Exchange and Correlation functionals	10
		2.6.1. Local spin density approximation (LSDA)	10
		2.6.2. Generalized gradient approximation (GGA)	11
		2.6.3. Hubbard U correction	11
	2.7.	Plane waves and Pseudopotentials	12
	2.8.	Spin-orbit coupling	14
	2.9.	The hyperfine interaction	14
	2.10.	Quantum ESPRESSO	15
3.	The	ory of the hyperfine interactions	17
•			17
	3.2.		19
		V 1	19
			21
		- v -	21
		3.2.4. Hyperfine Interaction Parameters	22
	3.3.	V ±	23
4.			24
	4.1.	Introduction	
	4.2.	Computational details	
	4.3.	Reference atomic calculations	
	4.4.	8-	29
	4.5.		
	4.6.	Adatoms on 1 layer of Cu2N and h–BN	
	4.7.	Discussion of the limitations of our simulations	
	4.8	Conclusion	40

5 .	Нур	erfine fields of Iron dimers	44
		Introduction	44
	5.2.	Computational details	45
	5.3.	Free-standing Fe dimers	47
	5.4.	Recap: Hyperfine interaction of a single Fe adatom on bilayer of MgO .	52
	5.5.		
	5.6.	Conclusion	
6.	Mag	gnetic Anisotropy Energy of 3d adatoms and 3d–O molecules on the	
	bilay	ver of MgO	58
	6.1.	Introduction	58
	6.2.	Computational details	60
	6.3.	MAE of a single Co adatom on the bilayer of MgO	61
	6.4.	Magnetic Anisotropy Energy of 3d adatoms and 3d–O molecules on	
		the bilayer of MgO	65
	6.5.	Hyperfine interactions	70
	6.6.	Conclusion	72
7.	Con	clusions	74
Α.	Арр	endix-chapter 4	79
В.	Арр	endix-chapter 5	84
C.	Арр	endix-chapter 6	90
D.	Indu	ced magnetization from multiple-scattering expansion	99
E.	List	of scientific contributions	101

List of Figures

1.1.	The hyperfine interaction studied by ESR in a scanning tunneling microscopy setup. (a) A schematic of the STM experimental set up showing different isotopes of single Fe atoms on a bilayer MgO film grown on Ag(001). (b) ESR spectra for different Fe isotopes. The blue line shows the spectrum pertaining to Fe that has zero nuclear spin (likely Fe ⁵⁶). The orange line corresponds to the spectrum of Fe ⁵⁷ with nuclear spin equal $\frac{1}{2}$. (c) Schematic of the evolution of two pertinent levels E associated to the Fe ⁵⁶ atom, compared to those of Fe ⁵⁷ , including the hyperfine interaction A after application of an external magnetic field B . Figure adapted from Ref. [42]	3
4.1.	Geometry of adatoms on MgO, NaF and NaCl. Top and side views of (a) adatom stacked on top of anion and (b) adatom in the bridge position. The adatom is represented by a blue sphere, the anion by a red sphere and the cation by an orange sphere. The definition of the distance d between the adatom and anion and the cation-anion-cation bond angle α is also illustrated	27
4.2.	Basic properties of isolated $3d$ transition metal atoms. (a) Spin magnetic moment, (b) spin-polarized energy levels and (c) Fermi contact contribution to the hyperfine interaction of isolated $3d$ transition metal atoms.	28
4.3.	Total energy of adatoms on the bridge position relative to the one for the anion-top position energy, calculated for structures relaxed within GGA-PBE. Ultra-thin films: (a) MgO, (b) NaF and (c) NaCl. The number to the left of the chemical formula in the legend indicates the number of layers in the ultra-thin film.	30
4.4.	Relaxed geometrical properties of adatoms on MgO ultra-thin films, placed on top of oxygen. (a) Mg-O-Mg bond angle and (b) distance between the adatom and oxygen. The number to the left of the chemical formula in the legend indicates the number of layers	31

4.5.	Magnetic properties of adatoms on MgO ultra-thin films, placed on top of oxygen (a–c) and on the bridge position (d–f). (a,d) Spin magnetic moment, (b,e) Fermi contact and (c,f) dipolar contributions to the hyperfine interaction. The number to the left of MgO in the legend indicates the number of layers in the ultra-thin film. The gray dash line represent the free-atom results. The black crosses in panels (b,c) and (e,f) refers to the experimental results for Fe and Ti from Ref. [42] and for Cu from Ref. [43]	32
4.6.	Thickness dependence of the electronic structure of a V adatom on MgO in the oxygen-top position. (a) One monolayer of MgO. (b) Two monolayers of MgO. (c) Free atom. The Fermi energy is marked by a vertical dashed line	33
4.7.	Relaxed geometrical properties of adatoms on NaF and NaCl ultra-thin films, placed on top of the respective anion. (a) Na–F–Na or Na–Cl–Na bond angle and (b) distance between the adatom and either F or Cl. The number to the left of the chemical formula in the legend indicates the number of layers	36
4.8.	Magnetic properties of adatoms on NaF and NaCl ultra-thin films, placed on top of anion (a–c) and on the bridge position (d–f). (a,d) Spin magnetic moment, (b,e) Fermi contact and (c,f) dipolar contributions to the hyperfine interaction. The number to the left of NaF and NaCl in the legend indicates the number of layers in the ultra-thin film. The gray dash line represent the free-atom results	37
4.9.	Relaxed geometrical properties of top-stacked adatoms on Cu_2N , h–BN and h–BN-vdW. (a) B–N–B and Cu –N– Cu bond angles and (b) Distance between the adatom and nitrogen	38
4.10.	Magnetic properties of top-stacked adatoms on Cu_2N and h–BN. (a) Spin magnetic moment, (b) Fermi contact and (c) dipolar contributions to the hyperfine interaction. The gray dash line represent the free-atom results	39
4.11.	Hyperfine interactions of magnetic adatoms on ultrathin films. (a) Fermi contact and (b) dipolar contributions. The free-atom values are given for comparison. The number to the left in the legend indicates the number of layers in the film. The adsorption position is denoted with T for atop the anion and with B for the bridge position (for h–BN and Cu_2N only T was considered). The possible impact of corrections from van der Waals interactions was explored for the h–BN case	42

0.1.	bilayer of MgO. The second MgO layer is not shown. The Fe adatom is stacked on top of O, on the bridge position and on top of Mg, respectively. Fe is represented by a blue sphere, O by a red sphere and Mg by an orange sphere. (b) Fermi contact contribution to the hyperfine interaction for the considered positions and (c) Fermi contact contribution as a function of the contribution to the spin magnetic moment coming from the s electrons (S-spin moment).	. 46
5.2.	Atomic structures for Fe dimers on a bilayer of MgO. The first row represents the Fe dimers in the ferromagnetic state and the second row those in the antiferromagnetic state. Fe atoms are represented by blue spheres, O by red spheres and Mg by orange spheres. The final diagram on the right defines the Fe-Fe distance, represented by the horizontal double arrow, and either the Fe-O or the Fe-Mg distance, whichever is nearest to the corresponding Fe atom, represented by the vertical	. 40
5.3.	double arrow. The green numbers on top of each structure in the first row give the Fe-Fe distance in the ferromagnetic state and the red ones in the second row in the antiferromagnetic state, in Å Basic properties of free-standing Fe dimers. (a) Total energy difference with respect to 2 Å of Fe-Fe distance in the ferromagnetic state, which is the most stable distance, (b) Fermi contact contribution to	. 47
5.4.	the hyperfine interaction, (c) atomic spin moment with the inset displaying the S-spin moment as function of atomic distances, and (d) Fermi contact contribution as a function of S-spin moment Noncollinear magnetism of free-standing Fe dimers. (a) Schematic of the considered magnetic configurations. (b) Total energy, (c) atomic	. 48
5.5.	spin magnetic moment and (d) S-spin magnetic moment as a function of the angle (θ) between the directions of the spins of the Fe dimer. Relaxed structural properties of Fe dimers on the MgO bilayer. (a) Total energy difference with respect to structure 1 in the ferromagnetic	. 51
5.6.	state, which is the most stable one, with the inset displaying total energy difference with respect to structure 2 in the antiferromagnetic state, which is the most stable one for Hubbard $U = 4$ eV. (b) Fe-Fe distance, (c) distance between Fe1 and either O or Mg, whichever is nearest, and (d) likewise for Fe2	. 53
	in (a,c) indicate the values found for the free-standing dimer at their equilibrium bond length in the ferromagnetic (F) and antiferromagnetic (AF) states. The Fermi contact contribution as a function of the S-Spin magnetic moment is shown in (b,d). The number inside the circles identifies the Fe dimer structures.	. 54

5.7.	Effect of the Hubbard- U on the hyperfine fields of Fe dimers on the bilayer of MgO in structure 1 (a and b) and structure 2 (c and d) in the ferromagnetic (F) and antiferromagnetic (AF) states. (a,c) Total energy difference with respect to $U = 0$ eV in the ferromagnetic state. (b,d) Fermi contact contribution to the hyperfine interaction. Fe1 and Fe2 in structure 1 they are equivalent.	56
6.1.	Atomic structures for $3d$ adatom and $3d$ –O molecules on a bilayer of MgO. $3d$ atoms are represented by blue spheres, O by red spheres and Mg by orange spheres	60
6.2.	Effect of the Hubbard- U correction on the electronic structure of a Co adatom (a, b, and c) atop oxygen (d, e, and f) from the MgO bilayer of MgO in the absence of SOC. (a, d) PDOS for U = 0 and J = 0, (b, e) PDOS for U = 4 eV and J = 1 eV, (c, f) PDOS for U = 6 eV and J = 1 eV. The Fermi energy is marked by a vertical dashed line	62
6.3.	Total energy difference of $3d$ –O molecules on the bilayer of MgO with respect to the one of structure 6. The structure number indicates a particular nanostructure illustrated in Fig. 6.1. Results obtained by LSDA + U + USPP calculations	66
6.4.	Magnetization directions along [100], [110], and [010] corresponding to $\phi=0^\circ$, 45°, and 90°, respectively, for $3d$ adatoms and $3d$ –O molecules on a bilayer of MgO. $3d$ atoms are represented by blue spheres, O by red spheres and Mg by orange spheres	67
6.5.	MAE of 3d adatoms and 3 d –O molecules on a bilayer of MgO. The structure number indicates a particular nanostructure with a specific orientation of the magnetization as illustrated in Fig. 6.4. A negative sign of the MAE favors an out-of-plane magnetization. Results obtained by LSDA + SOC + U + USPP calculations	68
6.6.	Energy barrier for the metastable perpendicular Co–O molecule on the bilayer of MgO. (a) the perpendicular Co–O molecule on the MgO bilayer ($\theta=0^{\circ}$), (b) total energy difference of Co–O molecule on the bilayer of MgO with respect to structure 3, as a function of the rotating angle (θ) and (c) The horizontal Co–O molecule on the MgO bilayer ($\theta=90^{\circ}$). θ is the rotation angle away from the z-axis towards the x-axis. Here we used $U=6$ and $J=1$ eV	69
6.7.	Energy barrier for the metastable perpendicular Fe–O molecule on the bilayer of MgO. (a) the perpendicular Fe–O molecule on the MgO bilayer ($\theta = 0^{\circ}$), (b) total energy difference of Fe–O molecule on the bilayer of MgO with respect to structure 3, as a function of the rotating angle (θ) and (c) The horizontal Fe–O molecule on the MgO bilayer ($\theta = 90^{\circ}$). θ is the rotation angle away from the z-axis towards the x-axis. Here we used $U = 6$ and $U = 1$ eV	70

6.8.	Fermi contact contribution to the hyperfine interaction of 3d adatoms and 3d–O molecules on a bilayer of MgO. The structure number indicates a particular nanostructure illustrated in Fig. 6.1. Here we used $U = 6$ eV. Results obtained by GGA + U + PAW calculations	71
7.1.	Schematic view on a possible network of hybrid qubits involving the nuclear and electronic spins constructed atom-by-atom, probed and coherently driven by an STM tip equipped with RF voltage pulses. Within the probed Fe adatom, the nuclear magnetic moment interacts with the electronic one via the hyperfine interaction. As shown in the thesis, a neighboring Fe magnetic moment imposes a magnetic interaction, which can be either ferromagnetic or antiferromagnetic, and more importantly it can modify the hyperfine interaction. The perpendicular 3d–O molecules predicted in our work could potentially be utilized as stable magnets which dictate an exchange field on a particular qubit.	76
A.1.	Relaxed geometrical properties of adatoms on MgO ultra-thin films, placed on the bridge position. (a,c) Mg–adatom–Mg and O–adatoms–O bond angle and (b,d) distance between the adatom and Mg and O. (a,b) results for single layer and (c,d) results for two layers of MgO	79
A.2.	Relaxed geometrical properties of adatoms on NaF ultra-thin films, placed on the bridge position. (a,c) F-adatom-F and Na-adatom-Na bond angle, (b,d) Distance between the adatom and either F or Na. (a,b) results for single layer and (c,d) results for two layers of NaF	80
A.3.	Relaxed geometrical properties of adatoms on NaCl ultra-thin films, placed on the bridge position. (a,c) Cl-adatom-Cl and Na-adatom-Na bond angle, (b,d) Distance between the adatom and either Cl or Na. (a,b) results for single layer and (c,d) results for two layers of NaCl.	81
A.4.	Effect of the Hubbard- U correction on the properties of the Fe adatom on the oxygen-top position for two layers of MgO. (a) Change in the spin moment. (b) Change in the Fermi contact contribution to the hyperfine interaction. (c) Change in the dipolar contribution to the hyperfine interaction.	82
A.5.	Effect of changing the bond length on the properties of the Fe adatom on the oxygen-top position for two layers of MgO. (a) Change in the spin moment. (b) Change in the Fermi contact contribution to the hyperfine interaction. (c) Change in the dipolar contribution to the hyperfine interaction. The previously optimized geometry was kept fixed, and only the position of the Fe adatom was changed	82

A.6.	Effect of changing the lattice constant on the properties of the Fe adatom on the oxygen-top position for two layers of MgO. (a) Change in the spin moment. (b) Change in the Fermi contact contribution to the hyperfine interaction. (c) Change in the dipolar contribution to the hyperfine interaction. The geometry was optimized for each value of the lattice constant	83
A.7.	Effect of the smearing parameter on the properties of the Fe adatom on the oxygen-top position for two layers of MgO. (a) Change in the spin moment. (b) Change in the Fermi contact contribution to the hyperfine interaction. (c) Change in the dipolar contribution to the hyperfine interaction. The vertical dashed line indicates the value used for systematic calculations	83
B.1.	Effect of the penalty term (λ) on the properties of noncollinear states of free-standing Fe dimers (Fe-Fe distance 2.0 Å). (a) Constrained-energy (penalty energy), corresponding to different input opening angles between the two Fe spin moments. (b) The self-consistent opening angle between magnetic moments of the two atoms of Fe dimer corresponding to different input opening angles	84
B.2.	Effect of the kinetic energy cutoff for the wavefunctions ('ecutwfc') on the basic properties of free-standing ferromagnetic Fe dimer (Fe-Fe distance 2.0Å). Results obtained with PAW (a-c) and with USPP (d-f). (a,d) Total energy. (b,e) Fe net spin moment. (c,f) Fe s-orbital projected moment. The cutoff for the density is ecutrho = 8^* ecutwfc. Fe1 and Fe2 are equivalent	85
B.3.	Effect of the kinetic energy cutoff for the wavefunctions ('ecutwfc') on the basic properties of ferromagnetic Fe dimers in structure 1 on the MgO bilayer. Results obtained with PAW (a-c) and with USPPs (d-f). (a,d) Total energy. (b,e) Fe net spin moment. (c,f) Fe s-orbital projected moment. Fe1 and Fe2 in structure 1 they are equivalent	86
B.4.	Dipolar contributions to the hyperfine interaction for the different Fe dimer structures and magnetic states. The number identifies the Fe dimer structures	86
B.5.	Effect of the Hubbard- U correction on the hyperfine fields of Fe dimers on the bilayer of MgO in structure 3 (a and b) and structure 4 (c and d) in the ferromagnetic (F) and antiferromagnetic (AF) states. (a,c) Total energy difference with respect to $U = 0$ eV in the ferromagnetic state. (b,d) Fermi contact contribution to the hyperfine interaction.	87

В.б.	Effect of the Hubbard- U correction on the hyperfine fields of Fe dimers on the bilayer of MgO in structure 5 (a and b) and structure 6 (c and d) in the ferromagnetic (F) and antiferromagnetic (AF) states. (a,c) Total energy difference with respect to $U = 0$ eV in the ferromagnetic state. (b,d) Fermi contact contribution to the hyperfine interaction. Fe1 and Fe2 in structures 5 and 6 they are equivalent	88
B.7.	Effect of the Hubbard- U correction on the hyperfine fields of Fe dimers on the bilayer of MgO in structure 7 (a and b) in the ferromagnetic (F) and antiferromagnetic (AF) states. (a) Total energy difference with respect to $U=0$ eV in the ferromagnetic state. (b) Fermi contact contribution to the hyperfine interaction	89
C.1.	Spin magnetic moment of 3d adatom and 3 d –O molecules on a bilayer of MgO. The structure number indicates a particular nanostructure with a specific orientation of the magnetization as illustrated in Fig. 6.4. Results obtained by LSDA + SOC + U + USPP calculations	90
C.2.	Total energy difference of 3 d –O molecules on the bilayer of MgO with respect to structure 6, which is the most stable one. The structure number indicates a particular nanostructure illustrated in Fig. 6.1. Results obtained by GGA + U calculations	91
C.3.	Spin magnetic moment of 3d adatoms and 3d–O molecules on a bilayer of MgO. The structure number indicates a particular nanostructure illustrated in Fig. 6.1. Here we use $U=6$ eV. Results obtained by GGA + U calculations	92
C.4.	S-spin magnetic moment of 3d adatom and 3 d -O molecules on a bilayer of MgO. The structure number indicates a particular nanostructure illustrated in Fig. 6.1. Here we used $U=6$ eV. Results obtained by GGA + U calculations	93
C.5.	Total energy difference of $3d$ –O molecules on the bilayer of MgO with respect to structure 6, which is the most stable one. The structure number indicates a particular nanostructure illustrated in Fig. 6.1. Results obtained by GGA + PAW calculations	94
C.6.	Spin magnetic moment of 3d adatom and 3 d –O molecules on a bilayer of MgO. The structure number indicates a particular nanostructure illustrated in Fig. 6.1. Results obtained by GGA + PAW calculations	95
C.7.	Fermi contact contribution to the hyperfine interaction of 3d adatom and $3d$ –O molecules on a bilayer of MgO. The structure number indicates a particular nanostructure illustrated in Fig. 6.1. Results obtained by GGA + PAW calculations	96
C.8.	S-spin magnetic moment of 3d adatom and $3d$ –O molecules on a bilayer of MgO. The structure number indicates a particular nanostructure illustrated in Fig. 6.1. Results obtained by GGA + PAW calculations.	97

C.9.	Effect of the Hubbard-U correction on the magnetic properties of the					
	isolated $3d$ -O molecule, for $U = 0$ (a, b, and c) and for $U = 6$ eV (d, e,					
	and f). (a,d) Fermi contact contribution to the hyperfine interaction.					
	(b,e) Spin magnetic moment. (c,f) S-spin magnetic moment. Results					
	obtained by GGA + PAW calculations	98				

List of Tables

4.1.	Experimental vs. theoretical lattice constants for the considered systems.	26
6.1.	MAE of the isolated Co–O molecule from DFT+SOC total energy calculations for different types of pseudopotentials (PPs) and exchange-correlation functionals, ($d_{\text{Co-O}} = 2\text{Å}$). A negative sign of the MAE	
6.2.	favors an out-of-plane magnetization	61
	from LSDA+SOC+U total energy calculations and from Experiment	
	(exp). A negative sign of the MAE favors an out-of-plane magnetization. U and J are given in eV	62
6.3.	Nonvanishing angular momentum matrix elements between d -states.	Ŭ -
	The notation is given for the d -states in Cartesian coordinates with z being the quantization axis, in units of h	64
6.4.		04
	degenerate perturbation theories to the MAE of Co adatom on the bi-	
	layer of MgO in the oxygen-top position from DFT+U with the absence of SOC. A negative sign of the MAE favors an out-of-plane magneti-	
	zation. U and J are given in eV, while the MAE is in meV	65
6.5.	MAE of the isolated Co-O molecule from LSDA+ SOC + U total	
	energy calculations for different bond lengths between Co and O atoms (d_{Co-O}) . CoO/2MgO is the perpendicular Co-O molecule on the MgO	
	bilayer (see Fig. 6.1-2 and Fig. 6.4-2). A negative sign of the MAE	
	favors an out-of-plane magnetization. Here we used $U=6$ and $J=1$ eV.	69

1. Introduction

Magnetic storage devices have come a long way since their inception, evolving from large room-sized machines to compact devices that can hold terabytes of data. Over the years, technological advancements have pushed the limits of storage capacity from bulky hard disk drives (HDDs) to smaller and more efficient solid-state drives (SSDs). However, as the demand for data storage increases exponentially, traditional magnetic storage devices are reaching their physical limits regarding storage capacity. Recent research has focused on exploring alternative approaches to push the boundaries of magnetic storage, including using single atoms and surface-embedded molecular magnetic structures as potentially the smallest possible magnetic bits. Unprecedented progress opened up new possibilities tackling storage issues and paved the way for the development of quantum computers, which rely on manipulating individual atoms or subatomic particles, known as qubits, as building blocks for quantum computing [1]–[6].

The field of quantum computing has gained significant attention due to the potential of revolutionizing various fields, including cryptography, drug discovery, and optimization problems. The basic building blocks of quantum computers are quantum bits, or qubits, which are the fundamental information units in quantum systems. Unlike classical bits, which can be in either a 0 or 1 state, qubits can be in a superposition of both states simultaneously, allowing for parallel processing and exponentially increased computational power.

At the atomic-scale, the behavior of individual atoms and molecules can exhibit unique quantum properties, that can be harnessed for novel applications, including conventional data storage [7], [8] while reaching out to quantum related implementations crucial for quantum computation [9], and coherent quantum manipulation [10], [11]. Current state-of-the-art research aims at exploring the possibility of establishing magnetic atoms on surfaces as a platform for the realization of quantum computation concepts with the possibility of utilizing scanning tunneling microscopy (STM) and spectroscopy (STS) [12]–[15] for an atom-by-atom construction and characterization of complex networks of qubits. STM/STS is a powerful nanoscale imaging technique that can reveal atomic details of surfaces with unprecedented resolution, allowing for direct observation and manipulation of individual atoms and molecules. STM/STS has revolutionized fields such as nanoscience, materials science, and surface physics, enabling breakthroughs in our understanding of matter and leading to the development of new technologies at the atomic scale.

However, in the context of qubits made of adsorbates deposited on substrates, the field faces various challenges. Utilizing tunneling current naturally triggers decoherence mechanisms unwanted for qubit-related applications. Moreover, the coupling of magnetic atoms and the underlying substrate presents both challenges and opportunities. While this coupling imposes a magnetic anisotropy energy, which can act as an energy barrier necessary to protect a spin in a given direction, it may also lead to its destabilization via various mechanisms, involving electron-hole excitations [16]–[20] and phonons [21]. To address these aspects, two main approaches have been pursued: employing thin insulating layers [7], [8], [22]–[53] or bringing several magnetic atoms together to reduce their quantum mechanical fluctuations [17], [54]–[58].

A way to avoid the aforementioned issues of decoherence inherent to the electronic spin moment is to consider nuclear magnetic moments, which are naturally weakly coupled to the environment making it both a blessing and a curse. In comparison to electron spin moments, individual nuclear spin states tend to have a much longer lifetime and therefore hold in principle a greater promise as building blocks for quantum computers [1]-[6]. This is of course an ideal property for a qubit but makes it extremely difficult to characterize and ultimately manipulate it. Nuclear moments are coupled to the electronic ones via the hyperfine interaction [59]-[61], which for decades has been harvested to gain insight into the electronic structure and chemical bonding of atoms, molecules, and solids, as explored with nuclear magnetic resonance techniques [62]. The latter are averaging setups that probe the hyperfine interactions of numerous nuclear moments at once. Recently a breakthrough has been realized with STM-based single-atom electron paramagnetic/spin resonance (EPR/ESR) [33], [36], [39], [40], [42]–[45], [52], [63]–[68] techniques, following previous efforts such as in Refs. [69]-[72], which have allowed for the detection of the extremely weak hyperfine interactions of single atoms [42]–[45].

The seminal paper of Willke et al. [42] was published just before starting the current PhD thesis. They detected the hyperfine interaction of individual adatoms (Fe and Ti) deposited on two layers of MgO grown on an Ag(100) surface. A schematic illustration of the experiment and the resulting measurements is provided in Fig. 1.1. Besides the usually applied bias voltage in an STM experiment, here a RF voltage is amended which drives an ESR signal detectable in the tunneling current (Fig. 1.1a). Instead of a single peak, two resonances are identified on a few atomic species. The case of Fe adatom is shown in Fig. 1.1b, where the splitted resonance is interpreted as a manifestation of an additional coupling due to the hyperfine interaction characterizing the $\mathrm{Fe^{57}}$ isotope, which has a natural abundance of 2% and a nuclear spin equal to one-half. Fig. 1.1c shows how the single ESR Peak emerges at a frequency f_0 from the splitting of a two-level systems due to the application of a magnetic field. Due to the hyperfine interaction, the initial and final levels experience a splitting, which according to the excitation selection rules lead to two resonances shifted away from each other by Δf , directly connected to the hyperfine constant. This work opened unprecedented opportunities to not only quantify such a small interaction but also to manipulate its magnitude by controlling the location of the adsorbate.

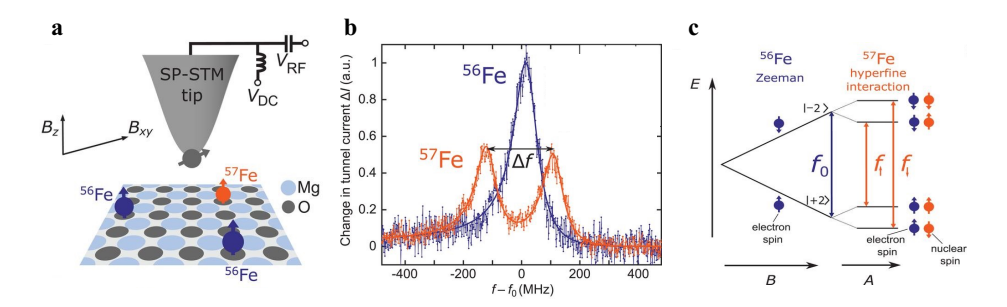


Figure 1.1.: The hyperfine interaction studied by ESR in a scanning tunneling microscopy setup. (a) A schematic of the STM experimental set up showing different isotopes of single Fe atoms on a bilayer MgO film grown on Ag(001). (b) ESR spectra for different Fe isotopes. The blue line shows the spectrum pertaining to Fe that has zero nuclear spin (likely Fe⁵⁶). The orange line corresponds to the spectrum of Fe⁵⁷ with nuclear spin equal $\frac{1}{2}$. (c) Schematic of the evolution of two pertinent levels E associated to the Fe⁵⁶ atom, compared to those of Fe⁵⁷, including the hyperfine interaction A after application of an external magnetic field B. Figure adapted from Ref. [42].

Intriguingly, however, the STM-detected hyperfine interaction was so far limited to a few atomic species on a two-layers thick MgO film. Moreover, the actual mechanism underpinning the EPR/ESR experiments is still under investigation [67], [73]–[78]. Definitely, a deep understanding of the hyperfine interactions in these systems is crucial for unlocking their full potential for quantum information storage and processing. Overall, this motivated us to proceed to a systematic investigation of the hyperfine interaction of various nanostructures made of transition metal adatoms (from Sc to Cu) placed on a numerous bonding sites of a rich set of insulating films (Mgo, NaF, NaCl, h-BN and Cu₂N). Our goal is to identify trends and the ideal combination of materials required to maximize the hyperfine interaction, which is crucial for the experimental community. Furthermore, we aim at unveiling the mechanisms governing nuclear spin dynamics and polarization and their intertwined correlations with other electronic and magnetic properties of the underlying materials. Of great interest is to unravel the interdependence between complex magnetic states and the hyperfine interactions of multi-atomic nanostructures.

Besides the hyperfine interaction, a fundamental energy scale addressed in this thesis and crucial in the context of magnetic nanostructures on surfaces is the magnetic anisotropy energy (MAE), which confers stability to a magnetic moment against fluctuations, making it robust and stable, and allowing the magnetization to be oriented

in a preferred spatial direction for a sufficient duration of time. Strategies for enhancing the MAE of magnetic adatoms are based on a large spin-orbit coupling (SOC) energy, a significant orbital moment, and a special ligand field. However, achieving a massive MAE without a suitable surface or substrate is challenging. Surprisingly, it turns out that on the very same MgO substrate, on which the hyperfine interaction was identified, the largest transition metal MAE of a few tens of meV, reaching the limit expected for 3d atoms and favouring an out-of-plane magnetic orientation, was measured for a Co adatom [8]. This motivated us to scrutinize the MAE of the systems for which we already determined the underlying hyperfine interaction and fingerprint the mechanisms responsible for the large MAE while proposing a new set of molecular nanostructures, made of oxygen and transition metal atoms. The latter molecules can surprisingly sit perpendicularly to the substrate, offering an ideal scenario for weak coupling to the substrate, responsible for decoherence, and large MAEs.

Our first-principles calculations have been carried out in the framework of the density functional theory (DFT) [79], [80], which has emerged as a powerful tool for predicting and understanding various properties of realistic materials on the level of quantum theory of interacting electrons without adjustable parameters. The essence of DFT is to address the insurmountable quantum-mechanical many-body problem of realistic materials by identifying the electronic charge density as the quantity that determines completely the ground state properties of the many-electron system. DFT has revolutionized a large set of fields, in particular magnetism by accurately predicting magnetic properties, such as magnetic moments, magnetic ordering, and magnetic anisotropy.

The thesis is structured as follows. In the second chapter, the theoretical and computational framework, which is used throughout this thesis, is introduced. Specifically, The basic concepts of density functional theory, spin-orbit coupling and hyperfine interaction are summarized. Furthermore a brief description of the utilized computational code, Quantum ESPRESSO, is presented. This code is widely used in the ab-initio community and provides the advantage of simulations atomic relaxations while giving access to various electronic and magnetic properties. It can be interfaced with other codes to perform post-processing or to give access to initially not produced quantities. For instance, the hyperfine interaction is obtained via GIPAW.

The third chapter is designed for the reader interested in a thorough derivation of the hyperfine and spin-orbit interactions, which are the cornerstones of the thesis. Our starting point is the Dirac Hamiltonian [81], [82]. Major approximations leading to the final forms known in the literature are highlighted with an effort to make the derivation short and concise.

The fourth chapter is devoted to an extensive computational investigation of the hyperfine interaction tensor of the whole series of 3d transition-metal adatoms deposited on various thicknesses of insulating thin films of experimental interest. We

identify the atoms and substrates triggering the most efficient hyperfine interactions and uncover the relevant trends, providing a valuable map for the corresponding experimental and theoretical communities.

In the fifth chapter, we tackle the case of multi-atomic nanostructures and investigate the impact of a non-trivial magnetic state on the underlying hyperfine interaction. We focus our study on the case of dimers and chose Fe adatoms as the building blocks of nano-objects under scrutiny. Our choice on Fe was motivated by its minimal nuclear moment while hosting a significant hyperfine interaction, which should simplify the experimental verification of our predictions. We explore the correlation between the hyperfine interaction and the magnetic state of Fe dimers, free-standing and deposited on a bilayer of MgO(001). We find that the magnitude of the hyperfine interaction can be controlled by switching the magnetic state of the dimers, and we demonstrate the ability to substantially modify the hyperfine interaction by atomic control of the location of the adatoms on the substrate. Interestingly, we demonstrate the limits of the usual hyperfine hamiltonian for complex magnetism and propose a straightforward extension.

In the sixth chapter, we investigate the possibility of enhancing the magnetic anisotropy energy of 3d transition metal adatoms by considering various structural geometries of 3d–O molecules deposited on MgO. We reproduce the experimentally measured large magnetic anisotropy energy of an individual Co adatom on a MgO (001) surface and unveil the mechanism behind it. Conventional density functional theory with the local density approximation or generalized gradient approximation for the exchange and correlation potential underestimate strongly the magnetic anisotropy. It is only with careful simulations incorporating static correlations combined with spin-orbit coupling that large values of the magnetic anisotropy energy are recovered. We also evidence the ability to substantially modify the MAE by atomic control of the location of the 3d–O molecules on the substrate and explore the underlying hyperfine interactions.

Finally, we conclude the thesis by summarizing the results and providing a short outlook on future exciting research directions.

2. Density Functional Theory

Condensed matter physics is the study of macroscopic and microscopic properties of a large number of interacting atoms and electrons, which are the quantum building blocks of solids. The theoretical description of the latter ideally requires to solve the Schrödinger equation, which is highly non-trivial when involving many-body interactions as the computational cost typically scales exponentially with the system's complexity. Consider a Co atom as an example; it contains 27 electrons; in three dimensions, we have $3 \times 27 = 81$ degrees of freedom; and if we try to solve Eq.(2.1) on a real space grid with 10 points in each dimension, we need to store 10^{81} numbers, which is roughly the number of atoms in the universe [83].

Among the many proposed methods [84]–[88] to tackle this problem, density functional theory (DFT) [79], [80] provides in practice a good balance between accuracy in the results and computational time. DFT, though exact in principle, relies om practice on several approximations and simplifications to map the quantum many-body problem to solve for the eigenstates and eigenvalues of a single-particle Hamiltonian in a self-consistent manner. The fundamental concepts of DFT are summarized here.

2.1. The Many-body Schrödinger Equation

The Schrödiger equation to be solved:

$$\hat{H}\Psi(\mathbf{r}_{1},\mathbf{r}_{2},...,\mathbf{r}_{N_{e}},\mathbf{R}_{1},\mathbf{R}_{2}...,\mathbf{R}_{N_{n}}) = E\Psi(\mathbf{r}_{1},\mathbf{r}_{2},...,\mathbf{r}_{N_{e}},\mathbf{R}_{1},\mathbf{R}_{2}...,\mathbf{R}_{N_{n}})$$
(2.1)

pertains to a system consisting of N_e interacting electrons and N_n nuclei (ions). $\hat{\mathbf{H}}$ is the Hamiltonian while $\Psi(\mathbf{r}_{N_e}, \mathbf{R}_{N_n})$ is the many-body wavefunction of the system. \mathbf{r}_i and \mathbf{R}_I are the position vectors for the electrons and the ions, respectively. E denotes the energy of the system. Note that the spin is disregarded in this notation. The general form of the full many-body Hamiltonian reads [89]:

$$\hat{\mathbf{H}} = \underbrace{-\frac{\hbar^{2}}{2m_{e}} \sum_{i}^{N_{e}} \nabla_{i}^{2}}_{\mathbf{T_{e}}} \underbrace{-\frac{\hbar^{2}}{2} \sum_{I}^{N_{n}} \frac{1}{M_{I}} \nabla_{I}^{2}}_{\mathbf{T_{n}}} \underbrace{-\sum_{i,I} \frac{e^{2}Z_{I}}{|\mathbf{r}_{i} - \mathbf{R}_{I}|}}_{\mathbf{V_{e-n}}} \underbrace{+\frac{1}{2} \sum_{i \neq j} \frac{e^{2}}{|\mathbf{r}_{i} - \mathbf{r}_{j}|}}_{\mathbf{V_{e-e}}} \underbrace{+\frac{1}{2} \sum_{I \neq J} \frac{e^{2}Z_{I}Z_{J}}{|\mathbf{R}_{I} - \mathbf{R}_{J}|}}_{\mathbf{V_{n-n}}},$$
(2.2)

where the first term (T_e) represents the kinetic energy of the electrons, the second term (T_n) the kinetic energy of the ions, the third term (V_{e-n}) the attractive interaction between an electron at \mathbf{r}_i and an ion at \mathbf{R}_I , the fourth term (V_{e-e}) the repulsion

between the electrons and the last term (V_{n-n}) the repulsion between ions. \hbar is the Planck constant divided by 2π , m_e is the electron mass, e is the electron charge, M_I and Z_I are mass and atomic number of ion I. ∇_i^2 , ∇_I^2 are the Laplacian operators with respect to \mathbf{r}_i and \mathbf{R}_I respectively. In Eq.(2.2) sums over the lower case indices (i,j) run over all electrons and the sums over the upper case indices (I,J) run over all ions.

2.2. Born-Oppenheimer Approximation

Since electrons are much lighter than the nuclei, they move much faster. It is thus a good approximation to consider the nuclei to be stationary on the time scale of the electronic motion. Therefore, we could replace in Eq.(2.2) the interaction of the nuclei with each other (V_{n-n}) by a constant (E_{n-n}) and remove the kinetic energy of the nuclei (T_n) . This leads to an adiabatic approximation known as the Born-Oppenheimer Approximation [90]:

$$\hat{H}_{BO} = T_e + V_{e-n} + V_{e-e} + E_{n-n} . \tag{2.3}$$

Collecting the second and the fourth terms together into V_{ext} in Eq.(2.3), we get our simplified Hamiltonian for electrons:

$$\hat{H}_{BO} = T_e + V_{e-e} + V_{ext}$$
 (2.4)

Using the Born-Oppenheimer approximation is the first step toward effectively describing a system of interacting particles. However, the electronic problem is a quantum many-body problem; the wavefunction $\Psi(\mathbf{r}_1, \mathbf{r}_2, ..., \mathbf{r}_{N_e})$ of the system depends on the coordinates of all the electrons because of their mutual interaction, and can not be separated into a single particle contribution. Because of that, the problem is still far too complicated to be solved exactly.

2.3. Hohenberg-Kohn Theorems

In 1964 Hohenberg and Kohn [79] laid the fundamental groundwork for DFT. The basic idea behind DFT is to solve the many-body electronic problem by concentrating on the single-particle probability density, which depends on just one spatial variable, rather than calculating the many-body wavefunction $\Psi(\mathbf{r}_1, \mathbf{r}_2, ..., \mathbf{r}_{N_e})$, which depends on the coordinates of all the electrons in the system. The ground state single-particle probability density $n_{\rm gs}(\mathbf{r})$ for a system of N_e interacting electrons described by Hamiltonian of Eq.(2.4) is as follows:

$$n_{\rm gs}(\mathbf{r}) = \int |\Psi(\mathbf{r}_1, \mathbf{r}_2, ..., \mathbf{r}_{N_e})|^2 d\mathbf{r}_2 d\mathbf{r}_3 ... d\mathbf{r}_n.$$
(2.5)

Consequently, it is straightforward to see that $n_{\rm gs}(\mathbf{r})$ is a functional of the external potential $V_{\rm ext}(\mathbf{r})$. The first Hohenberg-Kohn theorem contains the inverse relationship

stating that the potential is a functional of density [79] "For any system of particles in an external potential $V_{\rm ext}(\mathbf{r})$, the potential $V_{\rm ext}(\mathbf{r})$ is uniquely determined, excluding constants, by the ground state particle density $n_{\rm gs}(\mathbf{r})$ ". This theorem naturally implies that any ground-state observable of a particular system is uniquely represented as a functional of ground-state electron density, hence the name density functional theory. The total energy of the many body system can therefore be written as a functional of the density:

$$E = E[n] = T_e[n] + V_{e-e}[n] + V_{ext}[n].$$
 (2.6)

Hohenberg and Kohn went further by demonstrating their second theorem: "The total energy functional E[n] is minimised by the ground state density $n_{\rm gs}(\mathbf{r})$ ". This implies that the density can be calculated using the variational principle.

Although the Hohenberg-Kohn theorems are very powerful, they do not provide a practical scheme for minimizing Eq.(2.6), which is required to obtain the ground state density. This has been further elaborated by by Kohn and Sham [80] as briefly summarized below.

2.4. Kohn-Sham Formulation

About a year after the Hohenberg-Kohn theorems were proposed, Kohn and Sham [80] developed a systematic method to minimize the total energy functional, laying the groundwork for modern DFT calculations. Their strategy is to map the fully interacting many-body problem onto an auxiliary system of non-interacting particles under the condition that the latter system has the same ground state density and, consequently, the same ground state energy as the interacting system under study. The system of non-interacting particles is in principle trivial to address. The corresponding single-particle wavefunctions ψ_i build up the electron density

$$n(\mathbf{r}) = \sum_{i} |\psi_{i}(\mathbf{r})|^{2}, \qquad (2.7)$$

which is the key ingredient in defining the Kohn-Sham energy functional:

$$E_{KS}[n] = T_s[n] + \int n(\mathbf{r})V_{ext}(\mathbf{r})d\mathbf{r} + E_H[n] + E_{xc}[n]. \qquad (2.8)$$

 $T_s[n]$ is the kinetic energy of the non-interacting particles which reads:

$$T_s[n] = -\frac{\hbar^2}{2m_e} \sum_i \langle \psi_i | \nabla^2 | \psi_i \rangle . \qquad (2.9)$$

The second term in Eq. 2.8 represents the energy of the electron's interaction with the external potential V_{ext} while the third term $E_{\text{H}}[n]$ is the classical Coulomb repulsion (Hartree) energy given by:

$$E_{H}[n] = \frac{e^2}{2} \int \frac{n(\mathbf{r})n(\mathbf{r'})}{|\mathbf{r} - \mathbf{r'}|} d\mathbf{r} d\mathbf{r'}. \qquad (2.10)$$

The last term $(E_{xc}[n])$ is the exchange and correlation (xc) energy, which includes all the many-body effects enabling the mapping to the full many body system. All the contributions of the Kohn-Sham energy functional in Eq.(2.8) can be explicitly written down for any system except for the last term, which in practice is approximated. After minimizing (2.8) to find the ground state energy, one finds single-particle Kohn-Sham equations, which need to be solved self-consistently:

$$\hat{H}_{KS}\psi_i(\mathbf{r}) = \varepsilon_i\psi_i(\mathbf{r}) , \qquad (2.11)$$

$$\left[\frac{\hbar^2}{2m_e}\nabla_i^2 + V_{\text{eff}}(\mathbf{r})\right]\psi_i(\mathbf{r}) = \varepsilon_i\psi_i(\mathbf{r}) , \qquad (2.12)$$

where ε_i is the single-particle energies, and the effective Kohn-Sham potential $V_{\text{eff}}(\mathbf{r})$ is the functional derivative of the energy functional $E_{KS}[n]$ without the kinetic energy term $T_s[n]$ in Eq.(2.8), with respect to $\mathbf{n}(\mathbf{r})$:

$$V_{\text{eff}}(\mathbf{r}) = \frac{\delta(E_{KS}[n] - T_{s}[n])}{\delta n(\mathbf{r})} = V_{\text{ext}}(\mathbf{r}) + V_{H}(\mathbf{r}) + V_{xc}(\mathbf{r}), \qquad (2.13)$$

where $V_H(\mathbf{r})$ is the electrostatic Hartree potential:

$$V_{H}(\mathbf{r}) = \frac{\delta E_{H}[n]}{\delta n(\mathbf{r})}$$
 (2.14)

and $V_{xc}(\mathbf{r})$ is the exchange-correlation potential:

$$V_{xc}(\mathbf{r}) = \frac{\delta E_{xc}[n]}{\delta n(\mathbf{r})}.$$
 (2.15)

2.5. Spin polarized DFT

By decomposing the charge density $n(\mathbf{r})$ into its spin components, DFT can be extended to spin-polarized systems [91], [92]:

$$n(\mathbf{r}) = n^{\uparrow}(\mathbf{r}) + n^{\downarrow}(\mathbf{r}) , \qquad (2.16)$$

where $n^{\uparrow}(\mathbf{r})$ denotes the density of the majority spin electrons and $n^{\downarrow}(\mathbf{r})$ denotes the density of the minority spin electrons. Consequentially, the magnetic density is defined as

$$m(\mathbf{r}) = n^{\uparrow}(\mathbf{r}) - n^{\downarrow}(\mathbf{r}) . \tag{2.17}$$

Majority and minority spin electrons are now required to satisfy two separate Kohn-Sham equations (if dealing with collinear magnetism and spin-orbit coupling neglected):

$$\hat{\mathbf{H}}_{KS}^{\sigma} \psi_i^{\sigma}(\mathbf{r}) = \varepsilon_i^{\sigma} \psi_i^{\sigma}(\mathbf{r}) , \qquad (2.18)$$

where σ is the spin index, $\sigma = (\uparrow, \downarrow)$. The spin-dependent effective Kohn-Sham potential reads:

$$V_{\text{eff}}^{\sigma}(\mathbf{r}) = V_{\text{ext}}(\mathbf{r}) + \int \frac{e^2 n(\mathbf{r}')}{|\mathbf{r} - \mathbf{r}'|} d\mathbf{r} + \frac{\delta E_{\text{xc}}[n^{\uparrow}(\mathbf{r}), n^{\downarrow}(\mathbf{r})]}{\delta n^{\sigma}(\mathbf{r})}.$$
 (2.19)

The Kohn-Sham equations can also be extended to account for relativistic corrections, spin-orbit coupling [93] and non-collinear magnetism[94], [95] with the introduction of two component spinor wavefunctions.

2.6. Exchange and Correlation functionals

One of the most challenging aspects of any DFT method is approximating the exchange-correlation energy to reproduce the properties of the desired system. The computational cost of a given approach is another crucial factor to consider. In this section, we will discuss the two most famous methods for approximating the exchange-correlation energy, which are quite effective at predicting the properties of a wide rang of materials.

2.6.1. Local spin density approximation (LSDA)

One of the first and most straightforward methods is called the local density approximation (LDA). This approximation was proposed in the original work of Kohan and Sham [80] and is currently one of the most widely used DFT functionals.

In this thesis, we employ an extension of this approximation called the local spin density approximation (LSDA), which accounts for different spin channels [96]. In LDA and LSDA, the exchange-correlation energy is approximated by that of a "homogeneous" electron gas, whose density is assumed to be identical to the local electron density:

$$E_{xc}^{LSDA}[n^{\uparrow}, n^{\downarrow}] = \int n(\mathbf{r}) \epsilon_{xc}^{hom}(n^{\uparrow}(\mathbf{r}), n^{\downarrow}(\mathbf{r})) d\mathbf{r} , \qquad (2.20)$$

where $\epsilon_{\text{xc}}^{\text{hom}}(n^{\uparrow}(\mathbf{r}), n^{\downarrow}(\mathbf{r}))$ is the exchange-correlation energy density of a homogeneous electron gas. The exchange correlation energy is composed of an exchange component and a correlation component:

$$\epsilon_{xc}(n^{\uparrow}(\mathbf{r}), n^{\downarrow}(\mathbf{r})) = \epsilon_{x}(n^{\uparrow}(\mathbf{r}), n^{\downarrow}(\mathbf{r})) + \epsilon_{c}(n^{\uparrow}(\mathbf{r}), n^{\downarrow}(\mathbf{r})), \qquad (2.21)$$

where ϵ_x is the exchange contribution which can be calculated using the Hartree-Fock method for the homogeneous electron gas [97]. While ϵ_c , which is the correlation contribution, can be computed by using Quantum Monte Carlo simulations[96], [98]. In general, LSDA works exceptionally well for systems with slowly varying densities, such as metals. Moreover, LSDA also gives reasonable results for other materials "inhomogeneous systems" because of a systematic error cancellation, namely LSDA

underestimates the exchange energy, but it overestimates the correlation one, with the two having opposite signs [99].

Perdew and Zunger's parameterization is the most popular [100] LSDA flavour. The many advantages and disadvantages of LSDA have been extensively discussed in the literature [101]. In particular, the structural and vibrational properties, such as bond lengths, bond angles, and phonon vibrational frequencies, are well predicted by the functional. The main issue with LSDA is that the band gap of semiconductors and insulators is underestimated and is some cases may instead incorrectly predict a metallic ground state. Subsequently, more elaborate approximations for the exchange-correlation energy functional were introduced. The generalized gradient approximation (GGA) is one example.

2.6.2. Generalized gradient approximation (GGA)

The generalized gradient approximation (GGA) [102], [103] is a more sophisticated approach that builds on the LSDA functional such that in addition to the local electron density, the local gradient of electron density is included. For the spin polarized case the energy functional can be expressed as:

$$E_{xc}^{GGA}[n^{\uparrow}, n^{\downarrow}] = \int n(\mathbf{r}) \epsilon_{xc}(n^{\uparrow}(\mathbf{r}), n^{\downarrow}(\mathbf{r}), \nabla n^{\uparrow}(\mathbf{r}), \nabla n^{\downarrow}(\mathbf{r})) d\mathbf{r} . \qquad (2.22)$$

GGA functionals are generally preferred over LSDA because they contain more physical information about $n(\mathbf{r})$. There are a number of GGA formulations, but the most prevalent is that of Perdew, Burke, and Ernzerhof(PBE) [104]. Compared to LSDA, GGAs improve total energies, atomization energies, energy barriers, and structural energy differences [104] GGAs expand and soften bonds, a consequence that occasionally corrects and occasionally over-corrects the LSDA prediction. Also, GGAs typically prefer density inhomogeneity more strongly than LSDA [104].

For accurately describing the electronic structures of weakly correlated systems, the LSDA and GGA are ideal. Nevertheless, several DFT functionals exist for strongly correlated systems with well-localized states that are superior to LSDA- or GGA-based methods. Methods such as DFT+ Hubbard-U [105]–[109] and self-interaction correction[100] have been proposed over the years.

2.6.3. Hubbard U correction

The LSDA and GGA functionals provide good results for most of the solids but can fail when strong electron interactions are present in the systems. The latter systems are typically composed of rare-earth or transition metal atoms with partially filled d or f orbitals [110]. LSDA and GGA calculations may miss the localized nature of the strong correlations, occasionally leading to itinerant electron behavior and a metallic state instead of an insulating one [106]. This issue is highlighted in Mott

insulators [111], where the non-interacting band theory predicts a metallic state, but experiments reveal an insulating behavior [112]. The strength of the interaction between the electrons significantly impacts various features, such as magnetic exchange coupling, magnetic moment, etc [113], [114].

It is necessary to account correctly for the Coulomb interactions between the localized electrons to obtain the appropriate ground-state properties in strongly correlated systems. The so-called DFT+U scheme, which combines DFT and the Hubbard model [115]–[117], can be used to achieve this. The DFT+U method is a simple approach, with a low computational cost, to describe the Coulomb repulsion by adding a U correction to the DFT Hamiltonian. The general formulation of DFT+U energy functional, which is introduced by Anisimov and co-workers [105], [118], [119], is as follows:

$$E_{DFT+U}[n^{\sigma}(\mathbf{r}), \{\hat{n}^{\sigma}\}] = E_{DFT}[n^{\sigma}(\mathbf{r})] + E_{U}[\{\hat{n}^{\sigma}\}] - E_{dc}[\{\hat{n}^{\sigma}\}], \qquad (2.23)$$

where $\{\hat{n}^{\sigma}\}$ is the density matrix for correlated electrons with spin σ , which are typically d or f orbitals. $\mathrm{E}_{\mathrm{DFT}}[n^{\sigma}(\mathbf{r})]$ is the energy functional with the LSDA or GGA exchange-correlation approximation. $\mathrm{E}_{U}[\{\hat{n}^{\sigma}\}]$ is the energy term derived from the Hubbard Hamiltonian. $\mathrm{E}_{\mathrm{dc}}[\{\hat{n}^{\sigma}\}]$ is added to avoid the double-counting of the electronic interactions which are already partially included at the DFT level. There exist two formulations of the DFT+U we applied in this work. In Dudarev's approach [107], [109], only the difference between the Coulomb parameter U and exchange parameter U, (U-U), comes into play in the energy functional whereas in Liechtenstein's formulation [120] both U and U parameters separately come into play.

2.7. Plane waves and Pseudopotentials

As we have seen, DFT comprises various sophisticated models and approximations that describe in practice the interactions within many-body systems. We must accept certain numerical constraints to apply all of this theory to actual calculations on real systems. An appropriate basis set for the Kohn-Sham orbitals must be chosen to solve the DFT equations practically. One of the widely used methods is the plane wave pseudopotential method, which we used in this study.

The Kohn-Sham orbitals can be expanded on a plane waves basis set utilizing Bloch's theorem [121] as follows:

$$\psi_{\mathbf{k}v}(\mathbf{r}) = \sum_{\mathbf{G}} c_{v,\mathbf{G}+\mathbf{k}} \times \frac{1}{\sqrt{\Omega}} e^{i(\mathbf{G}+\mathbf{k})\cdot\mathbf{r}},$$
 (2.24)

where the sum runs over the reciprocal lattice vector \mathbf{G} , Ω is the volume of the unit cell and $c_{v,\mathbf{G}+\mathbf{k}}$ are the expansion coefficients of the wavefunction now expressed in terms of orthonormal plane waves. By substituting this expansion into Eq.(2.12),

we obtain the Kohn-Sham equations in reciprocal space for the expansion coefficient $c_{v,\mathbf{G}+\mathbf{k}}$. In the limit of an infinite number of G-vectors, the plane-wave expansion is exact. Nevertheless, since the number of expansion coefficients increases as $|\mathbf{G}+\mathbf{k}|^2$ increases, in practical calculations, one can deal with a finite number of wave vectors contained within a sphere of maximum energy cutoff:

$$\frac{\hbar^2}{2m_e} \mid \mathbf{G} + \mathbf{k} \mid^2 \le \mathbf{E}_{cut} \,. \tag{2.25}$$

In practical calculations, one should perform a preliminary investigation to determine the minimum number of wavefunctions (the minimum energy cut-off) that enables the total energy to converge. Once E_{cut} has been established, all electronic states must be expanded on the plane wave basis. This is computationally inconvenient, as a large number of plane waves are required to describe the system, especially if localized state are involved. The issue can be circumvented by distinguishing between core and valence electrons and assuming that the most of the relevant physics is due to the latter, while the former can be regarded as fixed in their atomic configuration [122] (frozen core approximation). So, instead of treating the core electrons directly, it is possible to introduce a pseudopotential (PP) [123], [124] that can reproduce how the real atomic potential interacts with the most outer states. The core electrons are described by a pseudo-wavefunction chosen to be smooth (nodeless) within a core cutoff radius from the core and to match the scattering properties of the whole system outside the core cut-off radius. In other words, the Kohn-Sham orbitals that come from an all-electron calculation outside the core-shell should match the single-particle orbitals that come from the PP.

There exist various families of pseudopotentials, which are determined by the position of the core cut-off radius, the mathematical structure of the PPs, the shape, and the conditions imposed on the pseudo-wavefunction. For norm-conserving pseudopotentials (NCPPs) [125], [126], a pseudo-wavefunction is formed under the requirement that the original full-potential wavefunction norm is preserved. The disadvantage of this condition is that in many systems, such as transition metals, a large number of PWs are needed to expand the wave function, which requires a high computational expense. This condition is relaxed for ultra-soft PPs (USPPs) [127] and Projector-Augmented Waves PPs (PAW) [128], [129] to reduce the number of G-vectors required to describe the variation of the pseudo-wavefunction in the core region, thereby reducing the cost of practical calculations. For USPPs [127], comparatively to other types of PPs, lower cut-off energy values are required while more empirical parameters are utilized. A feasibly more reliable alternative to USPPs is the PAW [128], [129], which tends to produce comparable results to USPPs but with better accuracy for specific materials. In this thesis, both USPPs and PAW are used in calculations.

2.8. Spin-orbit coupling

Relativistic effects such as spin-orbit coupling (SOC) originate from the Dirac equation [81], [82], which will be addressed in more detail in the next chapter. The SOC is responsible for phenomena such as the Rashba effect at metallic surfaces [130]–[132], non-collinear magnetism, and magnetic anisotropy [133]. The SOC is an effect that arises inside the atom and is given by coupling the electron's spin angular momentum with the orbital angular momentum. It usually splits states (typically ranging from a few to several hundred of meV) that are degenerate in a non-relativistic description. A derivation of the SOC can be found in textbooks on quantum mechanics such as [133]–[135], which is briefly addressed in the next chapter. In the case of a spherically-symmetric potential, as in an isolated atom, the associated Hamiltonian is:

$$\hat{\mathbf{H}}_{SOC} = \xi(r) \,\,\hat{\mathbf{S}} \cdot \hat{\mathbf{L}} \,\,\,\,(2.26)$$

where $\xi(r) = \frac{1}{2m_c^2c^2} \frac{1}{r} \frac{dV(r)}{dr}$ is SOC constant, c is the speed of light in vacuum, $\hat{\mathbf{S}}$ and $\hat{\mathbf{L}}$ are respectively the spin and angular momentum operators while V(r) is the nuclear electrostatic potential at a point located at a distance r from the center of the atom. Often, the SOC effect can be treated as a perturbation because it is smaller than the other contributions like kinetic or Hartree [136], [137]. The expression of the SOC in Eq.(2.26) becomes large at the vicinity of the nucleus. So, it is valid not only for isolated atoms but also for atoms in molecules and solids [133].

Due to SOC in an isolated isotropic atom, a change in the spin direction drags the orbital angular momentum along. In crystals, the spatial isotropy is broken. Therefore, the energy of the system is dependent on the alignment of the spherically asymmetric orbitals with the crystal's major axes. Consequently, because of the SOC, the energy of the system will also depend on the orientation of the magnetic moment. We refer to this phenomenon as magnetocrystalline anisotropy (MA).

2.9. The hyperfine interaction

The magnetic hyperfine interaction (HFI) is the interaction between the electron spin S and the nuclear spin I. While in the next chapter, we provide a detailed derivation of this interaction, we summarize here the important concepts and equations. The hyperfine Hamiltonian [59]–[61] reads:

$$\hat{H}_{HFI} = \hat{\mathbf{S}} \cdot \underline{\mathbf{A}}(\mathbf{R}) \cdot \hat{\mathbf{I}},$$
 (2.27)

where $\underline{\mathbf{A}}(\mathbf{R})$ is the hyperfine coupling tensor associated with the nucleus located at position \mathbf{R} , and the angular momenta are measured in units of \hbar . It consists of two contributions [60], $2S\mathbf{A}_{ij} = \mathbf{a}\,\delta_{ij} + \mathbf{b}_{ij}\,(i,j=x,y,z)$. The factor of 2S is needed to convert between the hyperfine parameters that enter Eq.(2.27) and the two contributions to the hyperfine field defined in Eqs. (2.28) and (2.29). Both quantities (a

and b) depend on the prefactor $P = \mu_0 g_e \mu_B g_N \mu_N$, with μ_0 the vacuum permeability, the electron and nuclear g-factors, g_e and g_N , and the Bohr and nuclear magnetons, μ_B and μ_N . We discuss the two contributions, a and b, without accounting for the effects of the spin-orbit interaction, which is consistent with the scalar-relativistic approximation adopted in our calculations.

The first contribution is called the Fermi contact term,

$$a = \frac{2P}{3} \rho_s(\mathbf{R}) . \tag{2.28}$$

It provides the isotropic part of the hyperfine interaction and originates from a finite electron spin density $\rho_s(\mathbf{r}) = \rho_{\uparrow}(\mathbf{r}) - \rho_{\downarrow}(\mathbf{r})$ at the position of the nucleus. This is usually the dominant contribution.

The second contribution is from the dipolar interaction between the electron and nuclear spin,

$$b_{ij} = \frac{P}{4\pi} \int d\mathbf{r} \, \frac{3r_i r_j - r^2 \delta_{ij}}{r^5} \, \rho_s(\mathbf{r}) \,. \tag{2.29}$$

Here **r** is relative to the nuclear position **R** and $r = |\mathbf{r}|$. The tensor \mathbf{b}_{ij} is traceless and has the angular symmetry of a quadrupole-like moment of the spin density, although heavily weighted towards the nucleus. It thus depends on the shape of the spin density and reflects the symmetry of the local atomic environment. Choosing the local cartesian axes to align with the principal axes of this tensor, we can discuss it in terms of its eigenvalues \mathbf{b}_{xx} , \mathbf{b}_{yy} and $\mathbf{b}_{zz} = -(\mathbf{b}_{xx} + \mathbf{b}_{yy})$.

2.10. Quantum ESPRESSO

The many-body Hamiltonian has been mapped onto a problem of self-consistent single-particle Kohn-Sham equations within the DFT framework. From the point of view of the numerical scheme, we used the open-source computer codes known as Quantum ESPRESSO (QE) [138]–[140], which is based on DFT, using a plane waves basis to expand the single-particle eigenstates of the Kohn-Sham equations and pseudopotentials (PPs) [123], [124] from the PSLibrary [141] to represent electron-ion interactions within the frozen-core approximation [122]. The SOC, which is essential for magnetocrystalline anisotropy, is taken into account by using fully-relativistic pseudopotentials (FR-PPs) [142], [143], which are generated by solving the atomic Dirac equation. Finally, the hyperfine parameters were computed with the GIPAW (Gauge Including Projector Augmented Waves) code, which is compatible with Quantum Espresso and uses the theory developed by Pickard and Mauri [144].

GIPAW is a method used to calculate hyperfine interactions in solids based on density functional theory (DFT) calculations. It is an extension of the PAW method,

which includes corrections for the relativistic and finite nuclear size effects on hyperfine interactions. It uses the magnetic response of the electrons in the material to calculate the hyperfine interactions. To perform GIPAW calculations with Quantum ESPRESSO, the following steps can be taken:

- Set up the crystal structure: Define the material's crystal structure and specify the atomic positions and types.
- Generate PAW potentials: Generate the PAW potentials for the material using the Quantum ESPRESSO pw.x code.
- Perform the GIPAW calculation: Use the Quantum ESPRESSO pw.x code with the GIPAW option to perform the DFT calculation with the GIPAW method.
- Analyze the results: Extract the hyperfine interaction parameters from the calculated results, such as the hyperfine coupling constants or isotropic shifts.

It is important to note that GIPAW calculations can be computationally demanding and may require significant computational resources. Therefore, care should be taken in choosing appropriate parameters and levels of accuracy to ensure reliable and accurate results. Additionally, GIPAW results should be validated against experimental data or other benchmark calculations to ensure their accuracy and reliability.

3. Theory of the hyperfine interactions

This chapter aims to derive the hyperfine and spin-orbit interactions from the Dirac Hamiltonian [81], [82]. In the previous chapter, we provided a short summary on the important aspects related to both interactions. The reader not interested in the details of the derivations can skip this chapter. Our starting point is the Dirac equation presented in [135]. Similar derivations are given in Refs. [59], [145]–[148].

3.1. Dirac Equation

The relativistic equivalent to the Schrödinger equation is the Dirac equation. We start with the Dirac Hamiltonian for a relativistic electron in an electromagnetic field described by a vector potential $\mathbf{A}(\mathbf{r})$ and a scalar potential $\phi(\mathbf{r})$. The Dirac Hamiltonian is given by

$$\hat{H}_{D} = c\alpha \cdot \pi + \beta mc^{2} - e\phi(\mathbf{r}) , \qquad (3.1)$$

where c is the speed of light in vacuum, the electron charge and rest mass are -e and m respectively, $\pi = \mathbf{p} + e\mathbf{A}(\mathbf{r})$ is the canonical momentum operator (\mathbf{p} is the momentum operator), and

$$\alpha = \begin{pmatrix} 0 & \sigma_i \\ \sigma_i & 0 \end{pmatrix}, \quad \beta = \begin{pmatrix} \mathbf{I}_2 & 0 \\ 0 & -\mathbf{I}_2 \end{pmatrix}, \tag{3.2}$$

are four-dimensional matrices constructed from the Pauli matrices σ_i , and the two-dimensional identity matrix, I_2 , defined as

$$\mathbf{\sigma}_x = \begin{pmatrix} 0 & 1 \\ 1 & 0 \end{pmatrix}, \quad \mathbf{\sigma}_y = \begin{pmatrix} 0 & -i \\ i & 0 \end{pmatrix}, \quad \mathbf{\sigma}_z = \begin{pmatrix} 1 & 0 \\ 0 & -1 \end{pmatrix}, \quad \mathbf{I}_2 = \begin{pmatrix} 1 & 0 \\ 0 & 1 \end{pmatrix}. \tag{3.3}$$

Since the Dirac Hamiltonian is a 4×4 matrix, the associated eigenstate Ψ to the eigenvalue equation (Dirac equation):

$$\hat{H}_{D}\Psi = E\Psi , \qquad (3.4)$$

is a four-component Dirac spinor

$$\Psi = \begin{pmatrix} \Psi_1 \\ \Psi_2 \end{pmatrix} , \qquad (3.5)$$

where Ψ_1 and Ψ_2 are two-component spinors describing respectively the electron and its anti-particle.

The Dirac equation can be rewritten as two coupled matrix equations:

$$(\epsilon' + e\phi(\mathbf{r}))\Psi_1 - c\mathbf{\sigma} \cdot \boldsymbol{\pi}\Psi_2 = 0 \tag{3.6}$$

and

$$(\epsilon' + 2mc^2 + e\phi(\mathbf{r}))\Psi_2 - c\mathbf{\sigma} \cdot \boldsymbol{\pi}\Psi_1 = 0, \qquad (3.7)$$

where $\epsilon' = \epsilon - mc^2$ is the electron energy relative to its rest-mass energy. We can estimate the relative magnitude of Ψ_1 and Ψ_2 from Eq.(3.6). Approximating $\sigma \cdot \pi \sim \mathbf{p} = mv$, where v is the electron velocity, and $\epsilon' + e\phi(\mathbf{r}) \sim \frac{1}{2}mv^2$ (kinetic energy), we obtain

$$\Psi_1 \sim \frac{c}{v} \Psi_2 \ . \tag{3.8}$$

For non-relativistic electrons $(\frac{c}{v} \gg 1) \Psi_1$, called the large component of the Dirac spinor, is much larger than Ψ_2 , called the small component of the Dirac spinor. After solving Eq.(3.7) for Ψ_2 , we get:

$$\Psi_2 = \frac{c}{\epsilon' + 2mc^2 + e\phi(\mathbf{r})} \,\mathbf{\sigma} \cdot \boldsymbol{\pi} \Psi_1 \ . \tag{3.9}$$

We insert Eq.(3.9) in Eq.(3.6) to obtain the eigenvalue equation for Ψ_1

$$\hat{\mathbf{H}}_1 \Psi_1 = \epsilon' \Psi_1$$

$$\left[-e\phi(\mathbf{r}) + \mathbf{\sigma} \cdot \mathbf{\pi} \frac{c^2}{\epsilon' + 2mc^2 + e\phi(\mathbf{r})} \mathbf{\sigma} \cdot \mathbf{\pi} \right] \Psi_1 = \epsilon' \Psi_1 . \tag{3.10}$$

By introducing the electric field, $\mathbf{E} = -\nabla \phi(\mathbf{r})$, and by using the property for two vector operators:

$$(\sigma \cdot \mathbf{X})(\sigma \cdot \mathbf{Y}) = \mathbf{X} \cdot \mathbf{Y} + i \sigma \cdot (\mathbf{X} \times \mathbf{Y})$$
 (3.11)

the Hamiltonian \hat{H}_1 can be re-expressed as:

$$\hat{H}_{1} = \frac{2mc^{2}}{\epsilon' + 2mc^{2} + e\phi(\mathbf{r})} \frac{\mathbf{p}^{2}}{2m} - e\phi(\mathbf{r}) + \hat{H}_{c} + \hat{H}_{L} + \hat{H}_{dip} + \hat{H}_{SOC} + \hat{H}',$$
(3.12)

where the term

$$\hat{\mathbf{H}}_{c} = \frac{e^{2} \hbar c^{2}}{(\epsilon' + 2mc^{2} + e\phi(\mathbf{r}))^{2}} \, \mathbf{\sigma} \cdot \mathbf{E} \times \mathbf{A}(\mathbf{r})$$
(3.13)

is called the Fermi contact interaction (isotropic hyperfine),

$$\hat{\mathbf{H}}_{L} = \frac{2e c^{2}}{\epsilon' + 2mc^{2} + e\phi(\mathbf{r})} \mathbf{A}(\mathbf{r}) \cdot \mathbf{p}$$
(3.14)

is the nuclear-orbital interaction

$$\hat{\mathbf{H}}_{\text{dip}} = \frac{e \, \hbar \, c^2}{\epsilon' + 2mc^2 + e\phi(\mathbf{r})} \, \mathbf{\sigma} \cdot (\nabla \times \mathbf{A}(\mathbf{r})) \tag{3.15}$$

is the dipolar hyperfine interaction (anisotropic hyperfine),

$$\hat{H}_{SOC} = \frac{e h c^2}{(\epsilon' + 2mc^2 + e\phi(\mathbf{r}))^2} \mathbf{E} \times \mathbf{p} \cdot \mathbf{\sigma}$$
(3.16)

is the spin-orbit interaction, and the last term of Eq.(3.12), \hat{H}' , contains relativistic effects which are independent of the spin σ of the electron such as the Darwin term [135].

3.2. Hyperfine interaction

3.2.1. Fermi contact interaction

The Fermi contact interaction (isotropic hyperfine), which is given by Eq.(3.13) can be further expanded for atomic structures. The underlying electron wavefunction is spread over many nuclei, each carrying a charge with a potential finite spin. A nuclear spin with charge Ze and magnetic moment $\mu_I = \gamma \hat{\mathbf{I}}$ (where γ is the nuclear gyromagnetic ratio and $\hat{\mathbf{I}}$ is the nuclear-spin operator) will generate an electric field of size ¹:

$$\phi(\mathbf{r}) = \frac{Ze}{4\pi\epsilon_0 r}, \quad \mathbf{E} = -\nabla\phi(\mathbf{r}) = \frac{Ze}{4\pi\epsilon_0 r^3} \mathbf{r} , \qquad (3.17)$$

and a vector potential

$$\mathbf{A}(\mathbf{r}) = \frac{\mu_0}{4\pi} \frac{\gamma \hat{\mathbf{I}} \times \mathbf{r}}{r^3} \ . \tag{3.18}$$

Using the above expressions for $\phi(\mathbf{r})$, \mathbf{E} , $\mathbf{A}(\mathbf{r})$, and the vector triple-product formula

$$\mathbf{r} \times (\hat{\mathbf{I}} \times \mathbf{r}) = \hat{\mathbf{I}}(\mathbf{r} \cdot \mathbf{r}) - \mathbf{r}(\hat{\mathbf{I}} \cdot \mathbf{r})$$
 (3.19)

in Eq.(3.13) for a non-relativistic electron ($\epsilon' \ll mc^2$), we can approximate the Fermi contact interaction by:

$$\hat{\mathbf{H}}_{c} = \mu_{0} \mu_{B} \gamma \delta_{T}(r) \left[\boldsymbol{\sigma} \cdot \hat{\mathbf{I}} - (\boldsymbol{\sigma} \cdot \hat{\mathbf{r}}) (\hat{\mathbf{I}} \cdot \hat{\mathbf{r}}) \right] , \qquad (3.20)$$

where $\mu_B = \frac{e\hbar}{2m}$ is the Bohr magneton, $\hat{\mathbf{r}} = \frac{\mathbf{r}}{r}$ is a radial unit vector, and

$$\delta_{\rm T}(r) = \frac{1}{4\pi r^2} \frac{r_{\rm T}/2}{(r + r_{\rm T}/2)^2} \ . \tag{3.21}$$

Here

$$r_{\rm T} = \frac{1}{4\pi\epsilon_0} \frac{Ze^2}{mc^2} = Z\alpha^2 a_0 , \qquad (3.22)$$

In the following we assume a constant electron g-factor of $g_e = 2$.

 $r_{\rm T}$ is called the Thomson radius, a_0 is the Bohr radius and α is the fine structure constant. We now consider the matrix elements of the Fermi contact Hamiltonian Eq.(3.20) with respect to two arbitrary states $|a\rangle$ and $|b\rangle$,

$$\langle a|\hat{H}_c|b\rangle = \mu_0 \mu_B \gamma \int d\mathbf{r} \, \delta_T(r) \Psi_a^*(\mathbf{r}) \left[\boldsymbol{\sigma} \cdot \hat{\mathbf{I}} - (\boldsymbol{\sigma} \cdot \hat{\mathbf{r}})(\hat{\mathbf{I}} \cdot \hat{\mathbf{r}}) \right] \Psi_b(\mathbf{r}) ,$$
 (3.23)

where $\Psi_a(\mathbf{r})$ and $\Psi_b(\mathbf{r})$ are spinors with components $\Psi_a(\mathbf{r}) = \langle \mathbf{r} | a \rangle$ and $\Psi_b(\mathbf{r}) = \langle \mathbf{r} | b \rangle$. Due to the $\delta_T(r)$ function, which limits significant contributions to distances less than or equal to the Thomson radius (r_T) , only the $s_{1/2}$ orbital will have a considerable size for s-symmetric orbitals, which explains that the contact interaction is solely a function of the s-orbitals. Since s-orbitals are spherically symmetric (isotropic), the angular part of the integral in Eq.(3.23) becomes:

$$\int d\Omega \left[\boldsymbol{\sigma} \cdot \hat{\mathbf{I}} - (\boldsymbol{\sigma} \cdot \hat{\mathbf{r}})(\hat{\mathbf{I}} \cdot \hat{\mathbf{r}}) \right] = \frac{4\pi}{3} \boldsymbol{\sigma} \cdot \hat{\mathbf{I}}. \tag{3.24}$$

Therefore, in a subspace spanned by s-orbitals ($\Psi_a(\mathbf{r})$ and $\Psi_b(\mathbf{r})$ are both s orbitals) the Fermi contact interaction reduces to:

$$\hat{\mathbf{H}}_{c} = \frac{4\mu_{0}}{3} \,\mu_{B} \gamma \delta_{T}(r) \,\boldsymbol{\sigma} \cdot \hat{\mathbf{I}} \,. \tag{3.25}$$

For an electron in the s-orbital ground state, Ψ_0 , the Fermi contact hyperfine Hamiltonian for the subspace of the orbital ground state can be written as:

$$\hat{\mathbf{H}}_{c,GS} = \langle \Psi_0 | \hat{\mathbf{H}}_c | \Psi_0 \rangle
= \frac{4\mu_0}{3} \mu_B \gamma \sum_r \sum_{r'} \langle \Psi_0 | r \rangle \langle r | \delta_{\mathrm{T}}(r) \boldsymbol{\sigma} \cdot \hat{\mathbf{I}} | r' \rangle \langle r' | \Psi_0 \rangle
= \frac{4\mu_0}{3} \mu_B \gamma \delta_{\mathrm{T}}(r) | \Psi_0(r) |^2 \boldsymbol{\sigma} \cdot \hat{\mathbf{I}} .$$
(3.26)

Since $\Psi_0(r)$ is the wave function for an electron in the orbital ground state in a periodic potential, this is equivalent to a Bloch function in a one-electron scheme. The radial integration is dominated by the region $r < r_T$. If we assume $r_T = 0$, the expression in Eq.(3.20) becomes:²

$$\hat{\mathbf{H}}_{c,GS} = \underbrace{\frac{2\mu_0}{3}\mu_B\mu_N g_N g_e \mid \Psi_0(\mathbf{R}) \mid^2 \mathbf{\sigma} \cdot \hat{\mathbf{I}}}_{,}$$
(3.27)

where $\Psi_0(\mathbf{R})$ stands for the one-particle wavefunction at the position of the nucleus \mathbf{R} . This mean that it is proportional to the probability of presence at the position of the nucleus. Since only s-wavefunctions are nodeless at \mathbf{R} , this implies that the a-parameter arises from only such contributions and thus effectively probes for the

²We substitute $g_e = 2$ and $\gamma = g_N \mu_N$, g_N is the g-factor for the nucleus, μ_N is the nuclear magneton $(\mu_N = \frac{e\hbar}{2m_p})$ and m_p is the proton mass.

s-like character of a system. The quantity $|\Psi_0(\mathbf{R})|^2 \sigma$ gives rise to the spin density vector. The length of the vector is given by the difference between spin-up and spin-down electrons, i.e. $\rho_s(\mathbf{r}) = \rho_{\uparrow}(\mathbf{r}) - \rho_{\downarrow}(\mathbf{r})$ at the position of the nucleus \mathbf{R} . Thus the Fermi contact hyperfine constant can also be written as:

$$a = \frac{2\mu_0}{3}\mu_B \mu_N g_N g_e \rho_s(\mathbf{R}) , \qquad (3.28)$$

already given in Eq.(2.28). From Eq.(3.28) the a-parameter depends on the g-factor for the nucleus g_N , this means that two magnetic isotopes of the same chemical element have two distinctive isotropic hyperfine couplings.

3.2.2. Dipolar hyperfine interaction

The dipolar hyperfine interaction Eq.(3.15) depends on the magnetic field **B** generated by the nuclear magnetic moment $(\mu_I = \gamma \hat{\mathbf{I}})$:

$$\mathbf{B} = \nabla \times \mathbf{A}(\mathbf{r}) = \frac{\mu_0}{4\pi r^3} \gamma \left[3\hat{\mathbf{r}} (\hat{\mathbf{I}} \cdot \hat{\mathbf{r}}) - \hat{\mathbf{I}} \right] . \tag{3.29}$$

Substituting the above expression into Eq.(3.15) gives:

$$\hat{\mathbf{H}}_{\text{dip}} = \frac{e \, \hbar \, c^2}{\epsilon' + 2mc^2 + e\phi(\mathbf{r})} \, \frac{\mu_0}{4\pi} \gamma \, \frac{3(\boldsymbol{\sigma} \cdot \hat{\mathbf{r}})(\hat{\mathbf{I}} \cdot \hat{\mathbf{r}}) - \boldsymbol{\sigma} \cdot \hat{\mathbf{I}}}{r^3} \, . \tag{3.30}$$

For a non-relativistic electron, using $\hat{\mathbf{S}} = \mathbf{\sigma}/2$, inserting for $\phi(\mathbf{r})$ (Eq.3.17), and after some algebra the above equation becomes:

$$\hat{\mathbf{H}}_{\text{dip}} = \frac{2\mu_0}{4\pi} \mu_B \gamma f_{\text{T}}(r) \frac{3(\hat{\mathbf{S}} \cdot \hat{\mathbf{r}})(\hat{\mathbf{I}} \cdot \hat{\mathbf{r}}) - \hat{\mathbf{S}} \cdot \hat{\mathbf{I}}}{r^3} , \qquad (3.31)$$

where

$$f_{\rm T}(r) = \frac{r}{r + r_{\rm T} / 2} \tag{3.32}$$

If we assume $r_T = 0$, $f_T(r) = 1$ then the dipolar hyperfine interaction in Eq.(3.31) becomes:

$$\hat{\mathbf{H}}_{\text{dip}} = \frac{\mu_0}{4\pi} \mu_B \mu_N g_N g_e \frac{3(\hat{\mathbf{S}} \cdot \hat{\mathbf{r}})(\hat{\mathbf{I}} \cdot \hat{\mathbf{r}}) - \hat{\mathbf{S}} \cdot \hat{\mathbf{I}}}{r^3} , \qquad (3.33)$$

3.2.3. Nuclear-orbital interactions

The nuclear-orbital interaction in Eq.(3.14) describes the coupling between a nuclear magnetic moment μ_I and an electron orbital magnetic moment $\hat{\mathbf{L}} = \mathbf{r} \times \mathbf{p}$. By inserting $\phi(\mathbf{r})(\text{Eq.3.17})$ and the vector potential Eq. (3.18) in Eq.(3.14), we get:

$$\hat{\mathbf{H}}_{L} = \frac{2e\,c^{2}}{\epsilon' + 2mc^{2} + \left(\frac{Ze}{4\pi\epsilon_{0}r}\right)} \frac{\mu_{0}}{4\pi} \mu_{N} g_{N} \left(\frac{\hat{\mathbf{I}} \times \mathbf{r}}{r^{3}}\right) \cdot \mathbf{p} \ . \tag{3.34}$$

Using the vector identity $\mathbf{A} \cdot (\mathbf{B} \times \mathbf{C}) = \mathbf{B} \cdot (\mathbf{C} \times \mathbf{A}) = (\mathbf{C} \times \mathbf{A}) \cdot \mathbf{B}$ gives:

$$\hat{\mathbf{H}}_{\mathbf{L}} = \frac{2e\,c^2}{\epsilon' + 2mc^2 + \left(\frac{Ze}{4\pi\epsilon\sigma r}\right)} \frac{\mu_0}{4\pi r^3} \mu_N g_N \hat{\mathbf{L}} \cdot \hat{\mathbf{I}} \ . \tag{3.35}$$

For a non-relativistic electron ($\epsilon' \ll mc^2$) and using some algebra Eq.(3.35) becomes:

$$\hat{\mathbf{H}}_{L} = \frac{\mu_0}{4\pi} \frac{\mu_B \mu_N g_N g_e}{r^3} f_{\mathrm{T}}(r) \hat{\mathbf{L}} \cdot \hat{\mathbf{I}}. \tag{3.36}$$

If we neglect the effect of the finite Thomson radius by setting $r_T = 0$, which leads to $f_T(r) = 1$, the above equation becomes:

$$\hat{\mathbf{H}}_{\mathbf{L}} = \frac{\mu_0}{4\pi} \frac{\mu_B \mu_N g_N g_e}{r^3} \hat{\mathbf{L}} \cdot \hat{\mathbf{I}}. \tag{3.37}$$

In contrast to the Fermi contact term, the s-orbitals do not contribute to both the dipolar and orbital hyperfine interactions. The latter are substantial for other orbitals (p- and d-orbitals). In our thesis, we neglect effects induced by spin-orbit coupling because it was previously found to have a small effect on the computed hyperfine interactions for transition metal centers and even for heavy atoms [149], [150].

3.2.4. Hyperfine Interaction Parameters

When nuclear-orbital interaction, \hat{H}_L , is ignored, the Hamiltonian for the hyperfine interaction can be written as:

$$\hat{H}_{HFI} = \hat{\mathbf{S}} \cdot \underline{\mathbf{A}}(\mathbf{R}) \cdot \hat{\mathbf{I}} , \qquad (3.38)$$

where $\underline{\mathbf{A}}(\mathbf{R})$ is the hyperfine coupling tensor associated with the nucleus located at position \mathbf{R} , and the angular momenta are measured in units of \hbar . When the Fermi contact and dipolar contributions are included, the hyperfine interaction coupling tensor can be expressed as follows:

$$\mathbf{A}_{ij} = \mathbf{a}\,\delta_{ij} + \mathbf{b}_{ij} \ . \tag{3.39}$$

The a term has been already defined in Eq.(3.28). It is isotropic and corresponds to the Fermi contact interaction term. The tensor b_{ij} is anisotropic due to the dipolar term Eq.(3.33), and consists of the terms:

$$b_{ij} = \frac{\mu_0}{4\pi} \mu_B \mu_N g_N g_e \int d\mathbf{r} \, \frac{3r_i r_j - r^2 \delta_{ij}}{r^5} \, \rho_s(\mathbf{r}) \,.$$
 (3.40)

Here **r** is relative to the nuclear position **R**, $r = |\mathbf{r}|$, (i, j = x, y, z) and $\sum_{ii} b_{ii} = 0$, i.e., it is tracless.

3.3. Spin-orbit interaction

The last term originating from the Dirac equation that we consider is the spin-orbit interaction Eq.(3.16). In the non-relativistic limit, this term can be written as:

$$\hat{\mathbf{H}}_{SOC} = \frac{e \hbar c^2}{(\epsilon' + 2mc^2 + e\phi(\mathbf{r}))^2} \mathbf{E} \times \mathbf{p} \cdot \mathbf{\sigma} \simeq \frac{e \hbar}{4m^2c^2} \mathbf{E} \times \mathbf{p} \cdot \mathbf{\sigma}.$$
 (3.41)

The spin-orbit interaction couples the spin degrees of freedom σ of the electron to its orbital degree of freedom (**p**). In the presence of the electric field generated by a charged nucleus Eq.(3.17), the spin-orbit coupling takes the well-known form already introduced in the previous chapter in section 2.8:

$$\hat{\mathbf{H}}_{SOC} = \xi(r)\,\hat{\mathbf{S}}\cdot\hat{\mathbf{L}} \ . \tag{3.42}$$

As a reminder, $\xi(r) = \frac{1}{2m^2c^2}\frac{1}{r}\frac{dV(r)}{dr}$ is SOC constant, $\hat{\mathbf{S}}$ and $\hat{\mathbf{L}}$, as a reminder, are respectively the spin and angular momentum operators while $V(r) = e\phi(\mathbf{r})$ is the nuclear electrostatic potential at a point located at a distance r from the center of the atom.

4. Hyperfine fields of magnetic adatoms on ultrathin insulating films

A recent breakthrough in quantum technologies was recently achieved by employing novel scanning tunneling microscopy techniques to demonstrate nuclear magnetometry of single magnetic adatoms. Atomically-resolving the weak hyperfine interaction between the nuclear and electron spins is the initial step toward realizing quantum devices based on individual nuclear spins well-shielded from environmental disturbances. The intriguing aspect in those experimental works is that successful measurements on the hyperfine interaction have been carried out only for a few chemical species adsorbed on two-layer thick MgO.

In order to acquire a broader view of this emergent topic, we present in this chapter an extensive first-principles computational investigation of the hyperfine interaction tensor of the whole series of 3d transition-metal adatoms deposited on various thicknesses of insulating thin films of experimental interest. We address MgO, NaF, NaCl, h–BN, and Cu₂N films, identify the atoms and substrates triggering the most efficient hyperfine interactions, and uncover the relevant trends. We proceed to a detailed analysis of the physical mechanisms. Finally, we summarize our findings in a valuable map (see Fig. 4.11) of the hyperfine interactions that will guide the corresponding experimental and theoretical communities. The topic of hyperfine interactions within single magnetic adatoms on surfaces remains unexplored. It is certainly of great interest to the broad quantum computational and experimental community aiming at exploring hyperfine interactions and nuclear spins to encode quantum information.

Results presented in this chapter have already been published in [151]: Shehada et al., Npj Comput. Mater. 7, 87 (2021).

4.1. Introduction

As elaborated in the Introduction chapter, in recent years, magnetic atoms on surfaces have gained considerable attention due to their potential in quantum technology applications. Besides the electronic magnetic moments, nuclear spins have also been proposed for application purposes. The two are coupled via the hyperfine interaction (see chapter 3), which offers insight into the electronic structure and chemical bonding

of atoms, molecules, and solids, as explored with nuclear magnetic resonance techniques [62]. In comparison to electron spin moments, individual nuclear spin states tend to have a much longer lifetime and hold in principle a greater promise as building blocks for quantum computers [1]–[6].

Recently, two significant steps were achieved experimentally through the development of single-atom STM EPR/ESR setup [33], [36], [39], [40], [42]–[45], [52], [63]–[68], [71] (see Fig. 1.1): the detection of the hyperfine interaction between the atomic nucleus and surrounding electrons for single Fe and Ti adatoms on MgO/Ag(001) [42], [44], [45] and the control of the nuclear polarization of individual Cu adatoms on the same surface [43]. The actual mechanism underpinning the EPR/ESR experiments is still under investigation [67], [73]–[78], but it is clear that a deep understanding of the hyperfine interactions in these systems is an essential piece of the puzzle. Moreover, the interactions were detected intriguingly only for a few set of atoms on a two-layers thick MgO film.

In this chapter, we report on systematic first-principles calculations of the hyperfine interactions for magnetic transition metal adatoms (from Sc to Cu) placed on different ultrathin insulators with different thickness and bonding site, namely MgO, NaF, NaCl, h–BN and Cu₂N. We note that conventional STM investigations of magnetic adatoms on thin insulating layers have mainly focused on Cu₂N [22]–[27], [32] and MgO [7], [8], [33]–[53], with lesser research on h-BN [28], [30], [31].

A summary of our findings is given in Fig. 4.11 for both contributions to the hyperfine interactions, which are measurable experimentally [42], [44], [45]: the Fermi contact and dipolar terms. Our findings enable the identification of the adatom-substrate complexes with the largest interactions and those that can even experience a sign change of the interaction, translating to an antiferromagnetic nuclear-electron spin coupling. Our analysis reveals the trends and the dependence of the computed hyperfine parameters on various factors, such as the filling of the magnetic d-orbitals of the adatom and the type and strength of bonding with the substrate. We also examine the thickness of the ultrathin film for MgO, NaF, and NaCl and two choices of binding sites. We show how the hyperfine interactions give access to information on the local electronic structure and address the main quantities that determine their properties. The obtained map of interactions can serve as a guide for future experimental explorations of nuclear-electron spin physics of adatoms and complex nanostructures on surfaces.

4.2. Computational details

As reported in chapters 2 and 3, our first-principles calculations have been carried out in the framework of the DFT as implemented in the Quantum Espresso code [138]–[140] to obtain structural, electronic, and magnetic properties. Here, we used pseu-

dopotentials from the PSLibrary [141] and the projector augmented wave (PAW) method [152]. Exchange and correlation effects were treated in the generalized gradient approximation (GGA) of Perdew, Burke and Ernzerhof (PBE) [104]. The hyperfine parameters in Eqs. 2.28 and 2.29 were computed with the GIPAW module of Quantum Espresso based on the theory developed by Pickard and Mauri [144].

Since it was previously found that the spin-orbit interaction has negligible effect on the computed hyperfine parameters for transition metal centers and even for heavy atoms (see for example Refs. [149], [150]), we did not account for it in the current study, which is consistent with the scalar-relativistic approximation adopted in our calculations. For all calculations, the kinetic energy cutoff for the wavefunctions and for the charge density were set to 90 Ry and 720 Ry, respectively. The Brillouin zone integrations were performed with a Gaussian smearing of width 0.01 Ry.

The tests on the impact of the Hubbard-U correction on the hyperfine parameters were investigated with the simplified rotationally-invariant scheme proposed by Dudarev [107] according to the methodology of Cococcioni and de Gironcoli [109]. For the calculations of isolated atoms, we employed cubic periodic cells with length 10 Å to minimize interactions between periodic replicas of the atom, and Γ -point sampling of the Brillouin zone. In order to determine the theoretical lattice constants, we constructed monolayer, bilayer and trilayer geometries with 4 atoms per layer for MgO, NaF and NaCl, and 3 and 2 atoms for monolayers of Cu₂N and h–BN, respectively. In all cases, we included a vacuum thickness equivalent to 9 layers of the respective materials, and the k-mesh was set to $12 \times 12 \times 1$. The results are collected in Table 4.1.

Material	Experimental lattice constants	Monolayers	Bilayers	Trilayers
MgO	4.2113 [153] (bulk)	4.0530	4.1466	4.1846
NaCl	5.6418 [154] (bulk)	5.6710	5.5941	
NaF	4.6324 [155] (bulk)	4.6555	4.6109	
Cu_2N	3.814 [156] (monolayer)	3.6637	_	
h– BN	2.50 [157] (monolayer)	2.5153		_

Table 4.1.: Experimental vs. theoretical lattice constants for the considered systems.

To accommodate the adatoms on MgO, NaF and NaCl, we then set up 3×3 supercells with one of the 3d adatoms either on top of the anion or in the bridge position, as shown in Fig. 4.1, with a consistent reduction of the k-mesh $4 \times 4 \times 1$. The supercells contained 37, 73 and 109 atoms for monolayers, bilayers and trilayers, respectively, and a vacuum thickness equivalent to 9 layers of the respective materials, as before. The cell dimensions were kept fixed while all atomic positions were allowed to fully relax. A similar procedure was followed for the 3d adatoms on top of nitrogen for the monolayers of Cu_2N (28 atoms) and h–BN (19 atoms), with a vacuum thickness of $16.5\,\text{Å}$ and $16.3\,\text{Å}$, respectively. For the relaxation distance of 3d adatoms on monolayer h–BN, we additionally take into account weak interactions — the van der Waals

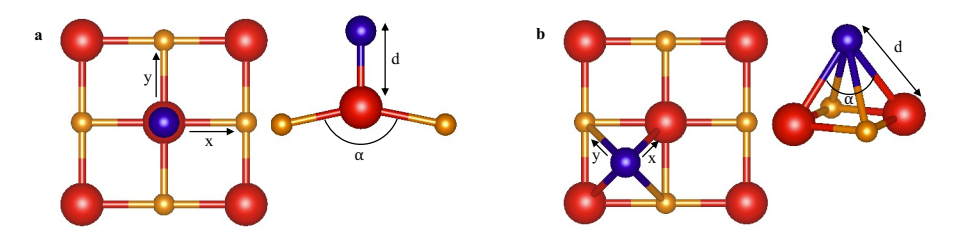


Figure 4.1.: Geometry of adatoms on MgO, NaF and NaCl. Top and side views of (a) adatom stacked on top of anion and (b) adatom in the bridge position. The adatom is represented by a blue sphere, the anion by a red sphere and the cation by an orange sphere. The definition of the distance d between the adatom and anion and the cation-anion-cation bond angle α is also illustrated.

correction (DFT-D) — to improve the description of the binding energy.

In this chapter and the rest of the thesis, we report the calculated Fermi contact and dipolar hyperfine interaction per nuclear g-factor, making them applicable to all isotopes of the 3d elements. Furthermore, for easier comparison with experimental measurements of these quantities, we convert them to frequency units (e.g. GHz) using Planck's constant.

4.3. Reference atomic calculations

In order to set the stage for our study of the 3d adatoms (Sc–Cu) deposited on different ultra-thin insulating layers, we first explore the case of isolated 3d atoms so that the substrate and its influence are excluded. We present the electronic and magnetic properties and the hyperfine parameters for isolated 3d atoms (Sc–Cu). These results provide a clear picture of the origin of the hyperfine interaction within our computational method, and serve as benchmarks for comprehending the behavior of the same atoms when placed on various ultra-thin insulating layers.

The most fundamental magnetic property of an isolated atom is its electron spin magnetic moment ($\mu_s = 2\mu_B \mathbf{S}/\hbar$), depicted in Fig. 4.2a. As predicted, most of the spin magnetic moment values follow Hund's first rule, with the exceptions of Cr and Cu and two additional cases involving Ti and V. These exceptions are explained by the spin-polarized atomic energy levels illustrated in Fig. 4.2b. In atomic physics, Cr and Cu are the well-known exceptions to Hund's first rule. In the case of Cr, the s-up and d-up energy levels are lower than the s-down and d-down energy levels, stabilizing the electronic configuration [Ar] $4s^13d^5$, corresponding to the increase in stability caused by the d-shell being only half-filled. For Cu, the s-down level has higher energy than

all the other levels, leading to the electronic configuration [Ar] $4s^13d^10$, where it is known that a full d-shell is more stable than a full s-shell.

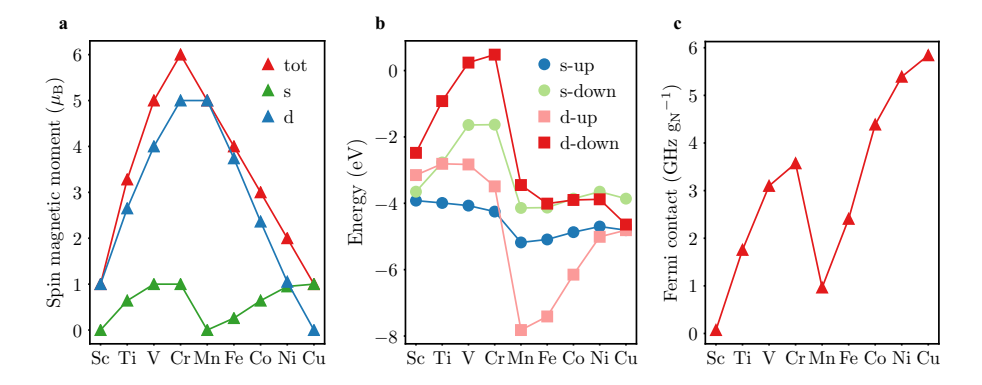


Figure 4.2.: Basic properties of isolated 3d transition metal atoms. (a) Spin magnetic moment, (b) spin-polarized energy levels and (c) Fermi contact contribution to the hyperfine interaction of isolated 3d transition metal atoms.

V and Ti are computational exceptions with no analog in atomic physics, and they illustrate potential issues with the computational approach for isolated cases. The computed atomic energy levels for V are arranged in the same order as they are for Cr, favoring the [Ar] $4s^13d^4$ electronic configuration (see Fig. 4.2b). The properties of V impurities have previously been shown to be sensitive to the exchange-correlation functional [158], with a spin magnetic moment of $3\mu_{\rm B}$ within the generalized gradient approximation (GGA) and $5\mu_{\rm B}$ for the local spin density approximation (LSDA) calculation. In our case, this sensitivity can also depend on the chosen pseudopotentials. Ti demonstrates what happens when two energy levels become nearly degenerate in energy (closer than the employed smearing for the occupations). Its calculated spin moment of $\mu_{\rm s}=3.28\,\mu_{\rm B}$ is the outcome of distributing three electrons among the d-up and the s-down levels due to this near-degeneracy. Despite the issues encountered for two isolated atoms, it is still instructive to analyze and explore the overall trend of the respective hyperfine interaction as a function of the atomic magnetic moments.

Because of the computational spherical symmetry of the isolated 3d atoms, only the Fermi contact contribution of the hyperfine interaction is finite, and their values are shown in Fig. 4.2c. Its magnitude increases steadily as we go from Sc to Cr, then drops suddenly for Mn and returns to steadily increasing until Cu. In order to clarify this behavior, we have to decompose the total spin moment of the free atom into contributions coming from its s and d electrons, as shown in Fig. 4.2a. We see that the Fermi contact contribution follows the behavior of the s contribution [61] to the total spin moment (S-spin moment), and so is a useful experimental probe of this otherwise hard to measure quantity.

Eq. (2.28) illustrates that the relevant quantity is the spin density at the nuclear position, $\rho_s(\mathbf{R})$, which arises purely from the s electrons. This immediately explains the huge drop in the Fermi contact contribution for Mn, as the s-shell becomes full and so $\rho_s(\mathbf{R})$ becomes significantly reduced in comparison to Cr. Nevertheless, a full s-shell does not imply a vanishing Fermi contact contribution, as the s-up and s-down wave functions have a different spatial dependence due to the exchange splitting of the atom, and thus a full compensation in $\rho_s(\mathbf{R})$ will not be achieved. This mechanism applies to the spin-polarized s core electrons as well In addition, as the atomic number increases, the s wave functions contract toward the nucleus, which explains the overall trend of the Fermi contact contribution to increase when going from Sc to Cu.

4.4. Adatoms on 1-3 layers of MgO

In this section, our investigation will focus on the 3d adatoms (Sc–Cu) deposited on a few layers of MgO. We report on adatoms that have been experimentally examined with STM [8], [33]–[36], [42]–[45], [52], [63]–[67] and those for which no measurements have been previously reported. We notice that the hyperfine interaction was only measured for three atomic species on a two-layer MgO/Ag(001) surface.

The measured values $1.93\,\mathrm{GHz}~\mathrm{g_N}^{-1}$ for the two isotopes $^{63}\mathrm{Cu}$ and $^{65}\mathrm{Cu}$ were reported in Ref. [43] and $1.28\,\mathrm{GHz}~\mathrm{g_N}^{-1}$ for $^{57}\mathrm{Fe}$ in Ref. [42]. For Fe we take into account the conversion factor of 2S=4 explained after Eq. (2.27). The Cu and Fe adatoms measurements could not distinguish between the Fermi contact and dipolar contributions to the hyperfine interaction. As we found that the dipolar contribution is small compared to the Fermi contact contribution (5% for Cu and 10% for Fe), we make the approximation of assigning these values solely to the Fermi contact value in order to compare them with our theoretical results. In addition, Ref. [42] provides measurements for the two isotopes $^{47}\mathrm{Ti}$ and $^{49}\mathrm{Ti}$ with a separation between Fermi contact and dipolar contributions, see Eqs. (2.28) and (2.29). For Ti on the oxygen-top position, the experimental values are a = 54 MHz g_N⁻¹ for the Fermi contact and b_{zz} = 54 MHz g_N⁻¹ for the dipolar contribution, while on the bridge position the measured Fermi contact value is a = 160 MHz g_N⁻¹, and the dipolar contribution is quantified by b_{zz} = 34 MHz g_N⁻¹. Nevertheless, in the experiment Ti was found to be hydrogenated, a situation that was not considered in our calculations.

We begin by discussing the considered structures and relaxed geometries: the adatoms sit either on top of an oxygen with up to three layers of MgO (Fig. 4.1a), or in a bridge position with up to two MgO layers (Fig. 4.1b). Generally, adsorption on top of oxygen is the most energetically favored (Fig. 4.3 a). However, we take into account both adsorption positions because STM experiments can manipulate the adatoms between them [42]. The preferred position has three main exceptions: (i and ii) Sc and Ti on a single layer of MgO, the energy differences between the

bridge and the oxygen-top positions are relatively small ($\Delta E \approx 40\,\mathrm{meV}$). However, the stability of the oxygen-top position is significantly higher for the two-layers case ($\Delta E \approx 0.6\,\mathrm{eV}$). (iii) Ni shows a strong sensitivity to the MgO thickness, switching from the oxygen-top position for the monolayer to the bridge position for the two layers. The structural properties agree with those of earlier studies [159]–[161].

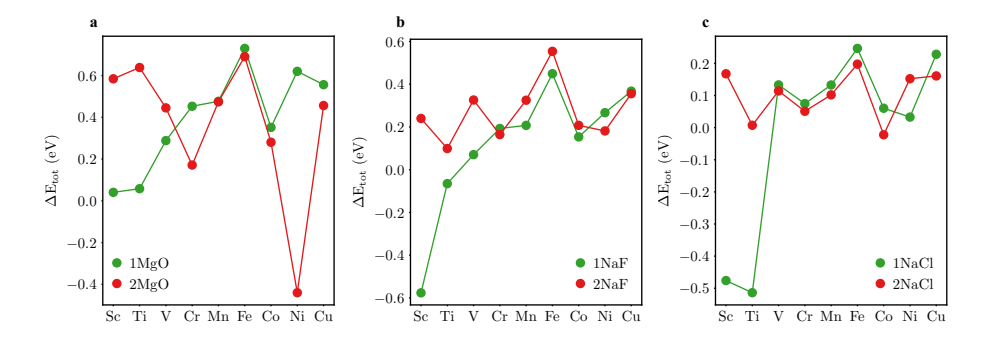


Figure 4.3.: Total energy of adatoms on the bridge position relative to the one for the anion-top position energy, calculated for structures relaxed within GGA-PBE. Ultra-thin films: (a) MgO, (b) NaF and (c) NaCl. The number to the left of the chemical formula in the legend indicates the number of layers in the ultra-thin film.

The adatoms on the oxygen-top position exhibit the following structural trends. The adatoms lead to a deformation of the angle α between O and the neighboring Mg (see Fig. 4.1a), which is more pronounced for a single MgO layer (between 150° and 165°) than for two or three MgO layers (between 160° and 175°). This deformation becomes less pronounced when switching from Sc to Cu (see Fig. 4.4 a). The average distance between the 3d adatoms and the O atom below is 1.90 Å for a single layer of MgO, and it increases slightly for two and three layers of MgO, with the most significant increase for V (see Fig. 4.4 b). This increase for V causes an important effect that will be discussed below.

The geometry of the bridge position is more complicated than the oxygen-top position. In order to characterize it, we calculated the O-adatom-O and Mg-adatom-Mg angles, as well as the distances between the adatom and the closest O and Mg atoms (see Fig. A.1 of Appendix). In general, the square formed by the two Mg and O atoms surrounding the adatom demonstrates significant buckling. The O-adatom-O and Mg-adatom-Mg angles (see Fig. 4.1b) for both one and two layers of MgO are typically within the range of 60° to 80°. The different distances between the adatom and either Mg or O make the buckling more evident. These distances have a large spread for the considered adatoms (2.3 Å to 2.9 Å), with Cr having the largest distance to the neighboring atoms and so the smallest buckling.

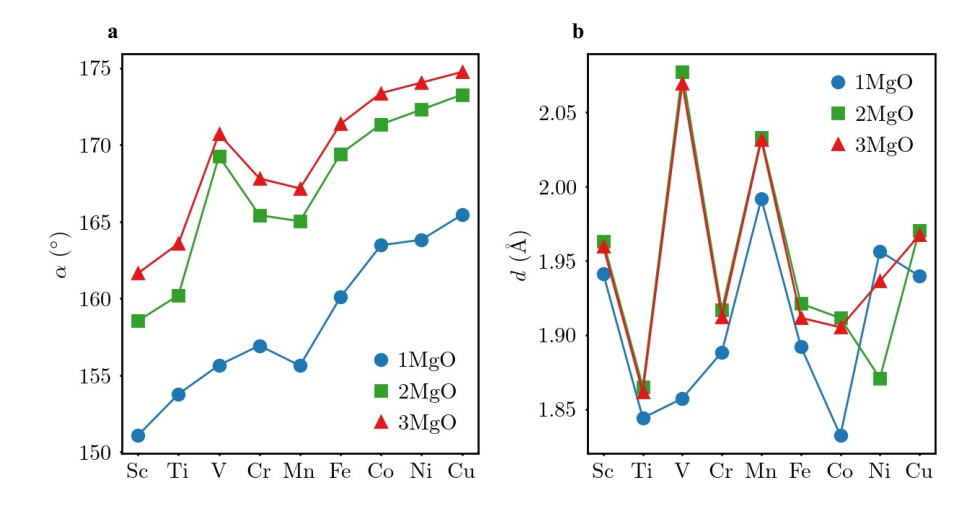


Figure 4.4.: Relaxed geometrical properties of adatoms on MgO ultra-thin films, placed on top of oxygen. (a) Mg-O-Mg bond angle and (b) distance between the adatom and oxygen. The number to the left of the chemical formula in the legend indicates the number of layers.

Fig. 4.5 shows the magnetic properties of the adatoms on the oxygen-top position. The spin moments of the adatoms are generally unaffected by the number of MgO layers, as shown in panel a. The spin moment of most adatoms follows Hund's first rule and is consistent with a nominal valence of $[Ar]4s^23d^n$. The contribution of the Fermi contact to the hyperfine interaction is depicted in Fig. 4.5b. The experimental measurements of the Fermi contact for Ti, Fe [42] and Cu [43] both on top of an oxygen and bridge positions (Ti) of two layers of MgO/Ag(001) surface agree well with our results. The Fermi contact overall magnitude is fairly reduced compared to the free-atom case (cf. Fig. 4.2c), consistent with a nominally full 4s shell.

The jump in the spin moment of V with increasing MgO thickness is caused by a change in valence from $4s^23d^3$ (low-spin) to $4s^13d^4$ (high-spin), which also causes a sudden change in the Fermi contact value. This occurs because the spin moment and Fermi contact approach the free-atom value as the distance between V and O increases. This is clearly seen in the modification of the underlying electronic structure shown in Fig. 4.6. The other noteworthy oddity is Ni, which has a small spin moment of about $0.8\,\mu_{\rm B}$ placed on top of O and $2.0\,\mu_{\rm B}$ when placed on the bridge position (see Fig. 4.2d). Theoretically, the site-dependent magnetism of Ni on MgO has already been identified [162]. The spin state of V and Ni is also affected by the exchange-correlation function chosen, according to Ref. [159] For all MgO thicknesses,

the Fermi contact contribution of Ni lies outside the expected trend of the curve, with a weak and negative value at the oxygen-top position (see Fig. 4.6b). The antiparallel alignment of the contribution to the spin moment of Ni coming from the s-electrons with respect to one of the d-electrons leads to a negative value of the Fermi contact contribution.

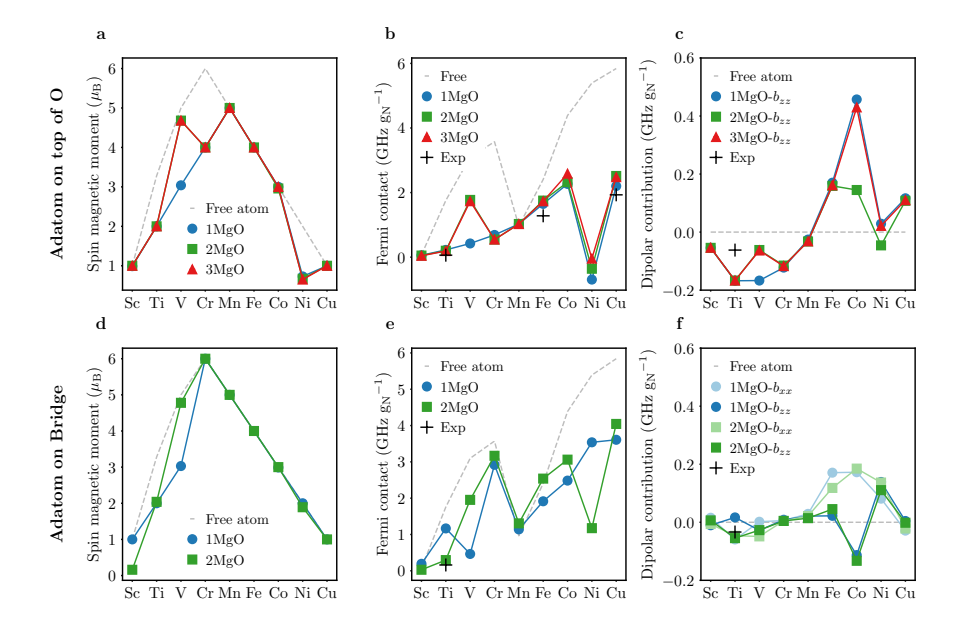


Figure 4.5.: Magnetic properties of adatoms on MgO ultra-thin films, placed on top of oxygen (a–c) and on the bridge position (d–f). (a,d) Spin magnetic moment, (b,e) Fermi contact and (c,f) dipolar contributions to the hyperfine interaction. The number to the left of MgO in the legend indicates the number of layers in the ultra-thin film. The gray dash line represent the free-atom results. The black crosses in panels (b,c) and (e,f) refers to the experimental results for Fe and Ti from Ref. [42] and for Cu from Ref. [43].

Putting the 3d adatoms on the MgO substrate leads to a shape deformation of the spin density that gives rise to a dipolar contribution to the hyperfine interaction, shown in Fig. 4.5c. Because of the C_{4v} symmetry observed in the oxygen-top position (see Fig. 4.1a), we show only the dipolar parameter b_{zz} , where z corresponds to the direction normal to the MgO layer and aligns with the orientation of the adatom-oxygen bond. Eq. (2.29) implies that the spherical part of the spin density does not contribute, so the dipolar contribution is not present for the free atoms. Thus,

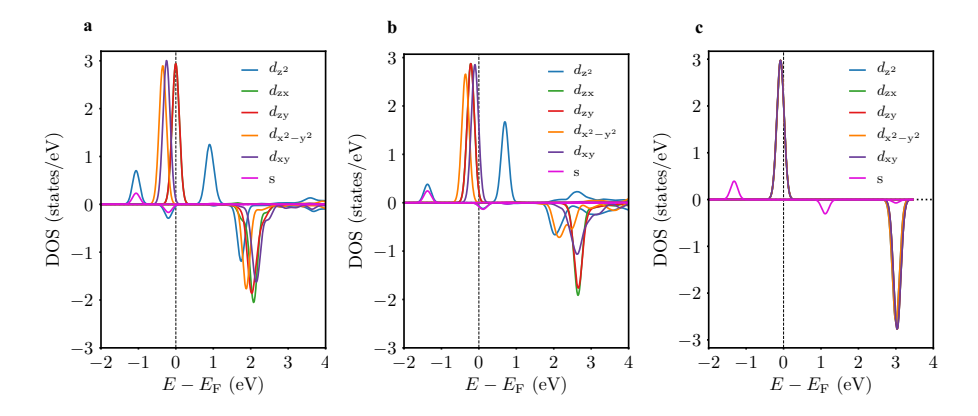


Figure 4.6.: Thickness dependence of the electronic structure of a V adatom on MgO in the oxygen-top position. (a) One monolayer of MgO. (b) Two monolayers of MgO. (c) Free atom. The Fermi energy is marked by a vertical dashed line.

in contrast to the Fermi contact contribution, we now expect the signal from the d electrons to be more important than the ones from the spherically-symmetric s electrons.

Another critical factor is that an ideal half-filled d-shell is spherically symmetric and should lead to a vanishing value of the dipolar contribution, as is indeed seen for Mn. In the case of Sc-Mn, the spin density is formed mainly by d-up electrons, while Fe-Cu have a dipolar contribution that originates on the d-down electrons, as their d-up shells are fully occupied. Since $\rho_s(\mathbf{r}) = \rho_1(\mathbf{r}) - \rho_1(\mathbf{r})$, the change in the sign of the dipolar contribution is anticipated when going from the first to the second group of adatoms, under the assumption that the deformation of the spin density is governed by the strong interaction with oxygen and so has the same shape for all adatoms. The behavior of the dipolar contribution of Co and V differs in response to changes in their atomic environment. For example, when transitioning from one to three MgO layers, the dipolar contribution for Co exhibits a high sensitivity to small changes. In contrast, the spin moment and Fermi contact contribution show weaker sensitivity. This behavior is unique to Co. On the other hand, when the thickness of MgO is increased, the dipolar contribution for V is reduced, while the spin moment and Fermi contact contribution both increase. This trend suggests that V becomes closer to the free-atom limit.

When the adatoms are placed in the bridge position instead of the oxygen-top position, their magnetic properties change significantly. As shown in Figure 4.5d, the spin moments for Cr to Cu align with the free-atom values for one and two layers of MgO, while those for Sc to V exhibit a more erratic dependence on the number

of MgO layers. Specifically, Sc almost loses its magnetic moment for two layers of MgO, while Ti maintains a robust moment of $2\mu_{\rm B}$ (lower than the free-atom value of $3.28\mu_{\rm B}$). Furthermore, a low- to high-spin transition for V also occurs under these conditions. The situation is more complex than it appears at first glance.

The trends depicted in Fig.4.5e demonstrate that, despite having spin moments that match the free-atom values, the Fermi contact contribution is generally weaker than in the case of free atoms. Ti and Ni exemplify this, as the Fermi contact contribution may be sensitive to internal rearrangements of the electronic configuration of the adatom. Both elements display significant changes in the value of the Fermi contact when transitioning from one to two MgO layers, even though the total spin moment remains unchanged. These changes suggest modifications in the relative contributions to the total spin moment from the s (S-spin moment) and d electrons due to alterations in the buckling of the surrounding Mg and O atoms when the number of layers is increased (refer to Fig.A.1 of Appendix). It is worth noting that the Fermi contact contribution for Ni is now positive.

The dipolar contribution interpretation becomes more challenging for the adatoms on the bridge position, see Fig. 4.5f. The main reason is that the local symmetry is now C_{2v} (instead of C_{4v} for the oxygen-top position), so the dipolar tensor has two independent parameters instead of one, making it more challenging to interpret. We established the orientation of the axes in Fig. 4.1b, such that the z axis is perpendicular to the MgO plane, and the b_{zz} dipolar parameter corresponds to it. Additionally, we defined the x axis as pointing towards the nearest oxygen, with the dipolar parameter bxx. The trends observed in the b_{zz} parameter are qualitatively similar to the previous case(adatoms on the oxygen-top position) but with an overall reduced magnitude, and no substantial dependence on the MgO thickness is observed. A possible explanation for the reduced magnitude is that the adatom now forms bonds with two oxygen atoms instead of one, resulting in longer bond lengths (refer to Fig. A.1 of Appendix). This leads to a weaker deformation of the spin density.

However, Ti behaves differently from other elements, as the dipolar interaction depends on the number of layers. Therefore, similar to the changes observed in the Fermi contact contribution, the rearrangement of the s and d densities should also reflect a change in its shape, which is detected through the b_{zz} parameter. The biaxial character of the deformation of the spin density can be understood by comparing b_{zz} with b_{xx} (the other parameter is $b_{yy} = -b_{xx} - b_{zz}$). Choosing Co as an extreme example, $b_{xx} \approx -2b_{zz}$ which implies $b_{yy} \approx b_{zz}$, so there is only one primary deformation axis of the spin density towards oxygen. We thus see that a careful study of the dipolar parameters can provide a lot of information about the spatial distribution of the spin density. The dipolar contribution for the Ti adatom located on the oxygen-top position shows a large disagreement between our computed values and the experimentally measured ones. We attribute this difference to the experimental Ti adatom's hydrogenated state, which we did not consider in our calculations, as

reported by [42]. It is worth mentioning that the Ti-H system has been studied in detail in recent works [44], [45], [48], [49].

4.5. Adatoms on 1–2 layers of NaCl and NaF

In order to obtain further understanding regarding the magnetic properties of the 3d adatoms on ultrathin insulators, we now place them on a single or double layer of NaF and NaCl, which possess the identical rocksalt structure as MgO but with a larger energy gap.

Considering that the structure is the same, it is reasonable to anticipate that the relaxed geometries in the presence of adatoms would be comparable to those observed in the case of MgO. From an energy perspective, the anion-top position remains the most favorable, as illustrated in Fig. 4.3 b and c, with the main exceptions being Sc and Ti for a single layer of NaF and NaCl. It is worth noting that the stability of the anion-top position compared to the bridge position decreases as we move from NaF to NaCl. Therefore, we consider both adsorption positions for our analysis, similar to our approach with MgO. However, we note that the adatoms could also become substitutional dopants instead [29], [163], as reported in previous studies [29], [163].

The arrangement of adatoms on the fluorine-top position of NaF exhibits structural trends that closely resemble those observed for the oxygen-top position on MgO. Although the range of variation in the angle between F and the neighboring Na is slightly larger for NaF than for MgO, the distances between the adatoms and F are similar to those found for MgO. The only exception is Cr, located approximately 0.4 Å farther away than the other cases. Conversely, the positioning of adatoms on the chlorine-top position of NaCl is highly sensitive to the number of NaCl layers. For two layers of NaCl, the angle between Cl and the neighboring Na deviates only slightly from the ideal value of 180°, whereas for a single layer, the deformation is much stronger (up to 25° for Fe-Cu) and less regular. Generally, the distances between the adatoms and Cl are also greater than those observed for MgO or NaF (see Fig. 4.7).

The geometry of the adatoms on the bridge position is also similar to their corresponding ones on MgO (see Fig. A.2 and Fig. A.3 of Appendix). The buckling observed is more regular, with the distances between the adatoms and either Na or the respective anions being closer to each other than those found for MgO. On average, the distances are greater for NaCl than for NaF, which is expected. However, Cr is once again an outlier with much larger distances to the neighboring atoms than the other adatoms, resulting in the smallest induced buckling of the under-layer. A similar pattern is observed for Mn on two layers of NaCl. Apart from these exceptions, the angles between each adatom and the neighboring atoms fall within the range of 80° to 100°.

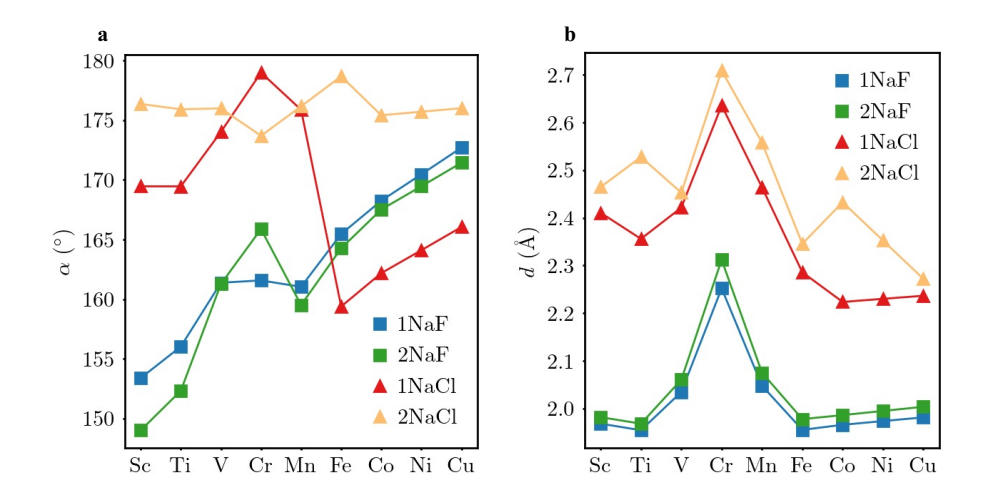


Figure 4.7.: Relaxed geometrical properties of adatoms on NaF and NaCl ultra-thin films, placed on top of the respective anion. (a) Na–F–Na or Na–Cl–Na bond angle and (b) distance between the adatom and either F or Cl. The number to the left of the chemical formula in the legend indicates the number of layers.

Fig. 4.8 displays the magnetic properties of adatoms situated on the anion-top and bridge positions. The number of NaF and NaCl layers has little influence on the overall magnetic properties, except for Ti, V, and Ni. The magnetic properties of adatoms on both positions strongly resemble the magnetic behavior of adatoms on the bridge position of MgO. With the exceptions mentioned earlier, the spin moments generally adopt the values of free atoms, and the hyperfine interaction contributions follow trends similar to previous cases, as can be identified in Figure 4.11.

Let us turn our attention to particular examples. Ti on NaF exhibits a low spin corresponding to a valence of $4s^23d^2$. However, the dipolar contribution reveals that a reshaping of its spin density occurs when moving from one to two layers, but only for the F-top position. The behavior of Ti on NaCl and of V and Ni on both substrates can be rationalized with the transition between low-spin and high-spin. When examining only the spin moment, nothing noteworthy appears for Fe, Co, and Cu.

However, the Fermi contact contribution indicates the impact of the changes in the local geometry, mostly for the bridge position. The dipolar contribution also follows these changes. Although Fe shows similar values of the dipolar parameters for both top and bridge positions, Co and Cu have noticeable differences. The dipolar parameters for Co shift from being large and positive on the top position to small and negative on the bridge position. For Cu, the behavior of the dipolar parameters

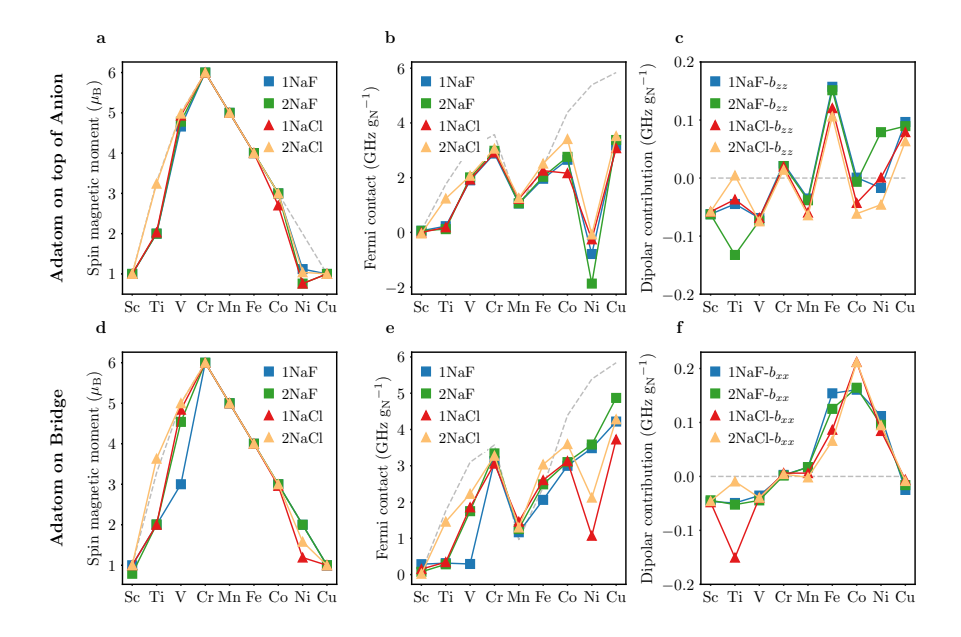


Figure 4.8.: Magnetic properties of adatoms on NaF and NaCl ultra-thin films, placed on top of anion (a–c) and on the bridge position (d–f). (a,d) Spin magnetic moment, (b,e) Fermi contact and (c,f) dipolar contributions to the hyperfine interaction. The number to the left of NaF and NaCl in the legend indicates the number of layers in the ultra-thin film. The gray dash line represent the free-atom results.

combined with the values of the Fermi contact contribution suggest that the spin density becomes more s-like on the bridge position, given the increase in magnitude for the Fermi contact and the drop to near zero in the dipolar parameters.

4.6. Adatoms on 1 layer of Cu2N and h-BN

To gain further insight into the hyperfine interactions on films which are not characterized by a rocksalt structure, we explore the case of single layers of $\mathrm{Cu_2N}$ and h–BN, which are commonly used experimentally to explore the electronic and magnetic properties of various nanostructures. Unlike the more ionic rocksalt compounds, these materials have a more covalent bond, leading to several differences. In both cases, we only consider the nitrogen-top position and note that N is less electronegative than O and F but similar to Cl. Previous experimental studies have investigated some of these adatoms [22]–[28], [30]–[32], but their hyperfine interactions have not been addressed.

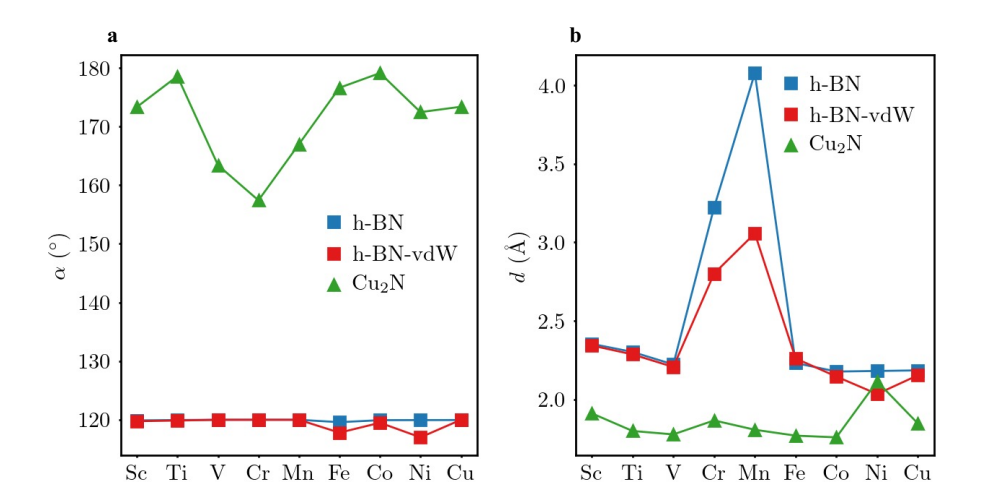


Figure 4.9.: Relaxed geometrical properties of top-stacked adatoms on Cu₂N, h–BN and h–BN-vdW. (a) B–N–B and Cu–N–Cu bond angles and (b) Distance between the adatom and nitrogen.

The adatoms on the nitrogen-top position of Cu_2N have a structural trend as follows. The angle between N and the two diametrically opposite Cu is close to the ideal value of 180°, with V, Cr, and Mn exhibiting the largest deviations (~ 18°). Meanwhile, the distances between the adatoms and N are similar to those between the adatoms and the anion on MgO and NaF, as shown in Fig. 4.9.On the other hand, the adatoms on the nitrogen-top position of h–BN behave differently from those on Cu_2N . The angle between N and B is very close to the clean value, and the bonding distances between the adatoms and nitrogen are larger than those on Cu_2N and similar to those on the top position for NaCl. These distances are actually so large for the Cr and Mn adatoms that they point to a failure of the PBE exchange-correlation functional in binding these adatoms to the film. This could be remedied to some extent by obtaining the relaxed geometry with an explicit account of van der Waals interactions (Fig. 4.9).

Figure 4.10 shows the magnetic properties of adatoms located at the nitrogen-top position of h–BN and $\mathrm{Cu_2N}$. Regarding h–BN, most of the adatoms exhibit magnetic properties minimally affected by the vdW correction. Although it seems that the spin moments of the adatoms are equivalent to those of free atoms (excluding Ni), a more detailed examination shows that Sc and Ti possess even higher spin moments than they would as free atoms (see Fig.4.10a). This is because of their unusual electronic configuration, $[\mathrm{Ar}]4s^13d^{n+1}$, that arises from the s-down energy level rising above the

d-up energy levels, a behavior already found in a previous theoretical study [164]. This explains the overall large values for the Fermi contact and the weak ones for the dipolar contributions to the hyperfine interaction (see Fig.4.10b,c). The negative values of the Fermi contact parameters for Ni were also found for the top positions of the previously discussed layers (clearly seen in Fig. 4.11a). The increased values of the dipolar parameters for Mn, Fe and Co when the van der Waals correction is included can be explained by the shortening of the adatom-nitrogen distances. Our findings are in broad agreement with those of Ref. [164], which also considered the impact of corrugation and a metal substrate.

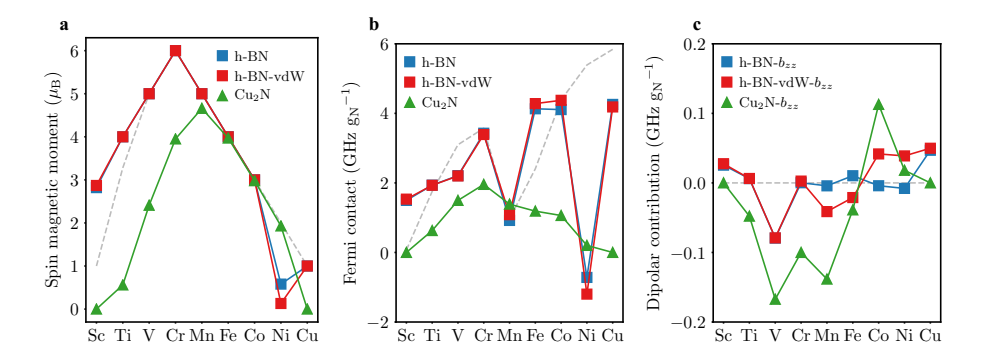


Figure 4.10.: Magnetic properties of top-stacked adatoms on $\mathrm{Cu_2N}$ and h–BN. (a) Spin magnetic moment, (b) Fermi contact and (c) dipolar contributions to the hyperfine interaction. The gray dash line represent the free-atom results.

Lastly, we discuss the magnetic properties for the $\mathrm{Cu_2N}$ case. The spin moment vanishes for Sc and Cu, weakens for Ti, and strengthens for Ni, being overall far from the free atom limit. Computationally, $\mathrm{Cu_2N}$ has a significantly smaller band gap than the previously studied systems, causing the magnetically active orbitals of the adatoms to hybridize with the conduction and/or valence states of the layer instead of being isolated in a large energy gap. As a result, the contribution to the spin moment from the s-orbitals is weak, resulting in the lowest values found for the Fermi contact parameters. Consequently, the contribution to the spin moment from the s-orbitals is weak, resulting in the lowest values found for the Fermi contact parameters. The large value of the dipolar parameters for V, Cr, Mn, and Co (see Fig.4.10c) can also be assigned to the stronger interaction with the electronic states of the layer.

4.7. Discussion of the limitations of our simulations

To the best of our knowledge, at the time of writing this thesis, the hyperfine interactions have only been measured for Ti, Fe, and Cu adatoms on two layers of MgO deposited on Ag(100) surface. The results of our simulations were in good agreement with the experimental data. However, we noticed a slight overestimation of the Fermi contact term for both Fe and Cu adatoms (about 20% larger). Although, we are dealing with rather small quantities, it is in order to inspect the limitations of our simulations induced our approximations. We do not incorporate the impact of the metallic substrate on which the insulating layers are deposited. We expect the most important effect to be the potential change in the charge state of the adatom by electron transfer from the metallic substrate [165], [166]. This situation happens when the adatom is highly electronegative, which is the case for a Au adatom on MgO deposited on Mo(100) surface. However, this is not the case for the transition metal atoms we studied, as computational studies have already verified it for Co adatoms [167].

The alignment of the s and d states is crucial in determining the final magnitude of the hyperfine interaction. Based on previous studies on transition metal complexes [150], [168] and our computations of small changes to the bond length, lattice constant, and the inclusion of a Hubbard-U correction for an Fe adatom on the oxygen-top position of two layers of MgO (as shown in Fig. A.4 - A.7 of Appendix), we estimate that the maximum uncertainty in the computed hyperfine parameters should be in the 10-15 % range. On the structural level, van der Waals interactions can lead to strong modifications in a few cases, as we already verified for the case of h–BN. A potential issue in a DFT setting is spin contamination, which is challenging to avoid, as mentioned in [150]. A way of curing it could be achieved by the Hubbard-U correction or by considering hybrid functionals or other nonlocal exchange-correlation corrections.

4.8. Conclusion

The hyperfine interactions are experimentally measurable quantities, but only a limited number of measurements are available for 3d adatoms on MgO. Therefore, to obtain systematic physical insights and provide guidance and reference values for future experiments, we conducted in this chapter a comprehensive and systematic study using ab initio calculations to investigate the hyperfine interactions of 3d magnetic adatoms on various ultra-thin insulating layers, including MgO, NaF, NaCl, h–BN, and Cu₂N, with varying thicknesses. We also examined the electronic and structural properties as well as the spin magnetic moments of these systems to provide insights into the hyperfine interactions. The free-atom calculations provide a clear picture for the origin of the hyperfine interaction and serves as a useful reference against which we could compare and contrast the behavior of the same atoms on different films. Our

study highlights the importance of considering the strength of the interaction between the adatom and the thin film as well as the local atomic arrangement in understanding the hyperfine interactions. Moreover, the hyperfine interactions can provide unique information on the electronic structure and magnetism of these adatoms, which cannot be obtained experimentally by other methods.

Before summarizing our findings on the hyperfine interaction, we recap the overall structural and magnetic properties on the different insulating films. Our results show that the adsorption on the anion-top position generally is the most energetically favorable compared to the bridge position. The structural trends for the adatoms on NaF are very similar to those on MgO, while on NaCl, there is a stronger dependence on the number of layers. On the anion-top position, the distance between the adatoms and Cl is significantly larger than for the cases of O and F. In addition, the buckling of the atoms surrounding the adatom on the bridge position of NaF and NaCl is somewhat more regular than that on MgO. Single layers of Cu₂N and h–BN are more covalently-bonded materials, while the rocksalt compounds (MgO, NaF, NaCl) are more ionic, which leads to several differences. The adatom-anion distances on Cu₂N (h–BN) are similar to those on MgO and NaF (NaCL).

The behavior of the spin magnetic moments can be understood as switching between the Hund's first rule for the d electrons (maximizing the number of d-up minus number of d-down electrons) and fully polarizing the s electrons (which is seen for V and Cr in most cases). This is explained by changes in the energetic alignment between the s and d levels, and can lead to transitions between two total spin values when changing the number of layers of the film.

The dominant contribution to the hyperfine interaction, known as Fermi contact, is determined by the spin density at the nuclear position. As this arises solely from the s electrons, it allows us to separate the total spin moment into s and d contributions, and to follow the relative energies of the s and d levels. The second contribution to the hyperfine interaction is called dipolar, representing the dipole-dipole interaction between the electronic and nuclear spins. This is only present if the electronic spin density is nonspherical, and so is absent for the free atoms. A summary of our findings is given in Fig. 4.11 for both contributions in all calculated substrates, which offers a bird's eye view of the hyperfine interactions.

The obtained map demonstrates the ability to modify the hyperfine interaction by atomic control of the location of the adatoms on the substrate. For all thin films except h-BN the magnitude of the Fermi contact parameter is significantly reduced compared to the free-atom case (Fig. 4.11a), which could indicate either a decrease in spin polarization of the s electrons or a decrease in their spatial localization near the nucleus of the adatom, due to bond formation with the atoms in the film. Overall, the larger the Fermi contact parameter is, the closer the adatom is to the free-atom limit. Moreover, the Fermi contact parameter can also trace internal rearrangements

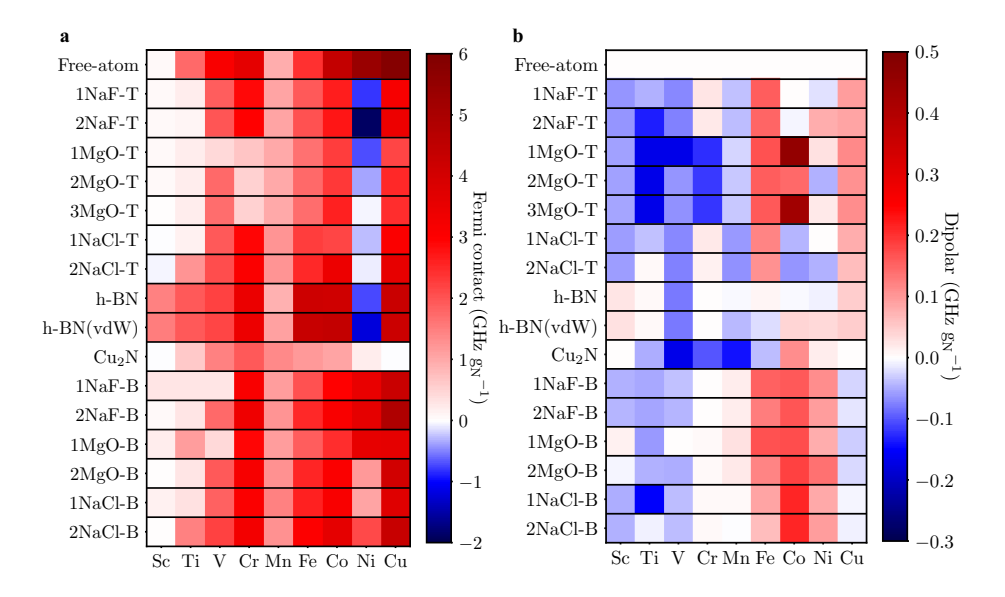


Figure 4.11.: Hyperfine interactions of magnetic adatoms on ultrathin films. (a) Fermi contact and (b) dipolar contributions. The free-atom values are given for comparison. The number to the left in the legend indicates the number of layers in the film. The adsorption position is denoted with T for atop the anion and with B for the bridge position (for h–BN and Cu₂N only T was considered). The possible impact of corrections from van der Waals interactions was explored for the h–BN case.

of the electronic structure that do not alter the total spin, as found for Ti and Ni on the bridge position of MgO. Generally, the bridge site leads to larger values of the Fermi contact contribution (Fig. 4.11a), in contrast to the dipolar contribution, compared to the anion-top site of the films with rocksalt structure (MgO, NaCl, NaF). In fact, it is somewhat stronger on NaF and NaCl than on MgO, which is due to the larger distance between the adatoms and the anion. Cu adatom, deposited on all ultra-thin insulating layers, has large values of the Fermi contact contribution compared to the rest of the 3d adatoms, especially in the bridge position, suggesting that the spin density becomes more s-like. It is worth noting that Ni adatom on the anion-top site has a negative Fermi contact contribution, while it is positive for the bridge site. This indicates that s-d coupling is antiparallel on anion-top position by contrast to the bridge site. Among all investigated films, h-BN, triggers the largest Fermi contact values (for Cu, Fe and Co adatoms) due to the adatom-substrate large distances, which makes it a strong candidate for future experiments. Cu₂N exhibits the weakest Fermi contact values due to its small band gap, enforcing a negligible contribution to the spin moment from the s-orbitals as a result of the hybridization of the magnetically active orbitals of the adatoms with the conduction and/or valence states of the substrate, instead of lying in a large energy gap as was the case for all other systems (MgO, NaF, NaCl, and h–BN).

The dipolar contribution to the hyperfine interaction is mostly sensitive to the spin density arising from the d electrons, and how it is deformed by interaction with the substrate. Its magnitude quantifies the non-sphericity of the spin density and is related to changes in the local bonding geometry. The dipolar parameters b_{zz} in the top position and b_{xx} in the bridge position are related to the interaction between the adatom and the anions. The sign of the dipolar contribution changes when the d-shell becomes more than half-filled, see Fig. 4.11b. The largest value was found for Co on one and three MgO layers. In general, Cr and Mn carry the weakest dipolar contributions on the bridge positions of the films with rocksalt structure, which indicates an almost spherical spin density.

In summary, this study presents the first comprehensive analysis of the hyperfine interaction strength of 3d transition metals adsorbed on various thin insulating layers using ab initio methods. The study of these systems is pertinent to the emerging field of the quantum control of surface spins and the broader quantum computing community. Our systematic analysis serves as a valuable guide for predicting the properties of unexplored systems and identifying the key engineering requirements necessary for achieving desired hyperfine characteristics. We anticipate numerous future exciting experimental and theoretical advancements in this field, which will benefit from the insights provided by our work.

In the next chapter, we explore the case of dimers by investigating the correlation between the hyperfine interaction and the magnetic state of free-standing Fe dimers, single Fe adatoms, and dimers deposited on a bilayer of MgO(001).

5. Hyperfine fields of Iron dimers

In the previous chapter, we systematically quantified from first-principles the hyperfine interactions for the whole series of 3d transition adatoms (Sc-Cu) deposited on various ultra-thin insulators, establishing the trends of the computed hyperfine interactions with respect to the filling of the magnetic s- and d-orbitals of the adatoms and to the bonding with the substrate. Here we explore the case of dimers by investigating the correlation between the hyperfine interaction and the magnetic state of Fe dimers, free standing and deposited on a bilayer of MgO(001), which are compared to the case of Fe single adatoms investigated in the previous chapter. Fe-adatom is a prototypical adatom that carries a large hyperfine interaction with a minimal nuclear spin, which offers several advantages over the rest of potential 3d transition metal atoms.

We find that the magnitude of the hyperfine interaction can be controlled by switching the magnetic state of the dimers. For short Fe-Fe distances, the antiferromagnetic state enhances the hyperfine interaction with respect to that of the ferromagnetic state. By increasing the distance between the magnetic atoms, a transition towards the opposite behavior is observed. Furthermore, we demonstrate the ability to substantially modify the hyperfine interaction by atomic control of the location of the adatoms on the substrate. Our results establish the limits of applicability of the usual hyperfine hamiltonian and therefore we propose an extension based on multiple scattering theory.

Results presented in this chapter have already been published in [169]: Shehada et al., J. Phys.: Condens. Matter. 34, 385802 (2022).

5.1. Introduction

Following the study performed in the previous chapter, it becomes appealing to explore the hyperfine interactions of more complex nanostructures made of 3d adatoms. We are intrigued by the possibility of engineering that interaction by building up various multi-atomic objects and investigate the possibilities offered by complex alignments of the magnetic moments and their impact to the underlying coupling to nuclei spin. Certainly, this kind of investigations are crucial for the guidance for exploratory EPR/ESR STM experiments aiming at building atomic qubits on surfaces. Moreover, wonderful insight can be grasped once accessing the intricate interplay between

hyperfine interaction and the various electronic, magnetic and chemical properties of complex nanostructures, as explored with nuclear magnetic resonance techniques [62].

After our extensive systematic study presented in the previous chapter, here we investigate Fe nanostructures. Noting that Ti dimers were investigated experimentally [42], our choice on Fe-based nano-objects is motivated by: (i) the Fe adatoms being characterized by a larger hyperfine interaction than Ti adatoms [42], [151]; (ii) in the experimentally measured Ti dimer, only one of the adatoms carries a nuclear spin [42]; (iii) identification of dimer-induced multiple ESR peaks should be easier in Fe than Ti since the former carries a nuclear spin of $\frac{1}{2}$ instead of the larger nuclear spin expected for Ti $(\frac{5}{2}$ or $\frac{7}{2})$ [170]. We investigate the impact of the magnetic alignment of the spin moments as function of their distance and bonding site on the strength of the hyperfine interaction.

5.2. Computational details

We follow the same numerical procedure detailed in chapter 4, utilizing DFT as implemented in the Quantum ESPRESSO code, on the basis of PBE-PAW scalar-relativistic pseudopotentials and GIPAW module with Gaussian smearing of width $0.01\,\mathrm{Ry}$ to compute the structural, electronic, and magnetic properties and hyperfine parameters without including the spin-orbit coupling. For completeness, we highlight that we maintained the kinetic energy cutoff for the wavefunctions and charge density to the standards specified in the previous chapter while the impact of the Hubbard-U correction on the hyperfine parameters was investigated with the simplified rotationally-invariant scheme.

We performed two types of simulations: The Fe dimers can be either free-standing or deposited on MgO. For the case of free-standing dimers, we employed cubic periodic cells with a lattice constant of 20 Å, in order to minimize interactions between periodic replicas of the dimers, and Γ -point sampling of the Brillouin zone. The noncollinear magnetism of these dimers was studied by the constrained DFT approach explained in Ref. [171], using (PBE) scalar-relativistic ultrasoft pseudopotentials [127] also from the PSLibrary and a fixed bond length of 2 Å. In order to ensure that the different noncollinear states were comparable, for each fixed magnetic configuration we performed a sequence of self-consistent constrained calculations ramping up the penalty parameter with the values $\lambda \in \{0.1, 0.2, 0.5, 2, 5, 10, 20, 25, 30\}$ (Ry). We show in Fig. B.1 of Appendix that this ramping-up strategy indeed achieved good convergence of the various quantities of interest. We remark that since GIPAW does not currently support non-collinear calculations, we used the projwfc.x code to obtain atom- and orbital-resolved spin magnetic moments for further analysis and connection to the hyperfine interactions.

We utilize the same supercell introduced in the previous chapter for the case of

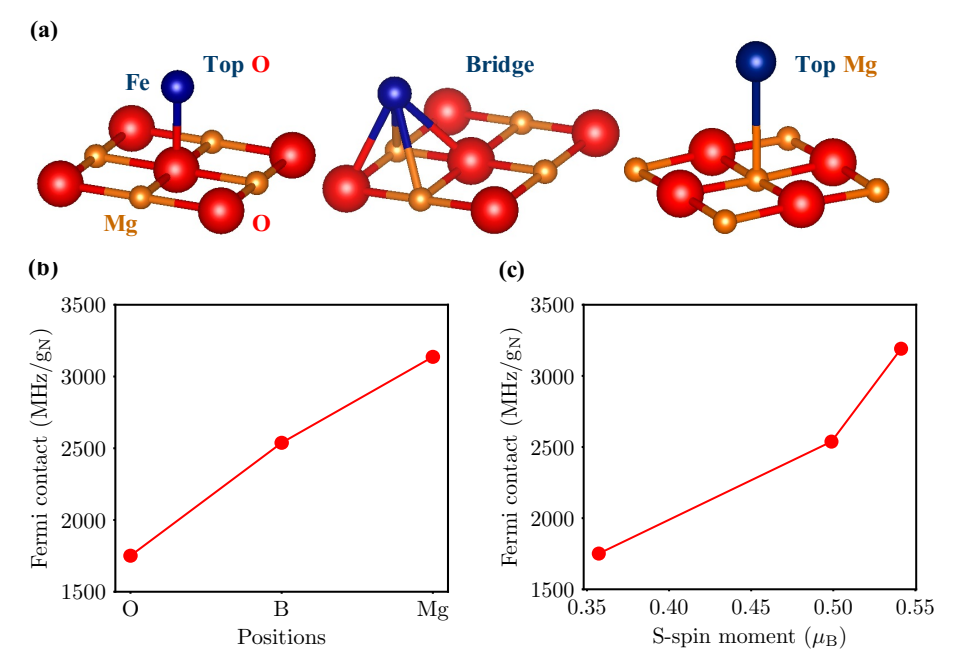


Figure 5.1.: Fe adatoms on a bilayer of MgO. (a) Geometry of Fe adatoms on a bilayer of MgO. The second MgO layer is not shown. The Fe adatom is stacked on top of O, on the bridge position and on top of Mg, respectively. Fe is represented by a blue sphere, O by a red sphere and Mg by an orange sphere. (b) Fermi contact contribution to the hyperfine interaction for the considered positions and (c) Fermi contact contribution as a function of the contribution to the spin magnetic moment coming from the s electrons (S-spin moment).

MgO substrate. Here we focus on a bilayer of MgO with the lattice constant reported in Table 4.1. We utilize the results of the simulations on the Fe adatom, as obtained from the previous chapter, as a reference for our calculations pertaining to the Fe dimers. However, for the latter case, we consider the top of magnesium as a potential location for the Fe atoms (Fig. 5.1a), which is a scenario not addressed in chapter 4. For the Fe dimers deposited on the MgO. bilayer, we set the Fe adatoms on different structures as shown in (Fig. 5.2). The supercells contain 73 and 74 atoms in total for the case of Fe adatoms and Fe dimers on bilayer of MgO, respectively, and a vacuum thickness equivalent to 9 layers of MgO. We adopted a $4 \times 4 \times 1$ k-mesh in both cases (Fe adatom and Fe dimer on bilayer of MgO). The cell dimensions were kept fixed while all atomic positions were allowed to fully relax.

Finally, to ensure that we chose suitable cutoffs, we studied the effect of the kinetic

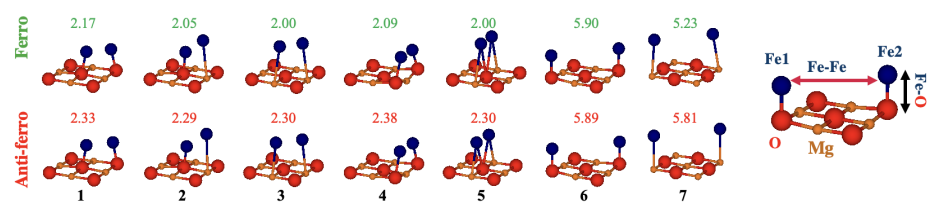


Figure 5.2.: Atomic structures for Fe dimers on a bilayer of MgO. The first row represents the Fe dimers in the ferromagnetic state and the second row those in the antiferromagnetic state. Fe atoms are represented by blue spheres, O by red spheres and Mg by orange spheres. The final diagram on the right defines the Fe-Fe distance, represented by the horizontal double arrow, and either the Fe-O or the Fe-Mg distance, whichever is nearest to the corresponding Fe atom, represented by the vertical double arrow. The green numbers on top of each structure in the first row give the Fe-Fe distance in the ferromagnetic state and the red ones in the second row in the antiferromagnetic state, in Å.

energy cutoff for the wavefunctions ('ecutwfc') and for the charge density ('ecutrho'), for fixed ecutrho = 8*ecutwfc, on the basic properties of ferromagnetic Fe dimers which are free-standing (Fig. B.2 of Appendix) and on MgO (Fig. B.3 of Appendix), for PAW and USPP. These tests confirm that the desired convergence of total energy, spin moment, and S-spin moment is achieved with the kinetic energy cutoff of 90 Ry for the wavefunctions (720 Ry for the density), which we used in the previous and current chapters.

In this chapter, we do not discuss the dipolar contribution to the hyperfine interaction since we found it to make a small contribution and be more weakly dependent on the magnetic state than the Fermi contact term, see Fig. B.4 of Appendix.

5.3. Free-standing Fe dimers

In order to set the stage for our study of the Fe dimers deposited on a MgO bilayer, we first explore the case of free-standing dimers so that the substrate and its influence is excluded. We investigate the dependence of the Fermi contact term as function of the distance between the adatoms and of their magnetic state being ferromagnetic or antiferromagnetic.

Our calculations indicate that free-standing dimers prefer to be ferromagnetic for all investigated Fe-Fe distances (up to $7\,\text{Å}$) as shown in Fig. 5.3a. The equilibrium distance of the ferromagnetic (antiferromagnetic) dimer is $2.0\,\text{Å}$ ($2.3\,\text{Å}$) in agreement with previous theoretical work, e.g. [171]. Interestingly, the dependence of the Fermi contact contribution to the hyperfine field displays a rich behavior as a function of

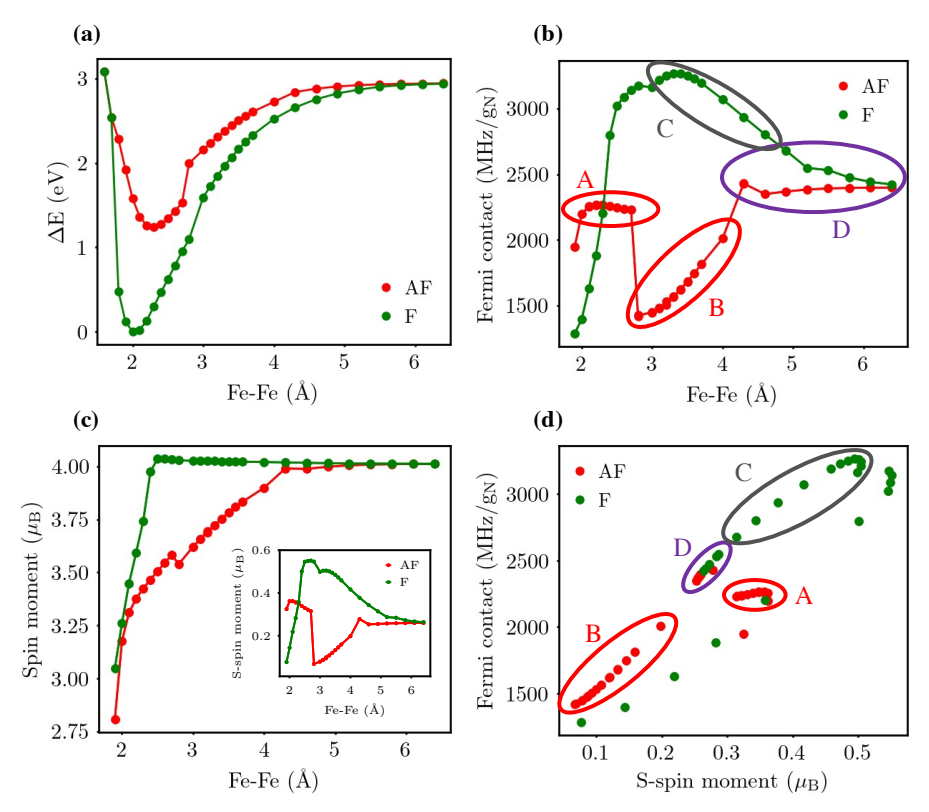


Figure 5.3.: Basic properties of free-standing Fe dimers. (a) Total energy difference with respect to 2 Å of Fe-Fe distance in the ferromagnetic state, which is the most stable distance, (b) Fermi contact contribution to the hyperfine interaction, (c) atomic spin moment with the inset displaying the S-spin moment as function of atomic distances, and (d) Fermi contact contribution as a function of S-spin moment.

the Fe-Fe distance, as seen in Fig. 5.3b. For short distances ($\lesssim 2.3\,\text{Å}$), the antiferromagnetic alignment of the spin moments induced a hyperfine field that is larger than the one obtained for a ferromagnetic state, and this behavior is reversed for larger distances. For distances ranging from 2.3 Å till 2.7 Å defines a plateau region for the Fermi contact term of the antiferromagnetic dimers before a sharp drop leading to a minimum, 1410 MHz, found at a distance 2.8 Å. In strong contrast and within the same range of Fe-Fe distances, the ferromagnetic dimer reaches the maximum value of the Fermi contact term 3280 MHz obtained at 3.3 Å, which the distance dependence being rather smooth. At distances larger than 6 Å the hyperfine field becomes independent of the magnetic state and approaches the value known for a

single free-standing Fe atom [151].

The distance-dependent behavior of the atomic spin moments for both magnetic states (Fig. 5.3c) is rather different from that of the Fermi contact term. The atomic spin moment increases monotonically with the distance and for a given distance is always larger for the ferromagnetic dimer. Its value saturates for the ferromagnetic dimer at a distance of 2.5 Å while for the antiferromagnetic one this only happens after 4.3 Å. While the magnitude of the atomic spin moment is mostly contributed by the d electrons, it is well known that the Fermi contact term is given by the spin density at the nuclear position (see Eq. 2.28). The latter correlates well with the contribution of the s electrons to the atomic spin moment, denoted S-spin moment, as shown in Fig. 5.3d and inset of Fig. 5.3c. The average trend is of proportionality between the two quantities, although the data does not fall on a single straight line and instead traces out two slightly curved lines. Both the S-spin moment and the Fermi contact term attain their largest values for the ferromagnetic dimers, but when the S-spin moment falls below $\lesssim 0.3\,\mu_{\rm B}$ the Fermi contact term becomes larger for the antiferromagnetic dimer than for the ferromagnetic one.

The non-trivial dependence of the hyperfine field on the magnetic state of the dimer, the distance between the atoms or the magnitude of the S-spin moment is a consequence of its sensitivity to changes in the electronic structure. These can be identified in Fig. 5.3b and Fig. 5.3d by discontinuities or kinks, as highlighted by the labelled ovals. In the large separation limit, the proportionality between the Fermi contact term and the S-spin moment is independent of the magnetic state, as seen in the oval labelled D in Fig. 5.3d, while the bonding is different for different magnetic states, which leads to a different localization of the s electrons and to the differences seen for a fixed separation between the Fe atoms in Fig. 5.3d.

The behavior for intermediate distances evolves in opposite ways for the ferromagnetic and antiferromagnetic states, see ovals labelled B and C in Fig. 5.3d, while connecting to the large distance data. This is explained by the increase (decrease) of the S-spin moment with decreasing separation for the ferromagnetic (antiferromagnetic) dimer. In the ferromagnetic case, the atomic spin moment is constant in region C (compare with Fig. 5.3c), so the increase in the S-spin moment with decreasing separation is compensated by a reduction in the spin moment of the d electrons. In the antiferromagnetic case, the atomic spin moment decreases in region B (compare with Fig. 5.3c) by more than the decrease in the S-spin moment with decreasing separation, which also signals a reduction in the spin moment of the d electrons. The decrease in the separation between the Fe atoms leads to an increased delocalization of the d electrons, which weakens the local intra-atomic exchange interaction among them and so their spin polarization. At any distance, the s electrons are much more delocalized than the d electrons and so experience the combined influence of the d spin moment of both Fe atoms. With decreasing separation, the ferromagnetic alignment leads to a stronger net exchange field and so to the observed increase in the S-spin moment, while the antiferromagnetic alignment leads to a partial cancellation of the net exchange field and so the the reduction in the value of the S-spin moment.

The most striking changes happen at short separations. In the antiferromagnetic state, the Fermi contact term jumps to a much larger value than at intermediate separations, see oval labelled A in Fig. 5.3b, which clearly follows from the associated jump in the magnitude of the S-spin moment, as shown in Fig. 5.3d, from $\lesssim 0.1 \,\mu_{\rm B}$ to $\gtrsim 0.3 \,\mu_{\rm B}$, see oval labelled A in Fig. 5.3d. There is also an accompanying but smaller jump in the atomic spin moment (at 2.7 Å in Fig. 5.3c), but overall the polarization of the d electrons is still decreasing with decreasing distance. At the same time, the magnitude of the Fermi contact term shows a plateau behavior with respect to the value of the S-spin moment (or separation between the Fe atoms). The magnitude of the S-spin moment is actually increasing with decreasing separation, so the plateau implies that the spin polarization at the nuclear position remains essentially constant. In the ferromagnetic state, the S-spin moment follows the steep reduction of the atomic spin moment with decreasing, with the same behavior thus seen on the magnitude of the Fermi contact term. However, an inspection of the data in Fig. 5.3d (points not encircled by a green oval) shows that the proportionality between the Fermi contact term and the S-spin moment is different at short separations than at large separations, with a smaller slope. This is explained by a decreased spatial localization of the s-electrons at the nuclear position for shorter separations, as they become more concentrated in the bonding region between the Fe atoms.

The strong impact of the magnetic state provides a route for engineering the magnitude of the hyperfine interaction while at the same time raising concerns on whether the hyperfine Hamiltonian of Eq. 2.27 is appropriate (for instance in combination with Heisenberg exchange interactions) to model and interpret experimental findings. One can use multiple scattering theory as a general framework to derive how the s-spin density at the nuclear position of atom i is expected to depend on the orientations of nearby magnetic moments, see Appendix D. If one neglects spin anisotropies, we anticipate that the lowest order dependence should be proportional to the dot products of the spin moments located at sites i and j, $\mathbf{S}_i \cdot \mathbf{S}_j$, similar to the Heisenberg exchange interaction. Our proposed extended Hamiltonian reads:

$$\hat{H} = \sum_{i} \mathbf{S}_{i} \cdot \left(\underline{\mathbf{A}}_{i}^{(0)} + \sum_{j} \underline{\mathbf{A}}_{ij}^{(1)} \mathbf{S}_{i} \cdot \mathbf{S}_{j} + \dots \right) \cdot \mathbf{I}_{i} + \sum_{ij} J_{ij} \mathbf{S}_{i} \cdot \mathbf{S}_{j} , \qquad (5.1)$$

where $\underline{A}_{i}^{(0)}$ is the part of the hyperfine interaction tensor which is independent of the magnetic state of the other atoms and $\underline{A}_{ij}^{(1)}$ is the proposed lowest order correction, and we include the standard Heisenberg exchange interaction J_{ij} . We can investigate the validity of the proposed Hamiltonian by employing the S-spin moment as a proxy for the behavior of the hyperfine interaction, as already demonstrated. We consider a free-standing Fe dimer at a fixed bond length of 2.0 Å and utilize constrained DFT to fix the spin direction of Fe₁ and rotate the one of Fe₂ (see Fig. 5.4a), which defines the angle θ between the two spin directions. The total energy has an essentially $\cos \theta$

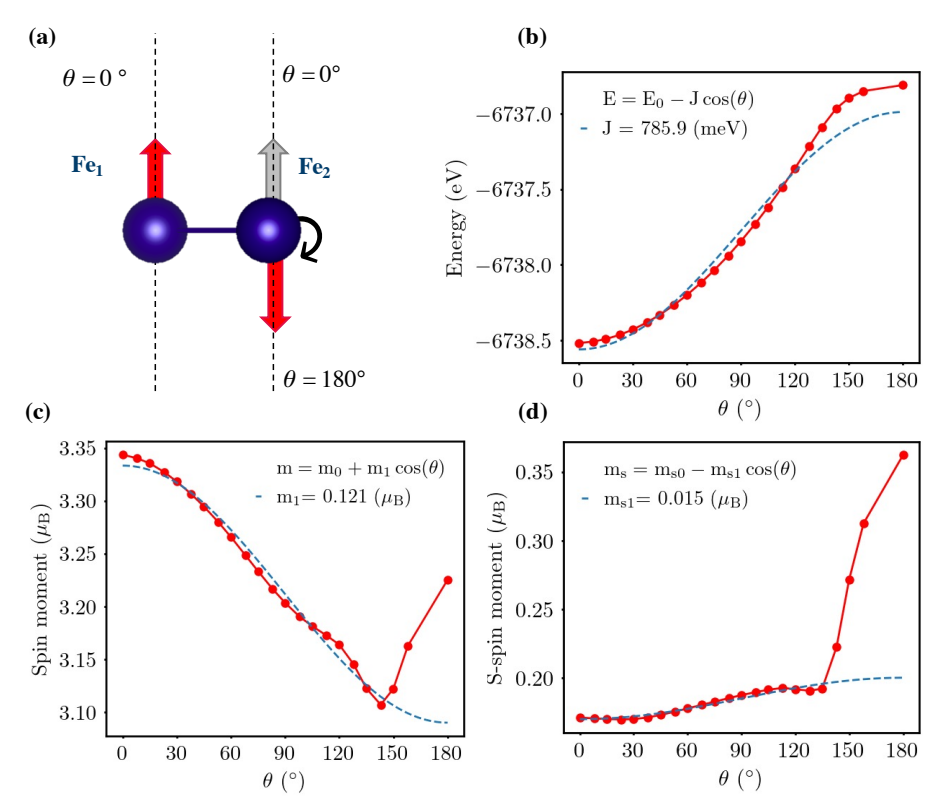


Figure 5.4.: Noncollinear magnetism of free-standing Fe dimers. (a) Schematic of the considered magnetic configurations. (b) Total energy, (c) atomic spin magnetic moment and (d) S-spin magnetic moment as a function of the angle (θ) between the directions of the spins of the Fe dimer.

dependence (Fig. 5.4b), which is the expected behavior according to the Heisenberg model.

That things are not so simple is demonstrated by the angular dependence of the atomic spin moment (Fig. 5.4c) and S-spin moment (Fig. 5.4d), with their magnitudes changing in a cosine-like manner until about 120° and then evolving in a more complex way near the antiferromagnetic alignment. This is likely due to a crossing of electronic energy levels as a function of the angle with changes in the highest occupied molecular orbital which leads to a more involved angular dependence of these key quantities. Nevertheless, the cosine-like angular dependence holds well in two separate angular ranges, from the ferromagnetic alignment up to 120° and from there until the antiferromagnetic alignment, although with different coefficients. This makes the proposed extended hyperfine Hamiltonian Eq. 5.1 useful for finite-temperature or non-equilibrium simulations of the ferromagnetic dimer, for instance in a pump-probe

scenario.

5.4. Recap: Hyperfine interaction of a single Fe adatom on bilayer of MgO

Let us first recapitulate the properties of a single Fe adatom discussed in the previous chapter and compare them to the scenario where Fe sits on top of magnesium before turning to the Fe dimers deposited on a bilayer of MgO. Naturally, if the atoms of the dimer are sufficiently far apart one recovers the properties of the isolated adatom. The three structural scenarios of interest are those realized experimentally [39], [40], [42], and consist as mentioned earlier on the Fe atom siting on top of oxygen or in the bridge position, as depicted in Fig. 5.1a. The Fe on top of oxygen is the energetically most favorable position but it creates the weakest hyperfine field (Fig. 5.1b), followed by the bridge position before reaching a maximum when adsorbed on top of magnesium are in good agreement with the trends of the S-spin magnetic moment shown in Fig. 5.1c. The origin of the unveiled trend lies in the local bonding geometry and is closely related to the bond length between the adatom and the nearest substrate atom, indicating qualitatively the strength of hybridization of their respective electronic states. Larger bond lengths lead to reduced hybridization, which in turn favors the localization of the spin density at the nucleus and so a larger hyperfine field. For instance, this bond length is the shortest atop oxygen (1.9 Å), then it increases in the bridge position (2.4 Å) before reaching its maximum value atop magnesium (2.9 Å).

5.5. Hyperfine interaction of Fe dimers on a bilayer of MgO

Here we address the last main topic of our investigation in the current chapter, namely dimers placed on MgO bilayer considering different location of the Fe atoms and inter-adatom distances and assuming both the ferromagnetic and antiferromagnetic states. After structural relaxation, we classified the results into seven structures which strongly depend on the magnetic alignment of the spins, as illustrated in Fig. 5.2. As shown in Fig. 5.5a and similarly to the free-standing case, the Fe dimers prefer to be in a ferromagnetic state, with structure 1 (see Fig. 5.2) being the most stable. We find that switching the atomic spin alignment from parallel to antiparallel increases the Fe-Fe distance, as illustrated in Fig. 5.5b, the exception being structure 6. In structures 1 to 5 the Fe adatoms are close to each other with a separation only slightly larger than that found for the free-standing dimers in the respective magnetic states, while in structures 6 and 7 they are much farther apart. The distances between each Fe atom and the nearest substrate atom are given in Fig. 5.5c and Fig. 5.5d. Short distances indicate that oxygen is underneath while long distances signal magnesium, with the values close to but in most cases substantially larger that those found for an

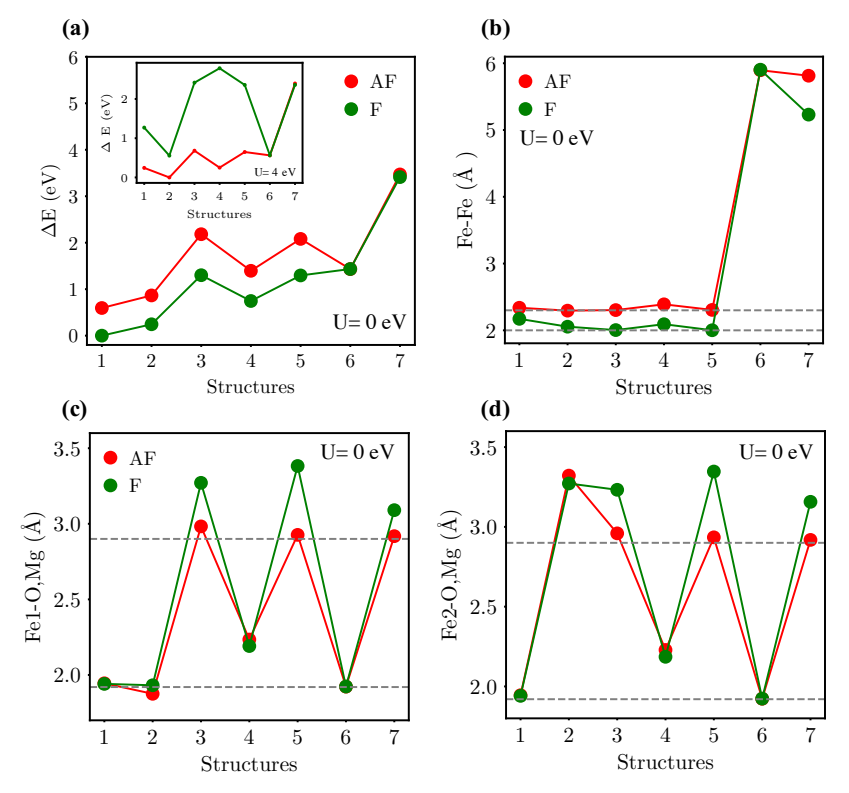


Figure 5.5.: Relaxed structural properties of Fe dimers on the MgO bilayer. (a) Total energy difference with respect to structure 1 in the ferromagnetic state, which is the most stable one, with the inset displaying total energy difference with respect to structure 2 in the antiferromagnetic state, which is the most stable one for Hubbard U=4 eV. (b) Fe-Fe distance, (c) distance between Fe1 and either O or Mg, whichever is nearest, and (d) likewise for Fe2.

isolated Fe adatom.

The variation of the hyperfine interaction across the different dimer structures in both considered magnetic states is plotted in Fig. 5.6a. Given the previous discussion, it makes sense to compare structures 1 to 5 to the results for the free-standing dimers and structures 6 and 7 to the results for the isolated adatoms on MgO. Starting with the latter two structures, we do find that the obtained values of the Fermi contact term are very similar to the adatom values and have little dependence on the magnetic state of the dimer, confirming the weak coupling between the Fe atoms (see also Fig. 5.5a). In contrast, structures 1 to 5 show a strong coupling between the two Fe

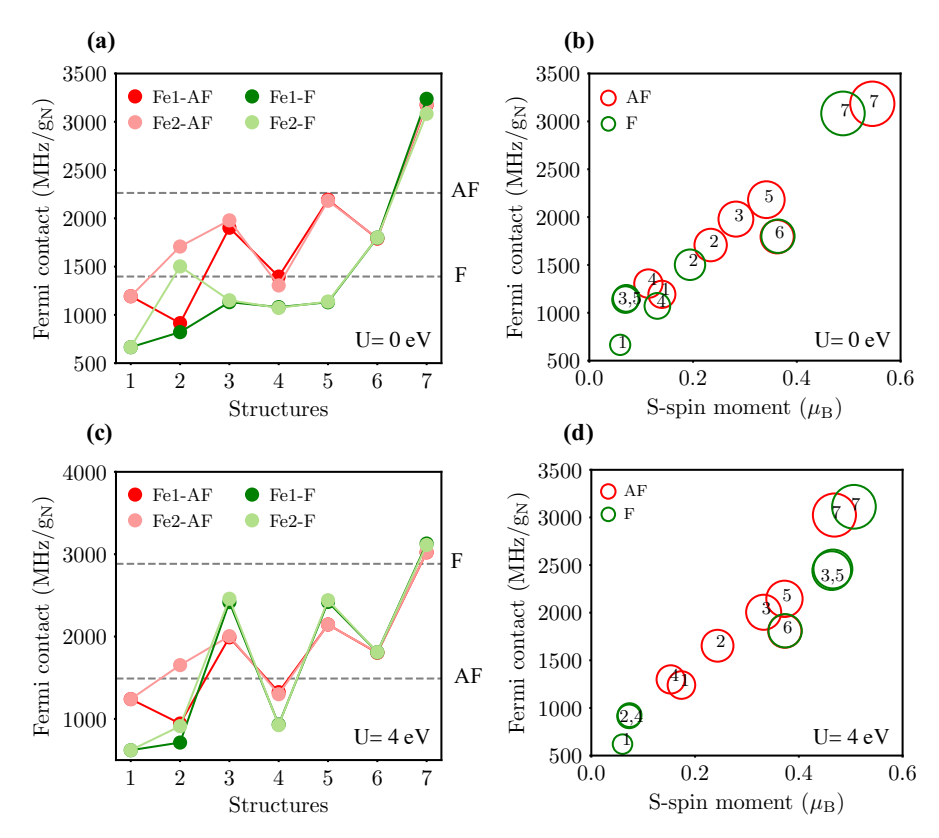


Figure 5.6.: Effect of the Hubbard-U on the hyperfine fields of Fe dimers on the MgO bilayer, for U=0 (a,b) and for U=4 eV (c,d). The Fermi contact contribution to the hyperfine interaction for the different structures and magnetic states is given in (a,c). The horizontal dashed lines in (a,c) indicate the values found for the free-standing dimer at their equilibrium bond length in the ferromagnetic (F) and antiferromagnetic (AF) states. The Fermi contact contribution as a function of the S-Spin magnetic moment is shown in (b,d). The number inside the circles identifies the Fe dimer structures.

atoms combined with a strong influence of the MgO bilayer on the hyperfine interactions. Overall the values of the Fermi contact term are substantially reduced from those obtained for the free-standing dimers in the respective magnetic states and at their equilibrium bond lengths. This is a consequence of the dimer bonding with the MgO bilayer, which leads to an increased delocalization of the s electrons and so to a reduction of the value of the Fermi contact term. In structures 1, 3, and 5, changing the dimer from ferromagnetic to antiferromagnetic leads to an almost doubling in the

magnitude of the Fermi contact term, while for structures 2 and 4 the change in the magnetic state has a much weaker impact on the hyperfine interaction. This cannot be simply rationalized in terms of strong vs. weak magnetic coupling between the Fe atoms in the dimer, as Fig. 5.5a shows that for all these structures there is a large total energy difference between the two magnetic states. Instead, it reveals in which structures the s electron orbitals change strongly or weakly in response to a change in the magnetic state of the dimer.

Fig. 5.6b shows that the proportionality between the Fermi contact values and the S-spin magnetic moment is fairly independent of the structure and magnetic state of the Fe dimer. In contrast to the results for the free-standing dimers, on MgO the data follows a single linear relation between the two quantities, which is even more apparent if structures 6 and 7 are ignored (as they are closer to the isolated adatom behavior). This can be interpreted as a stabilization of the electronic structure against magnetic or structural changes, in particular of the s-states, due to the bonding between the Fe atoms and the substrate.

We thus see that the S-spin magnetic moment is an excellent proxy for the hyperfine field of the Fe dimers on MgO, and so our findings concerning the noncollinear magnetic states of the free-standing dimers should also apply in this situation.

The strongly-localized magnetic d-orbitals of Fe are affected by self-interaction errors in the standard exchange-correlation functionals, so we consider the impact of an additional correction such as a Hubbard-U. In the previous chapter, we dealt with single Fe adatoms on a bilayer of MgO. We checked carefully the dependence of U and we concluded that the Hubbard-U correction has a small influence on the computed hyperfine parameters. In addition to that, our results agreed well with the experimental measurements [42] of the Fermi contact parameter without including the Hubbard-U correction.

We now revisit this issue for the Fe dimers on the bilayer of MgO. We repeated all the calculations by including $U \in \{0,1,2,3,4,5\}$ eV for all the structures (see Fig. 5.7 and Fig. B.5 - B.7 of Appendix), but keeping the geometries found at U=0. We found that the ground state changes from ferromagnetic to antiferromagnetic in structures 1 to 5 for $U \ge 2$ eV (Fig. 5.5a, inset). The Hubbard-U correction still has a small influence on the hyperfine parameters of Fe dimers on the bilayer of MgO in structures 1, 2, 4, 6 and 7, although the relative change is somewhat larger than found for the single Fe adatoms. As concrete examples, we present results for structures 1 and 2 in Fig. 5.7. While the antiferromagnetic state becomes the ground state once $U \ge 2$ eV, the Fermi contact parameter has the same qualitative behavior as for U=0, being much larger in the AFM than in the FM case. We found a similar behavior in structure 4 (see Fig. B.5 of Appendix)(not shown). The exception is the Fe atom atop Mg in structure 2, which shows a much stronger dependence on U.

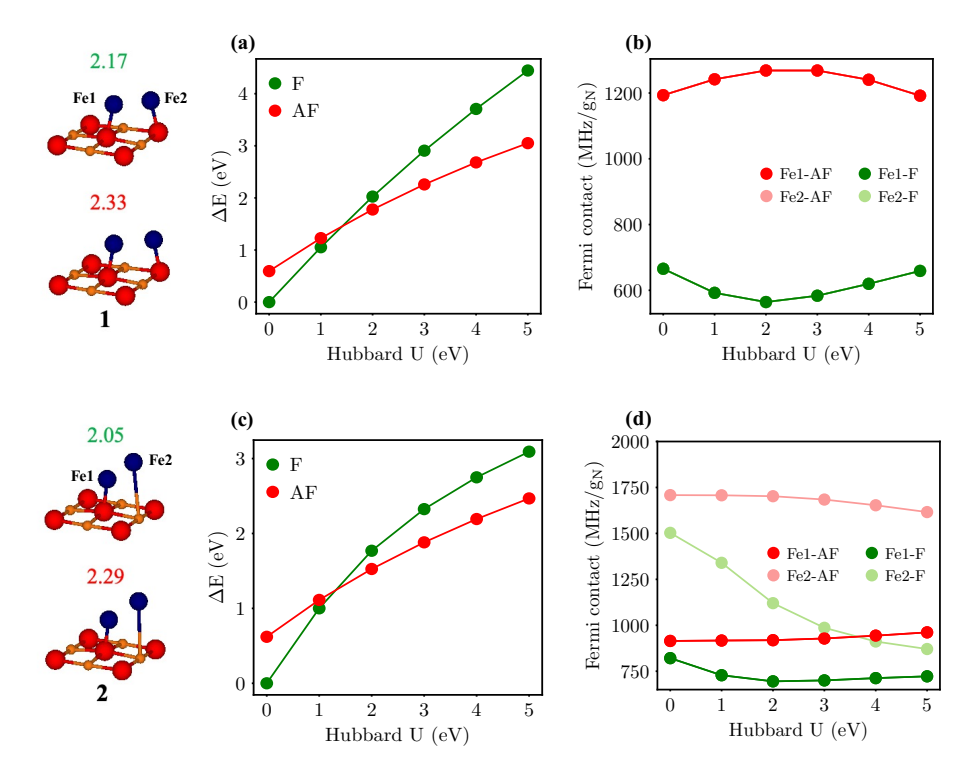


Figure 5.7.: Effect of the Hubbard-U on the hyperfine fields of Fe dimers on the bilayer of MgO in structure 1 (a and b) and structure 2 (c and d) in the ferromagnetic (F) and antiferromagnetic (AF) states. (a,c) Total energy difference with respect to U=0 eV in the ferromagnetic state. (b,d) Fermi contact contribution to the hyperfine interaction. Fe1 and Fe2 in structure 1 they are equivalent.

In order to illustrate the trends, we decided to include in Fig. 5.6(c,d) the results with U = 4 eV, which is a value close to what was used in a previous study [34]. We see that there is only a qualitative change in the results for structures 3 and 5, for which the Fermi contact parameter is now larger in the ferromagnetic state than in the antiferromagnetic one, and also for the Fe atom atop Mg in structure 2. This is due to transitions from high- to low-spin states when we switch the magnetic state from ferromagnetic to antiferromagnetic. Fig. 5.6a and d, shows that the proportionality between the Fermi contact values and the S-spin magnetic moment is very similar, independently of U. In general, the qualitative behavior is the same for the most structures, with some variation in the quantitative behavior when we include Hubbard-U corrections.

5.6. Conclusion

We presented the results of ab initio calculations on the main contribution to the hyperfine interaction, namely the Fermi contact, of free standing Fe dimers, Fe dimers deposited on a bilayer of MgO compared to the case of isolated Fe adatoms. We explored in particular their structural, electronic and magnetic properties and scrutinized the impact of the inter-adatom distance as well as the magnetic state on the hyperfine interaction, whose physics is mainly dictated by the polarization of the s electrons at the nucleus position.

We revealed the non-trivial influence of the magnetic alignment of the moments, being parallel or antiparallel, on the magnitude of the Fermi contact term. At short inter-adatom distances, the antiferromagnetic state enhances the hyperfine interaction with respect to that of the ferromagnetic state while the opposite behavior is found for large distances. Considering the preceding studies on transition metal complexes [150], [168] and the variation of our computed parameters when considering a Hubbard-U correction, we found that the qualitative behavior is the same for the most structures, with some variation in the quantitative behavior.

This opens on the one hand the possibility of controlling the magnitude of the Fermi contact term by switching the magnetic state of the nanostructure. This could potentially be achieved via for example: (i) atomic manipulation utilizing atomic decoration, by engineering the environment of the adatoms, (ii) inelastic scanning tunneling spectroscopy or (iii) an external magnetic field.

On the other hand, our findings question the use of the hyperfine Hamiltonian, eq. 2.27, usually amended with conventional Heisenberg exchange interaction to describe the interplay of magnetic coupling and hyperfine interaction, which is not anymore a constant, in multi-atomic structures. To address the latter aspect, we proposed an extended hyperfine-Heinseberg Hamiltonian, eq. 5.1, where the hyperfine interaction is proportional to the dot product of the spin moments, as motivated from multiple-scattering theory. Our calculations confirm that the angular dependence is reasonable for a wide range of angles around the value obtained for the ferromagnetic state.

Moreover, we evidenced the ability to substantially modify the Fermi contact term by atomic control through the control of the location of the adatoms on the substrate. The nature of the nearest neighboring surface atoms impact on the adatom-substrate distance, which affects the localization of the spin-polarized s electrons and therefore the hyperfine interaction.

6. Magnetic Anisotropy Energy of 3d adatoms and 3d–O molecules on the bilayer of MgO

Designing systems with large magnetic anisotropy energy (MAE) is desirable and critical for nanoscale magnetic devices. Thus far, the MAE per atom in single-molecule magnets and ferromagnetic films remains typically one to two orders of magnitude below the theoretical limit imposed by the atomic spin-orbit interaction. Experimentally Rau et al. [8] realized the maximum MAE for a 3d transition metal atom by coordinating a single Co atom to the O site of a MgO(100) surface.

Theoretically, conventional density functional theory (DFT) calculations do not recover the large MAE of this system. Here, including a Hubbard-U correction and spin-orbit coupling, we reproduce the large MAE of an individual Co adatom on a MgO (001) surface and unveil the mechanism behind it. More importantly, we take one step further by investigating the possibility of enhancing the MAE of 3d transition metal adatoms by considering various structural geometries of 3d–O molecules deposited on MgO. In one of the structures, where the molecules are perpendicular to the surface, the MAE can be enhanced while reducing the interaction with the substrate, which should minimize spin fluctuations and enhance the magnetic stability. Moreover, we evidence the ability to substantially modify the MAE by atomic control of the location of the 3d–O molecules on the substrate and explore the underlying hyperfine interactions.

6.1. Introduction

Surface-embedded molecular magnetic structures are of tremendous interest, as they represent the smallest magnetic units at the ultimate atomic scale [27], [55], [57]. Recent studies on magnetic adatoms with sizeable magnetic anisotropy energy (MAE) has been intense due to their potential applications in high-density information storage and quantum spin processing [8], [23], [34], [172]–[178]. For instance, single Co atoms deposited onto a Pt (111) surface give rise to an MAE of 9 meV per atom favoring an out-of-plane orientation of the magnetic moment, and the assembled Co nanoparticles have an MAE that is reliant on the coordination of a single atom [172]. If the Co atoms are separated from the Pt surface by graphene, the MAE is maintained at a significant value (MAE =8.1 meV) [174]. Ab-initio simulations predicted

the possibility of achieving remarkable MAEs for Co or Ir dimers on graphene (MAE = 60 meV) [175], for Os adatoms on graphene nanoflakes (MAE = 22 meV) [176], and for Co dimers on benzene (MAE = 100 meV) [177]. A substantial out-of-plane MAE would generate an energy barrier that could protect the magnetization from thermal fluctuations, making it robust and stable and allowing the magnetization to be orientated in a preferred spatial direction for a sufficient duration of time, which would be practical for the realization of a magnetic bit.

Strategies for enhancing the MAE of magnetic adatoms are based on three vital aspects: a large spin-orbit coupling (SOC) energy, a significant orbital moment, and a special ligand field [8], [178]. As a ligand field frequently quenches or reduces an orbital moment, by enforcing orbital degeneracies, it is difficult to attain a massive MAE without a suitable surface or substrate. Recently, thin insulating layers of MgO developed into an appealing substrate for exploring various magnetic aspects pertaining to magnetic adatoms and molecules [7], [8], [33]–[53].

On that very substrate, Rau et al., discovered in 2014 that Co adatom adsorbing on the oxygen-top position of the MgO (001) surface (see Fig. 6.1-1) is characterized by a large MAE since the underlying measured zero-field splitting with inelastic STM reaches approximately 60 meV [8]. Assuming a spin $\frac{3}{2}$ for the Co adatom implied reaching a magnetic anisotropy energy of the order of 90 meV [179]. This MAE breaks records and reaches the magnetic anisotropy limit of 3d transition metals. Details of the interaction between Co and MgO surface, for instance the Co–O bond, determines uniquely the underlying magnetic properties. Theoretically, simple LSDA or GGA calculations do not recover the large MAE of Co on MgO. To overcome this issue, we need constrained LSDA + U and LSDA + SOC + U calculations. The recent ab-initio work of Ou et al. [179] predicts that if the simulations are done properly, one can recover the MAE of Co on MgO, and expect larger MAEs for Ru (MAE = 110 meV) and Os on the same surface (MAE = 208 meV).

In this chapter, we investigate the remarkable MAE of Co and other 3d adatoms on MgO surface and explore the possibility of enhancing their by attaching to them an additional O atom in order to form XO molecules (X being a 3d atom), see Fig. 6.1. Of our particular interest is the case where the molecule is perpendicular to the MgO surface, such that the interaction of Co with the substrate is minimized as shown in Fig. 6.1-2, which should reduce the substrate-induced spin fluctuations to a minimum. For completeness, we investigate the impact of the various atomic structures on the underlying hyperfine interactions.

6.2. Computational details

We follow the same numerical procedure as the one provided in chapters 4 and 5. The code projwfc.x code was used to obtain atom- and orbital-resolved spin magnetic moments for further analysis and connection to the hyperfine interactions and the magnetic anisotropy energy (MAE). We applied two formulations of the Hubbard-U correction in this chapter: (i) Dudarev's approach used for structure relaxation and to obtain the hyperfine interactions, and (ii) Liechtenstein's formulation [120] used for MAE calculations. We utilize this hybrid scheme because of their current implementations and stability in the Quantum ESPRESSO code. First, Dudarev's approach is suitable for SOC, atomic relaxations and hyperfine interactions (with GIPAW) but currently incompatible with arbitrary rotations of the magnetic moment, which is an essential ingredient for the evaluation of the MAE. Second, the Liechtenstein's approach works with SOC while enabling the rotation of the magnetic moments but without having access to the structural relaxations and hyperfine field. Thus, in practive, we perform the relaxations and address the hyperfine interaction with the formulation of Dudarev. Once the atomic geometries obtained, we switch to the approach of Liechtenstein et al. to compute the MAE.

SOC-physics is explored within the local spin density approximation (LSDA) [100] as implemented in the Quantum ESPRESSO code with scalar relativistic [127] as well as fully relativistic USPPs and PAWs [142], [143]. While the study on hyperfine interactions was carried out with GGA, here we switch to LSDA because of problems of stability in the self-consistent GGA simulations of the nanostructures deposited on MgO once SOC included.

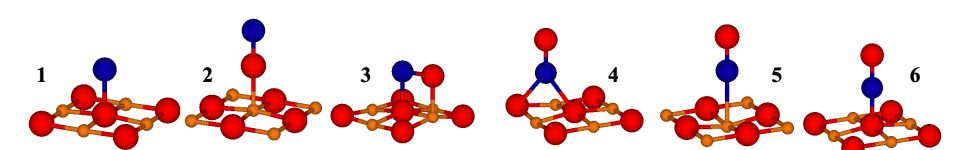


Figure 6.1.: Atomic structures for 3d adatom and 3d-O molecules on a bilayer of MgO. 3d atoms are represented by blue spheres, O by red spheres and Mg by orange spheres.

In this chapter, we discuss two types of simulations: 3d adatoms on the oxygen-top position of the MgO bilayer and 3d–O molecules free-standing or deposited on the MgO bilayer. For the case of free-standing 3d–O molecules, we employed cubic periodic cells with a lattice constant of $20\,\text{Å}$, in order to minimize interactions between periodic replicas of the dimers, and assumed Γ -point sampling of the Brillouin zone while using different bond lengths between 3d adatoms and O atoms (d_{3d-O}). While the unitcells assumed for the adatoms and 3d–O molecules on the bilayer of MgO are the same than those of chapters 4 and 5, here we used two different lattice constants of the MgO bilayer: the one from GGA (see Table 4.1) which equals $4.147\,\text{Å}$ for the

hyperfine interactions calculations, and the one from LDA (4.065 Å) for the MAE calculations. The supercells contain 73 and 74 atoms in total for the case of 3d adatoms on the oxygen-top position and 3d–O molecules deposited on the MgO bilayer MgO, respectively, and a vacuum thickness equivalent to 9 layers of MgO. We adopted a $4\times4\times1$ k-mesh in both cases and the cell dimensions were kept fixed while all atomic positions were allowed to relax in z-axis.

The rotation of the magnetic moment of the free-standing Co–O molecules was studied by the constrained DFT approach explained in Ref. [171], using different types of fully relativistic pseudopotentials [142], [143] to calculate the MAE. In order to ensure that the different magnetic states were comparable, for each fixed magnetic configuration we performed a sequence of self-consistent constrained calculations ramping up the penalty parameter as we did in chapter 5.

PPs	GGA PAW	GGA USPP	LSDA PAW	LSDA USPP
MAE (meV)	-13.5	-12.9	-10.0	-12.84

Table 6.1.: MAE of the isolated Co–O molecule from DFT+SOC total energy calculations for different types of pseudopotentials (PPs) and exchange-correlation functionals, ($d_{\text{Co-O}} = 2\text{Å}$). A negative sign of the MAE favors an out-of-plane magnetization.

As an initial test, we computed the MAE for free-standing Co–O molecules with different types of fully relativistic pseudopotentials shown in Table. 6.1. Since the results were quantitatively similar, we opted for LSDA+USPP for the rest of the MAE calculations due to the low computational cost, especially when we add Hubbard-U correction. The MAE is defined as the difference in the total energies between the two magnetic states: in-plane magnetization along the x-axis and out-of-plane magnetization along the z-axis (MAE = $\mathbf{E}^{\hat{z}} - \mathbf{E}^{\hat{x}}$). In our convention, a negative MAE corresponds to a favorable out-of-plane magnetization.

6.3. MAE of a single Co adatom on the bilayer of MgO

To set the stage for our study, we investigate the MAE of a single Co adatom on a bilayer of MgO surface. We know from section 4.4 that the O-top site is the most stable adsorption site (see Fig. 6.1-1), in agreement with previous studies [8]. We noticed that the MAE as obtained from LSDA + SOC + U + USPP calculations (see Table 6.2) indicates a preference for an out-of-plane magnetization but with values that depend on the Hubbard U (and exchange parameter J). As we can see from the Table 6.2, the MAE for U = 0 eV and J = 0 eV, is the smallest (-10 meV), whereas for U = 4, J = 1 eV (MAE = -145.2 meV), and for U = 6, J = 1 eV (-93.3 meV), it

Co/MgO	U = 0, J = 0	U = 4, J = 1	U = 6, J = 1
MAE (meV)	-10.0	-145.2	-93.3

Table 6.2.: MAE for Co adatom on the bilayer of MgO in the oxygen-top position from LSDA+SOC+U total energy calculations and from Experiment (exp). A negative sign of the MAE favors an out-of-plane magnetization. U and J are given in eV.

reaches the order of magnitude experimental values. To explain the dependence of the MAE on the values of the Hubbard U and exchange parameter J, we plot the corresponding PDOS of Co adatom without including SOC (Fig. 6.2). A common feature in all investigated cases is the degeneracy at the Fermi level of the d_{xz} and d_{yz} states. The rest of the states experience a clear shifts with respect to the Fermi energy as soon as the Hubbard-U correction included, which presumably trigger the aforementioned differences in the MAE.

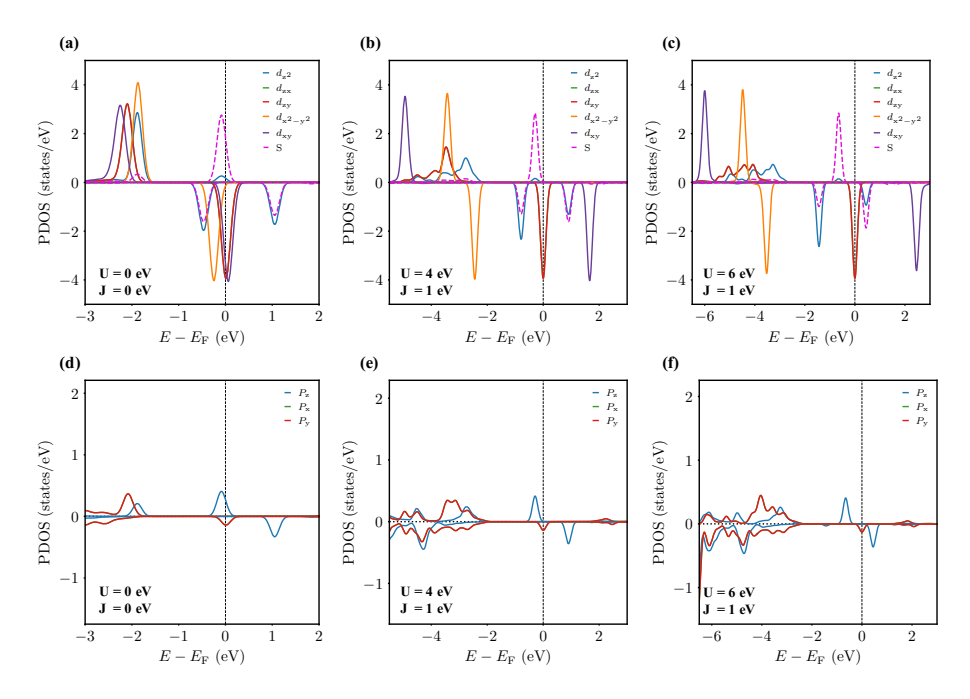


Figure 6.2.: Effect of the Hubbard-U correction on the electronic structure of a Co adatom (a, b, and c) atop oxygen (d, e, and f) from the MgO bilayer of MgO in the absence of SOC. (a, d) PDOS for U = 0 and J = 0, (b, e) PDOS for U = 4 eV and J = 1 eV, (c, f) PDOS for U = 6 eV and J = 1 eV. The Fermi energy is marked by a vertical dashed line.

In the following we utilize degenerate and second-order perturbation theories [180]–[183] in order to unveil the mechanisms shaping the large MAE characterizing the Co adatom once incorporating.

First order degenerate perturbation theory. In our discussion, first, we focus on the case of U=0 eV and J=0 eV, and the other cases will be discussed later. We start by looking at the PDOS for the d-states in Fig. 6.2-a. As aforementioned, the d_{xz} and d_{yz} minority-spin states are degenerate at the Fermi level for which we have to proceed with first-order degenerate perturbation theory [183]–[186] in order to predict the impact of spin-orbit coupling. The z-component of the orbital momentum operator is the only one connecting both orbitals, implying that the SOC term of interest is $\frac{1}{2}\xi\sigma_z \cdot \hat{\mathbf{L}}_z$, which simplifies to $-\frac{1}{2}\xi\hat{L}_z$ since the the two states are of minority-spin character. Here ξ is the radial integral of the SOC with the associated atomic wave functions. This also means that there is gain in energy only when the moment points along the z-direction. We diagonalize the degenerate subuspace including the SOC term:

$$\begin{bmatrix} \hat{H}_{11} & \hat{H}_{12} \\ \hat{H}_{21} & \hat{H}_{22} \end{bmatrix} = -\frac{1}{2} \xi \begin{bmatrix} 0 & \langle d_{xz} | \hat{L}_z | d_{yz} \rangle \\ \langle d_{uz} | \hat{L}_z | d_{xz} \rangle & 0 \end{bmatrix} = -\frac{1}{2} \xi \begin{bmatrix} 0 & 1 \\ 1 & 0 \end{bmatrix}, \quad (6.1)$$

and find as eingenvalues

$$\Delta E_{\pm} = \mp \frac{1}{2} \xi . \tag{6.2}$$

The corresponding eigenstates are: $(d_1^{\downarrow} = \frac{1}{\sqrt{2}}(d_{xz} + d_{yz}))$ for eigenvalue $E_1 = -\frac{1}{2}\xi$ and $(d_2^{\downarrow} = \frac{1}{\sqrt{2}}(d_{xz} - d_{yz}))$ for eigenvalue $E_2 = \frac{1}{2}\xi$. The d_1^{\downarrow} and d_2^{\downarrow} represent bonding and anti-bonding states, respectively. The electron initially shared by both orbitals located at the Fermi energy will be located in the bonding states d_1^{\downarrow} just below the Fermi energy while the d_2^{\downarrow} state becomes unoccupied.

Overall, we conclude that the easy axis along z-direction is strongly favored by the degenerate states located at the Fermi energy, contributing to the MAE by a large value of $-\frac{1}{2}\xi=-35$ meV, where we assumed that $\xi\approx70$ meV for Co [187]. Obviously, it is the degeneracy of the d_{xz} and d_{yz} minority-spin states at the Fermi energy, which is responsible for the large out-of-plane MAE detected experimentally. The differences noticed among the simulations utilizing various values of U and J must be induced by the rest of the states, which are non-degenerate. These will be addressed in the following.

Second-order non-degenerate perturbation theory. Here we evaluate the contributions to the MAE from the non-degenerate states. The MAE is determined by the matrix elements of SOC involving occupied and unoccupied states [180]:

$$MAE_{2^{\text{nd}}\text{order}} = \frac{\xi^2}{4} \sum_{o,u,\sigma,\sigma'} (1 - 2\delta_{\sigma\sigma'}) \frac{|\langle o^{\sigma} | \hat{L}_z | u^{\sigma'} \rangle|^2 - |\langle o^{\sigma} | \hat{L}_x | u^{\sigma'} \rangle|^2}{\epsilon_{u,\sigma'} - \epsilon_{o,\sigma}}, \qquad (6.3)$$

where $o^{\sigma}(u^{\sigma'})$ and $\epsilon_{o,\sigma}(\epsilon_{u,\sigma'})$ represent eigenstates and eigenvalues of occupied (unoccupied) states in spin state $\sigma(\sigma')$. Nonzero \hat{L}_z and \hat{L}_x matrix elements involving d-states are summarized in Table 6.3. Considering that all the majority-spin states are fully occupied and rather far away from the Fermi energy, as shown in Fig. 6.2, the dominant contribution to the MAE can be attributed to the minority-spin states, spin-down occupied and spin-down unoccupied states, $\sigma(\sigma' = (\downarrow \downarrow))$. We neglect spin-flip contributions from spin-up occupied and spin-down unoccupied states for the qualitative analysis carried out in this section. In fact, there is a satellite majority-spin d_{z^2} state showing up close to the Fermi energy. However, it emerges from the p_z state of the underlying oxygen atom, which gives rise to a prominent s-state (shown as a dashed line in Fig. 6.2). But even if we include it, its contribution vanishes.

Cartesian	$\langle \hat{L_{\sigma}} \rangle$
$\langle d_{xz} \hat{L_z} d_{yz}\rangle$	1
$\langle d_{x^2-y^2} \hat{L}_z d_{xy}\rangle$	2
$\langle d_{z^2} \hat{L_x} d_{xz}, d_{yz} \rangle$	$\sqrt{3}$
$\langle d_{xy} \hat{L}_x d_{xz}, d_{yz} \rangle$	1
$\left \langle d_{x^2 - y^2} \hat{L_x} d_{xz}, d_{yz} \rangle \right $	1

Table 6.3.: Nonvanishing angular momentum matrix elements between d-states. The notation is given for the d-states in Cartesian coordinates with z being the quantization axis, in units of \hbar .

There are three finite dominant contributions to Eq. 6.3:

$$\mathrm{MAE_{2^{\mathrm{nd}}\mathrm{order}}} = -\frac{\xi^{2}}{4} \ \frac{|\langle d_{x^{2}-y^{2}}^{\downarrow} | \hat{L}_{z} | d_{xy}^{\downarrow} \rangle|^{2}}{\epsilon_{xy,\downarrow} - \epsilon_{x^{2}-y^{2},\downarrow}} \ + \frac{\xi^{2}}{4} \ \frac{|\langle d_{1}^{\downarrow} | \hat{L}_{x} | d_{z^{2}}^{\downarrow} \rangle|^{2}}{\epsilon_{z^{2},\downarrow} - \epsilon_{1,\downarrow}} \ + \frac{\xi^{2}}{4} \ \frac{|\langle d_{1}^{\downarrow} | \hat{L}_{x} | d_{xy}^{\downarrow} \rangle|^{2}}{\epsilon_{xy,\downarrow} - \epsilon_{1,\downarrow}} \ , \tag{6.4}$$

which are listed for different values of U and J and compared to the value obtained from first-order degenerate perturbation theory in Table 6.4. Since static correlations increase the energy splitting between the occupied $d_{x^2-y^2}^{\downarrow}$ and unoccupied d_{xy}^{\downarrow} , the first term in Eq. 6.3, favoring the out-of-plane easy-axis, reduces in magnitude. The same trend is followed by the third term, which however favors an in-plane orientation of the moment in contrast to the second term. Clearly, there is a complex competition between the different terms, which imposes a strong reduction of the MAE emerging from first-order degenerate perturbation theory.

After summing up the different contributions to the MAE as obtained from firstand second-order pertubration theory, we recover qualitatively the trends found from

MAE	U = 0, J = 0	U = 4, J = 1	U=6, J=1
$-\frac{\xi^2}{4} \; \frac{ \langle d_{x^2-y^2}^{\downarrow} \hat{L_z} d_{xy}^{\downarrow} \rangle ^2}{\epsilon_{xy,\downarrow} - \epsilon_{x^2-y^2,\downarrow}}$	-15.7547	-1.1919	-0.8170
$+\frac{\xi^2}{4} \frac{ \langle d_1^{\downarrow} \hat{L_x} d_{\underline{z}^2}^{\downarrow} \rangle ^2}{\epsilon_{z^2,\downarrow} - \epsilon_{1,\downarrow}}$	6.9665	8.1303	16.7347
$+\frac{\xi^2}{4}\;\frac{ \langle d_1^{\downarrow} \hat{L_x} d_{xy}^{\downarrow}\rangle ^2}{\epsilon_{xy,\downarrow}-\epsilon_{1,\downarrow}}$	38.8888	1.4749	1.0008
$MAE_{degenerate} = -\frac{1}{2}\xi$	-35.0	-35.0	-35.0
Σ =	-4.8994	-26.5867	-18.0815

Table 6.4.: Various contributions from first-order degenerate and second-order non-degenerate perturbation theories to the MAE of Co adatom on the bilayer of MgO in the oxygen-top position from DFT+U with the absence of SOC. A negative sign of the MAE favors an out-of-plane magnetization. U and J are given in eV, while the MAE is in meV.

the full ab-initio calculations as reported in Tables 6.2 and 6.4. This shows that the main mechanism favoring the out-of-plane orientation of the magnetic moment with a large MAE is driven by the SOC-induced lifting of the degeneracy of the minority-spin d_{xz} and d_{yz} states located at the Fermi energy. We note that there is an excellent agreement with a previous theoretical study [179] based on full-potential augmented plane wave calculations. Their argument, however, to explain the large MAE of Co adatom is different from ours and is based on a non-trivial reordering of the occupation matrix generated with static correlations.

In the next section, we investigate the MAE of other 3d adatoms deposited on MgO and explore the possibility of enhancing their MAE by considering 3d–O molecules as potential adsorbates (see Fig. 6.1). In the following we limit our simulations to the case of U=6 and J=1 eV since the MAE value obtained for Co adatoms is the closest to the experimentally measured one [8]. We will use an identical U value, when addressing the hyperfine interaction.

6.4. Magnetic Anisotropy Energy of 3d adatoms and 3d–O molecules on the bilayer of MgO

Here, we address the main topic of our investigation, namely 3d adatoms on the bilayer of MgO and the 3d–O molecules placed on the MgO bilayer considering different structures. After structural relaxation, using LSDA + U (U = 6 eV and J = 1 eV) total energy calculations, we classified the results into six structures shown in Fig. 6.1. As shown in Fig. 6.3, structure 6 is energetically the most favorable one for all 3d–O molecules except for the Sc–O molecule case, while structure 5 is the one that is the

least favorable. Independent from their relative stability, we study the MAE of all the converged nanostructures.

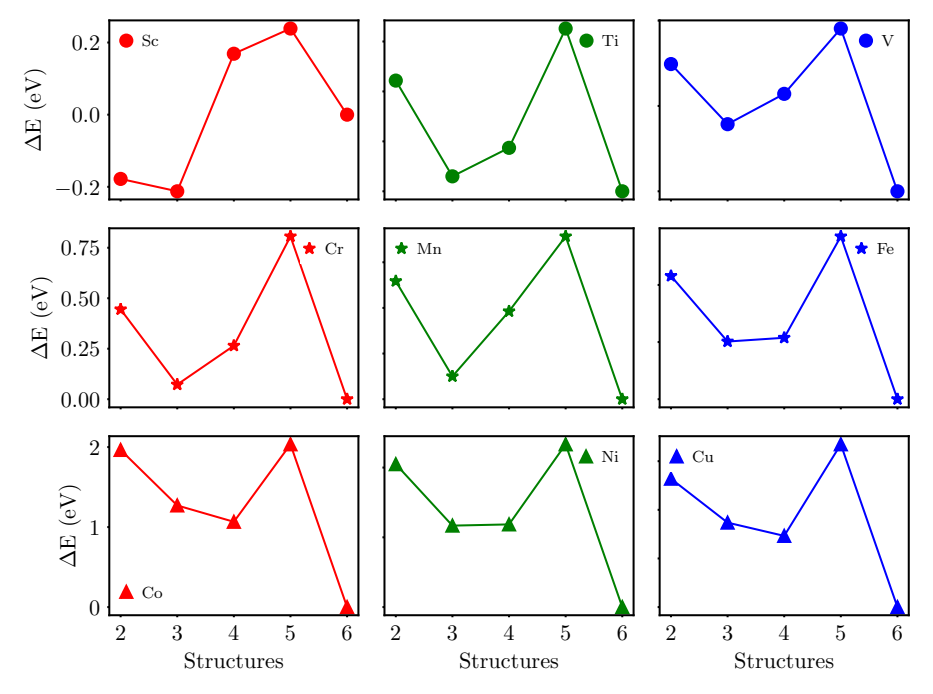


Figure 6.3.: Total energy difference of 3d-O molecules on the bilayer of MgO with respect to the one of structure 6. The structure number indicates a particular nanostructure illustrated in Fig. 6.1. Results obtained by LSDA + U + USPP calculations.

Most of the investigated structures have C_{4V} symmetry except for structures 3 and 4. For the latter cases, we explore various in-plane rotations of the magnetization and calculate the MAE as follows:

$$MAE = E^{\hat{z}} - E^{\phi} , \qquad (6.5)$$

where ϕ is the azimuthal angle. To monitor the different investigated cases including the extra scenarios with different orientations of the magnetization ($\phi = 45^{\circ}$) and [010] ($\phi = 90^{\circ}$), we rename the structures in Fig. 6.1 and defined new ones as shown in Fig. 6.4.

It is valuable to explore how the magnetic moments of the 3d atoms are changed once embedded in the 3d-O molecules as summarized in Fig. C.1 of Appendix. In contrast to the single adatoms, 3d-O molecules follow Hund's first rule. As a reminder,

in the single adatom case (Fig. 6.4-1), 3 atomic species do not follow Hund's first rule: Ni, Ti and V, similar to what we reported in chapter 4 without U. The spin moments of the different deposited nanostructures are generally unaffected by the positions of the 3d-O molecules (Fig. C.1 of Appendix) and the electronic occupation is consistent with a nominal valence of $[Ar]4s^23d^n$. We did not show any data for Cr due to computational difficulties to reach self-consistency with LSDA + SOC + U + USPP.

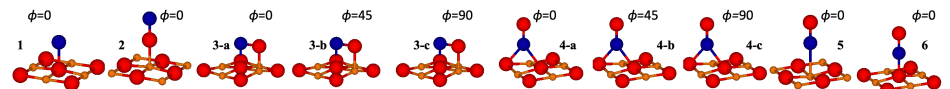


Figure 6.4.: Magnetization directions along [100], [110], and [010] corresponding to ϕ = 0°, 45°, and 90°, respectively, for 3d adatoms and 3d–O molecules on a bilayer of MgO. 3d atoms are represented by blue spheres, O by red spheres and Mg by orange spheres.

The underlying MAE is shown in Fig. 6.5. Ti, Fe, Co, and Ni structures generally yield significant MAE ranging from a few to tens meV. At the same time, the MAE values of Sc, V, Mn, and Cu are close to zero for all structures except the Cu–O molecule, which is characterized by an out-of-plane MAE of 2.35 and 2.25 meV in structures 5 and 6, respectively.

Among all the 3d adatoms and 3d–O molecules, a single Co adatom on the bilayer of MgO in the oxygen-top position exhibits the most significant MAE values (an out-of-plane MAE of 93 meV), representing the magnetic anisotropy limit of 3d adatoms and 3d–O molecules on MgO as obtained from our simulations. Moreover, Co–O molecule in structure 2 (see Fig. 6.1-2) is perpendicular and has the second largest out-of-plane MAE of 53 meV compared to the rest of explored nanostructures, see Fig. 6.5. A closer look at the Ti MAE values in Fig. 6.5 reveals that the perpendicular Ti–O molecule in structure 2 has the largest in-plane MAE of 45 meV, with the remaining structures MAE values significantly decreasing (range between 0 and 4 meV). Except for structure 3-a, Co–O molecules prefer all an out-of-plane orientation of the magnetization.

We expect structure 2, to be the one where the 3d atoms are less interacting with the substrate, which should favor magneic stability if allowed by the right out-of-plane MAE. In principle its MAE should be close to the free standing molecule. To examine this scenario, we calculated the MAE of the isolated Co–O molecule for different bond lengths between Co and O atoms ($d_{\text{Co-O}}$), see Table 6.5, to cover all the bond lengths of Co–O molecules on the bilayer of MgO (structures 2 to 6 in Fig. 6.1). Table 6.5 shows an excellent agreement between the computed MAE of the isolated Co–O molecule and the perpendicular Co–O molecule on the MgO bilayer, which confirms our expectations. Moreover, Table 6.5 reveals a minimal effect of the bond length on the computed MAEs of the isolated Co–O molecule.

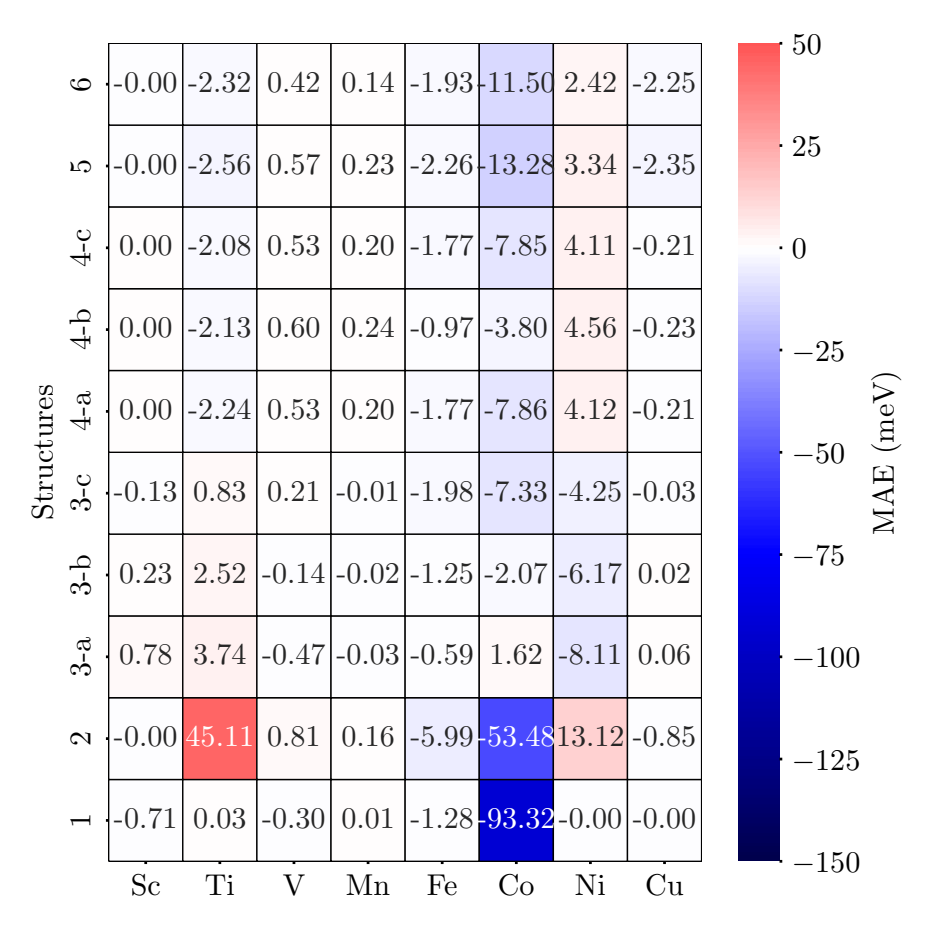


Figure 6.5.: MAE of 3d adatoms and 3d–O molecules on a bilayer of MgO. The structure number indicates a particular nanostructure with a specific orientation of the magnetization as illustrated in Fig. 6.4. A negative sign of the MAE favors an out-of-plane magnetization. Results obtained by LSDA + SOC + U + USPP calculations.

Although the perpendicular Co–O molecule (structure 2 in Fig. 6.1) is energetically less stable than the horizontal one (structure 3 in Fig. 6.1) on the MgO bilayer (see Fig. 6.3), which has a very small MAE compared to the perpendicular one, it is of great interest to figure out whether the former structure (2) is metastable and could be protected by an energy barrier, which would enable its experimental realization. To address this aspect, we considered the perpendicular Co–O molecule on the MgO

d _{Co-O} (Å)	1.7	1.8	1.9	2	CoO/2MgO
MAE (meV)	-46.06	-48.25	-50.89	-52.11	-53.48

Table 6.5.: MAE of the isolated Co–O molecule from LSDA+ SOC + U total energy calculations for different bond lengths between Co and O atoms (d_{Co-O}). CoO/2MgO is the perpendicular Co–O molecule on the MgO bilayer (see Fig. 6.1-2 and Fig. 6.4-2). A negative sign of the MAE favors an out-of-plane magnetization. Here we used U = 6 and J = 1 eV.

bilayer and rotated it in the zx-plane till installing the molecule parallel to the substrate, as shown in Fig. 6.6.

As one sees in Fig. 6.6-b, there is an energy barrier of 0.6 eV that should prevent the perpendicular Co–O molecule from falling parallel to substrate, which indicates that it is a metastable state. Fe–O molecule, in contrast, seems to prefer a tilted configuration with a large barrier identified at an angle of 45°, see Fig. 6.7-b. It is definitely of interest to motivates experiments on such perpendicular molecules. Certainly, we need to extend in the future these theoretical investigations. In the next section, we analyse the hyperfine interactions of all the molecules investigated in the current chapter.

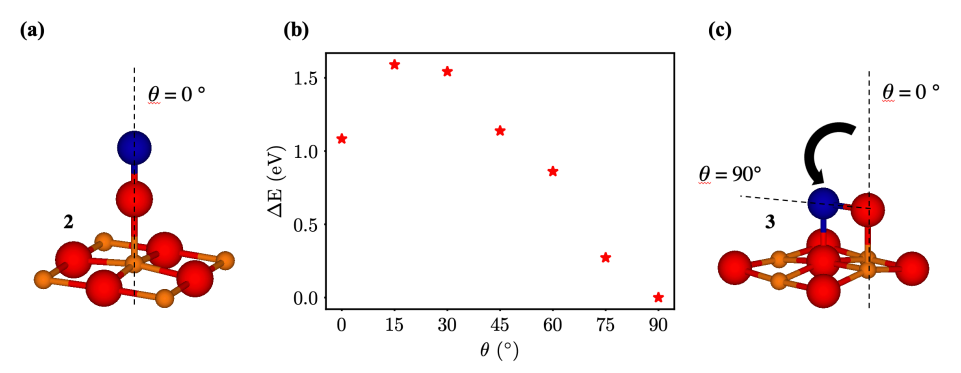


Figure 6.6.: Energy barrier for the metastable perpendicular Co–O molecule on the bilayer of MgO. (a) the perpendicular Co–O molecule on the MgO bilayer $(\theta=0^{\circ})$, (b) total energy difference of Co–O molecule on the bilayer of MgO with respect to structure 3, as a function of the rotating angle (θ) and (c) The horizontal Co–O molecule on the MgO bilayer $(\theta=90^{\circ})$. θ is the rotation angle away from the z-axis towards the x-axis. Here we used U=6 and J=1 eV.

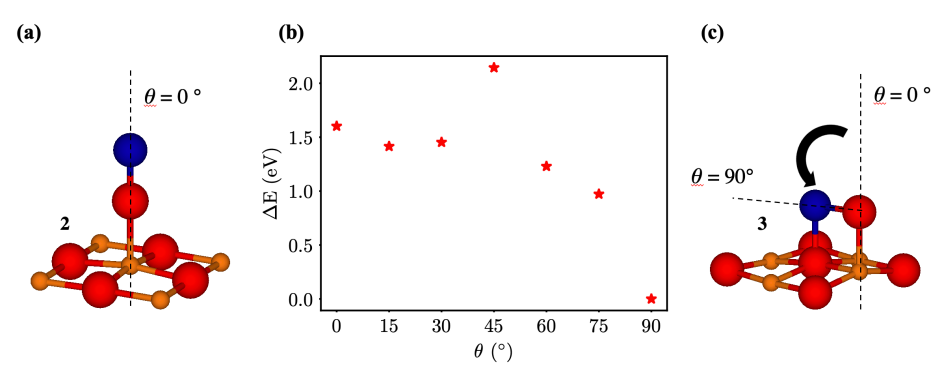


Figure 6.7.: Energy barrier for the metastable perpendicular Fe–O molecule on the bilayer of MgO. (a) the perpendicular Fe–O molecule on the MgO bilayer $(\theta=0^{\circ})$, (b) total energy difference of Fe–O molecule on the bilayer of MgO with respect to structure 3, as a function of the rotating angle (θ) and (c) The horizontal Fe–O molecule on the MgO bilayer $(\theta=90^{\circ})$. θ is the rotation angle away from the z-axis towards the x-axis. Here we used U=6 and J=1 eV.

6.5. Hyperfine interactions

In chapter 4, we systematically quantified from first-principles the hyperfine interactions of the whole series of 3d transition adatoms deposited on various thicknesses of MgO, NaF, NaCl, h–BN, and Cu₂N films. We identified the adatom-substrate complexes with the largest hyperfine interactions and unveiled the main trends and exceptions. In addition, we provided a general map of hyperfine interactions for the 3d transition adatoms on various ultra-thin insulators. Furthermore, we demonstrated the ability to substantially modify the hyperfine interactions by atomic control of the location of the adatoms on the substrate. In chapter 5, we explored the case of dimers by investigating the correlation between the hyperfine interactions and the magnetic state of free standing Fe dimers, single Fe adatoms, and dimers deposited on the MgO bilayer. We found that the magnitude of the hyperfine interactions can be controlled by switching the magnetic state of the dimers and by changing Fe-Fe distances on the MgO bilayer.

In this section, we explore the hyperfine interactions of the 3d-O molecules on MgO shown in Fig. 6.1 and take as a reference for comparison the one associated to the 3d adatoms atop oxygen studied in the current chapter. As mentioned earlier with use a value of U=6 eV in our simulations with GGA. As a sanity check, we compared the spin moments obtained with both types of exchange and correlations functionals, GGA and LSDA (utilized for the MAE) for all the investigated nanostructures. The only discrepancy occurred for Ni–O molecules, which do not follow Hund's first rule in GGA (see Fig. C.3 of Appendix) opposite to what we found in LSDA. Ni–O molecule

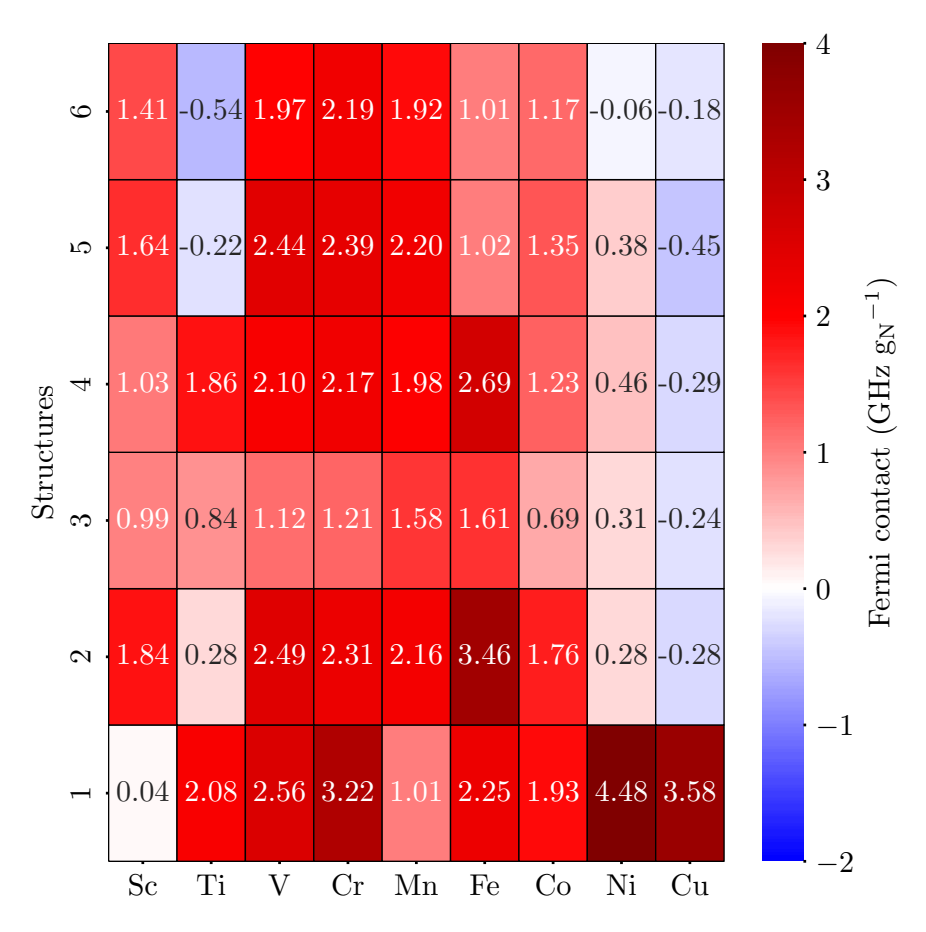


Figure 6.8.: Fermi contact contribution to the hyperfine interaction of 3d adatoms and 3d–O molecules on a bilayer of MgO. The structure number indicates a particular nanostructure illustrated in Fig. 6.1. Here we used U = 6 eV. Results obtained by GGA + U + PAW calculations.

carries a rather small spin magnetic moment of about $0.72\,\mu_{\rm B}$ in structure 2, which vanishes in structures 3 and 4 (see Fig. C.3 of Appendix). As done previously, we focus on the Fermi contact term, the dominant contribution to the hyperfine interactions. As mentioned in chapter 4, we neglect in our analysis effects induced by SOC since it was already found to have a negligible impact on the computed hyperfine interactions for transition metal centers and even for heavy atoms [149], [150]. We also choose not to discuss the dipolar contribution to the hyperfine interaction, as we found it to make a small contribution. The trends of the structural relaxations

obtained with GGA + U + PAW shown in Fig. C.2 of Appendix are similar to the ones reported in this chapter with LSDA + U + USPP (Fig. 6.3).

The Fermi contact contribution to the hyperfine interaction is shown in Fig. 6.8. The extra oxygen atom in the 3d-O molecules leads to a dramatic impact on the hyperfine interaction. For instance, the large Fermi contact term obtained for Ti, Ni and Cu adatoms collapses with the possibility of changing sign. For Fe, the interaction increases slightly for structure 2, while Sc experiences a significant Fermi contact term in contrast to the initially negligible value obtained as an isolated adatom. The remaining 3d adatoms have a rather stable hyperfine interaction.

Following our analysis in chapters 4 and 5, there is no need to stress that the physics of the Fermi contact contribution to the hyperfine interaction can be grasped by the s-contribution (S-spin magnetic moment) to the total spin magnetic moment (Fig. C.4 of Appendix), which emerges from s-orbitals that can overlap with the nucleus. It is interesting to compare how the Fermi contact term for the 3d adatoms atop oxygen compares with those we report in Figs. 4.11a, where the Hubbard-U correction was not included. The magnitude of the Fermi contact changes weakly, while the general trends are not altered. We noted, however, that for Ni adatom, the Fermi contact changes sign and becomes negative once the Hubbard-U included. More detailed comparison of various properties can be grasped from Figs. C.5 - C.9 of Appendix.

6.6. Conclusion

We presented the results of ab initio calculations on the MAE and the Fermi contact contribution to the hyperfine interaction of 3d—O molecules free-standing or deposited on the MgO bilayer, which were compared to the case of 3d adatoms on the oxygen-top position of the MgO bilayer. We explored, in particular, their structural, electronic, and magnetic properties and scrutinized the impact of the existence of an extra oxygen atom attached to 3d adatoms on the MAE and Fermi contact. On the one hand, the physics of MAE is mainly explained by applying degenerate and non-degenerate perturbation theories. On the other hand, the physics of Fermi contact is dictated primarily by the polarization of the s electrons at the nucleus position as discussed in previous chapters.

We evidenced the ability to substantially modify the MAE via atomic control of the location of the 3d-O molecules on the bilayer of MgO substrate. In particular, we revealed the possibility of having the 3d-O molecules perpendicular to the substrate with the 3d adatom being atop the oxygen atom of the molecule, which should minimize spin-fluctuations triggered by the interaction with the substrate. These molecules can be characterized by large MAE similar to that of the isolated Co adatom. Both aspects, large MAE and weak coupling to the substrate are the

right ingredients to enable magnetic stability of the nanostructure, which so far has not been achieved for 3d adatoms. In fact, the perpendicular 3d–O molecules on the bilayer of MgO act like the isolated 3d–O molecule indicating the weak impact of the substrate on the MAE, especially in the cases of Co–O, Ti–O, Ni–O, and Fe–O perpendicular molecules. Although the aforementioned perpendicular molecule is a metastable structure, it could be protected by an energy barrier, which makes its experimental realization via atomic manipulation with STM possible. Moreover, we evidenced the ability to substantially modify the MAE by atomic control by controlling the location of the 3d–O molecules on the substrate.

Simultaneously, we proved that the Fermi contact term of several of the 3d-O molecules can be engineered depending on their location and show significance differences with respect to the isolated 3d adatoms.

7. Conclusions

In this thesis, we conducted a comprehensive study using first-principles calculations to investigate the hyperfine interactions and the magnetic anisotropy energy of 3d magnetic adatoms and more complex nanostructures on various ultra-thin insulating layers. We utilized density functional theory as a theoretical framework to obtain structural, electronic, and magnetic properties while scrutinizing the hyperfine interactions and the magnetic anisotropy energies of the explored materials.

In the first results part of the thesis, chapter 4, we thoroughly and systematically investigated the hyperfine interactions of single 3d magnetic adatoms on various ultrathin insulating layers. We explored the electronic and structural properties as well as the spin magnetic moments to gain insights into the underlying hyperfine interactions. Our study demonstrates the significance of considering the strength of the interaction between the adatom and the thin film and the local atomic arrangement in understanding the hyperfine interactions. We also highlighted the potential of hyperfine interactions to provide unique information on the electronic structure and magnetism of these adatoms. We used free-atom calculations as a reference to compare and contrast the behavior of the adatoms on different films. Additionally, we described the two components of hyperfine interactions, Fermi contact and dipolar, and how they can be used to track the relative energies of the s and d levels. We also discussed the most important properties that determine the behavior of magnetic adatoms and how they can be challenging to compute accurately. We suggested that future studies should consider adopting hybrid functionals or other nonlocal exchange-correlation corrections and noted the potential issue of spin contamination.

In chapter 5, the second part of the results of the thesis, we focused on the hyperfine interaction of free-standing Fe dimers and Fe dimers deposited on a bilayer of MgO and compared them to the case of isolated Fe adatoms. The dimers are representatives of the smallest multi-atomic nanostructures that can be deposited on a substrate. We investigated the influence of inter-adatom distance and magnetic state on the Fermi contact term, which is the main contribution to the hyperfine interaction. Our results showed that the magnetic alignment of the moments had a significant impact on the magnitude of the Fermi contact term. When considering the Hubbard-U correction, the qualitative behavior is the same for most structures, with some variation in the quantitative behavior. We also proposed an extended hyperfine-Heisenberg Hamiltonian to describe the interplay of magnetic coupling and hyperfine interaction in multi-atomic structures. Our findings suggest the possibility of controlling the Fermi contact term by manipulating the magnetic state of the nanostructure. Additionally,

we showed that atomic control can modify the Fermi contact term by controlling the location of the adatoms on the substrate.

In the third part of the results of the thesis, chapter 6, we presented ab initio calculations on the magnetic anisotropy energy (MAE) and Fermi contact contribution to the hyperfine interaction 3d-O molecules free-standing or deposited on the MgO bilayer, which were compared to those characterizing 3d adatoms on the oxygen-top position of the MgO bilayer. We identify the mechanism behind the large MAE measured experimentally for a Co adatom on MgO, which consists on the spin-orbit coupling-induced lifting of degeneracy of d-orbitals initially located at the Fermi energy. The chapter examines the impact of an extra oxygen atom attached to 3dadatoms on the MAE and Fermi contact and explores the structural, electronic, and magnetic properties of the molecules. The study shows that the MAE can be substantially modified via atomic control of the location of the 3d-O molecules on the bilayer of the MgO substrate. The perpendicular 3d-O molecules on the bilayer of MgO act like the isolated 3d-O molecule, indicating the weak impact of the substrate on the MAE. The study also reveals that the Fermi contact term of several of the 3d-O molecules can be engineered depending on their location and show significant differences with respect to the isolated 3d adatoms.

The findings from our study offer valuable insights into predicting the properties of unexplored systems and identifying engineering requirements for desired hyperfine characteristics in the field of quantum control of surface spins, which ultimately might be useful in the future aim of implementing adatom qubits on surfaces to realize basic concepts fundamental for quantum computing. Additionally, our research enhances our understanding of hyperfine interactions in multi-atomic structures and opens research avenues to explore the non-trivial impact of complex magnetism on the hyperfine interaction. The latter might be utilized to sense the magnetic nature of the surrounding environment and vice-versa, exciting the system magnetically could be utilized to engineer the magnitude of the hyperfine interaction as well as the frequency of the associated excitation modes. Finally, our findings on the 3d–O molecules deposited on MgO is an appealing proposal for the experimental community to realize magnetically stable 3d magnetic adatoms, an aspect so far not yet achieved. This could have significant implications for upcoming research in the field.

In future research, this work can be extended by exploring the hyperfine interactions of 4f adatoms. Intriguingly, those adatoms are the first smallest nanostructures where magnetic stability was demonstrated for relatively long times [7], [37], [51], [188], [189]. Considering the strong localization of the f states carrying the magnetic moments with contributions from the d states, we expect potentially strong spin-polarization of the s-states from which can emerge gigantic hyperfine interactions. An important mechanism to the instability of magnetic moments is the presence of vibrational modes [21]. It would be of great interest to investigate how vibrations affect the magnitude of the hyperfine interactions. Intuitively, we expect the s-spin-

polarization to be modified if a phonon mode is excited. The latter can then be utilized to engineer dynamically the hyperfine interaction. Ultimately, it is appealing to utilize the findings of our thesis in realizing a proof of concept of a network of adatom-qubits based on nuclear spins in combination with the electronic ones. A schematic representation of our proposed device is depicted in Fig. 7.1.

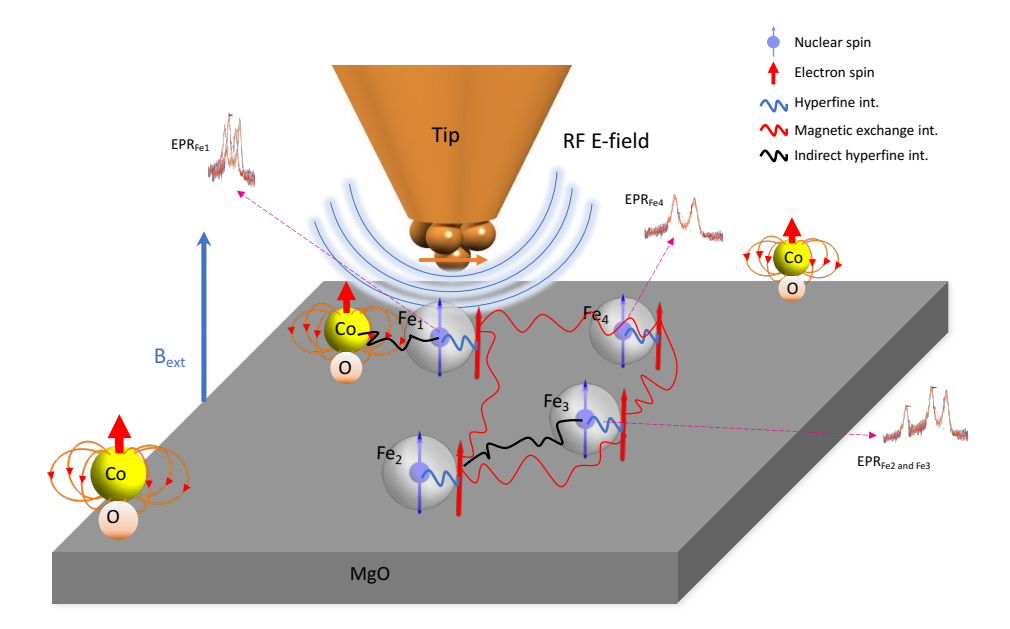


Figure 7.1.: Schematic view on a possible network of hybrid qubits involving the nuclear and electronic spins constructed atom-by-atom, probed and coherently driven by an STM tip equipped with RF voltage pulses. Within the probed Fe adatom, the nuclear magnetic moment interacts with the electronic one via the hyperfine interaction. As shown in the thesis, a neighboring Fe magnetic moment imposes a magnetic interaction, which can be either ferromagnetic or antiferromagnetic, and more importantly it can modify the hyperfine interaction. The perpendicular 3d—O molecules predicted in our work could potentially be utilized as stable magnets which dictate an exchange field on a particular qubit.

We foresee the potential of utilising STM-ESR equipped, as conventionally available, with a radio-frequency bias voltage, which can impose distinct pulses of the bias voltage. The latter could in principle coherently, without being subject to a tunneling current, address adatoms that are not sitting directly underneath the tip-apex. The electronic magnetic moment can then be driven to an excitation mode, which will be affected by the nuclear moment owing to the presence of the hyperfine interaction. As shown in our thesis, the magnetic state of a given nuclear spin can also be con-

trolled by a nearby magnetic adatom, which depends on their mutual distance and their respective location. We envision the possibility of constructing a complex set of hybrid qubits (hybrid since this involves the electronic spin besides that of the nuclear one), engineered atom-by-atom. The magnetic nanostructures showing high magnetic stability, as expected for the 3d-O molecules, could be utilized to impose a robust and stable exchange field, whose magnitude can be tuned depending on the distance with respect to the adatom-qubits. We foresee the utilization of one of the adatoms as a sensor that can be probed directly underneath the STM tip. While our proposed scenario faces various challenges for its successful realization, it provides an exciting prospective project.

A. Appendix-chapter 4

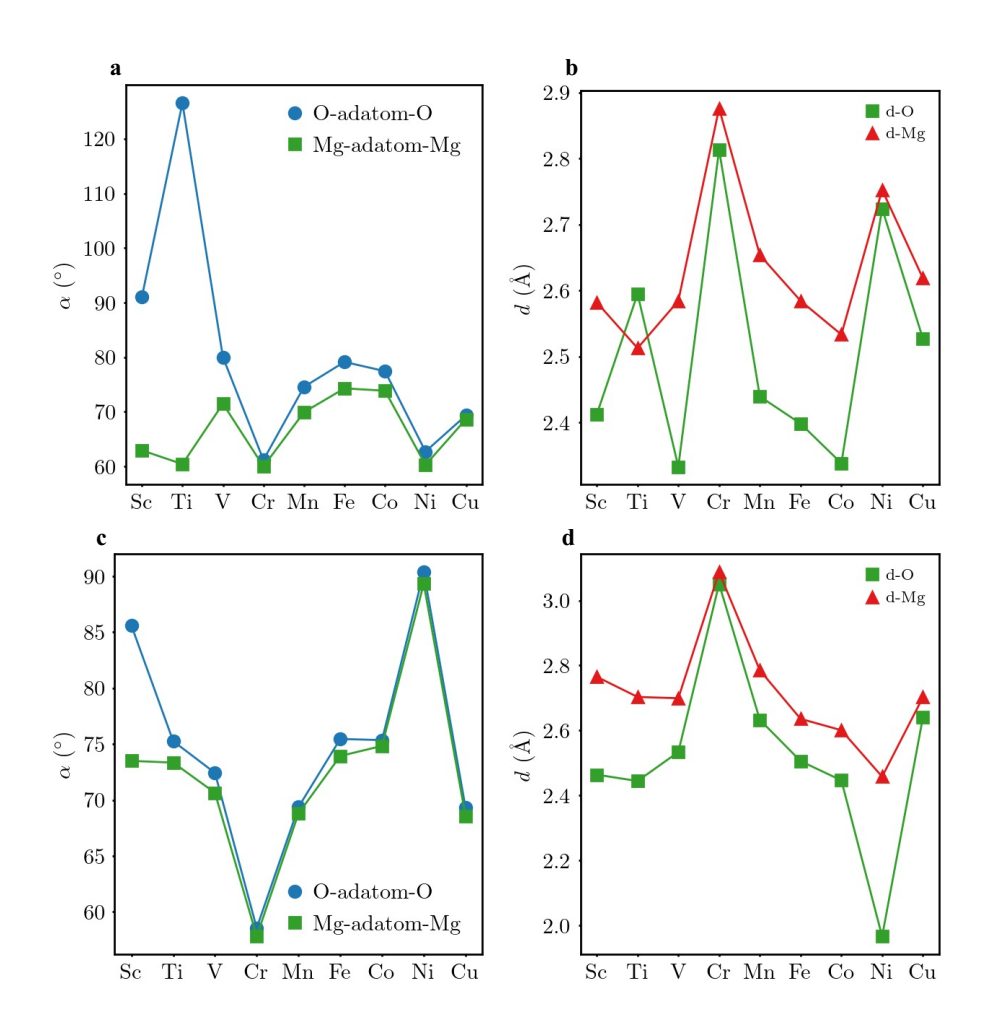


Figure A.1.: Relaxed geometrical properties of adatoms on MgO ultra-thin films, placed on the bridge position. (a,c) Mg-adatom-Mg and O-adatoms-O bond angle and (b,d) distance between the adatom and Mg and O. (a,b) results for single layer and (c,d) results for two layers of MgO.

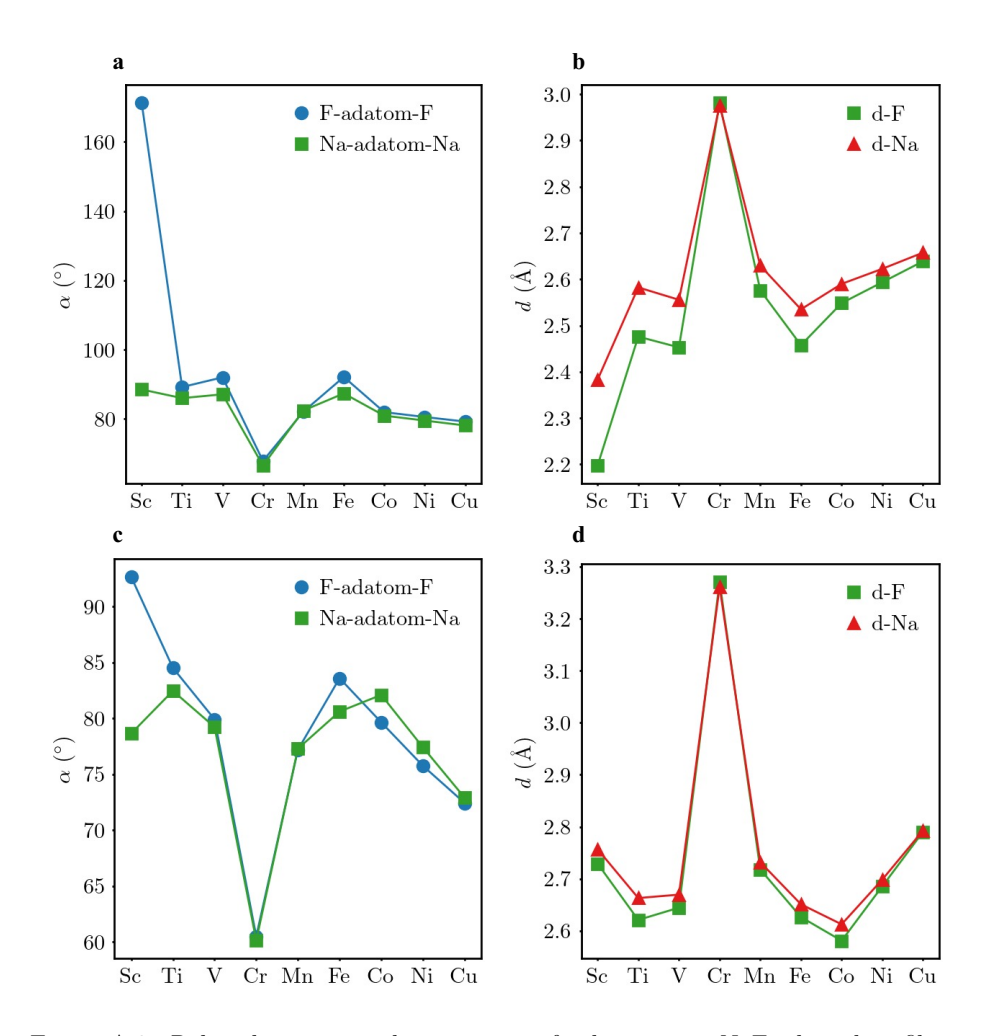


Figure A.2.: Relaxed geometrical properties of adatoms on NaF ultra-thin films, placed on the bridge position. (a,c) F-adatom-F and Na-adatom-Na bond angle, (b,d) Distance between the adatom and either F or Na. (a,b) results for single layer and (c,d) results for two layers of NaF.

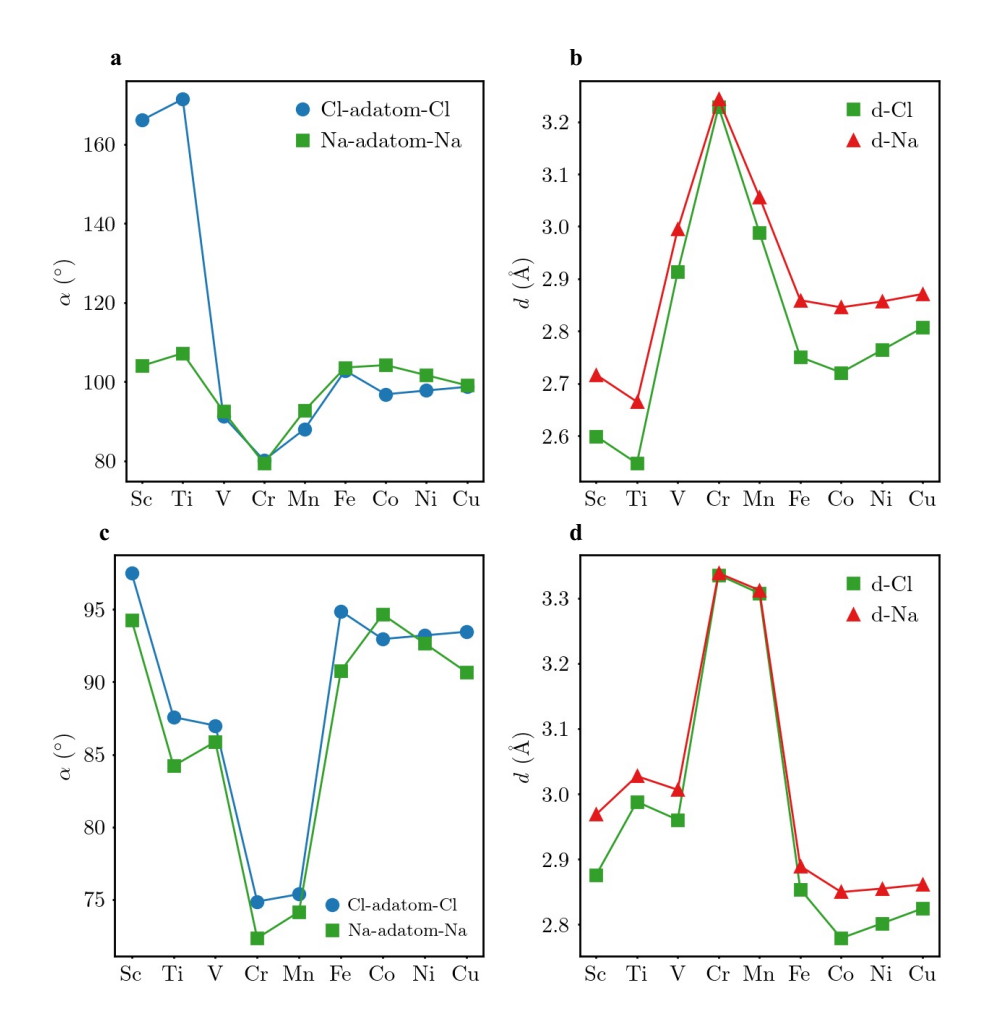


Figure A.3.: Relaxed geometrical properties of adatoms on NaCl ultra-thin films, placed on the bridge position. (a,c) Cl-adatom-Cl and Na-adatom-Na bond angle, (b,d) Distance between the adatom and either Cl or Na. (a,b) results for single layer and (c,d) results for two layers of NaCl.

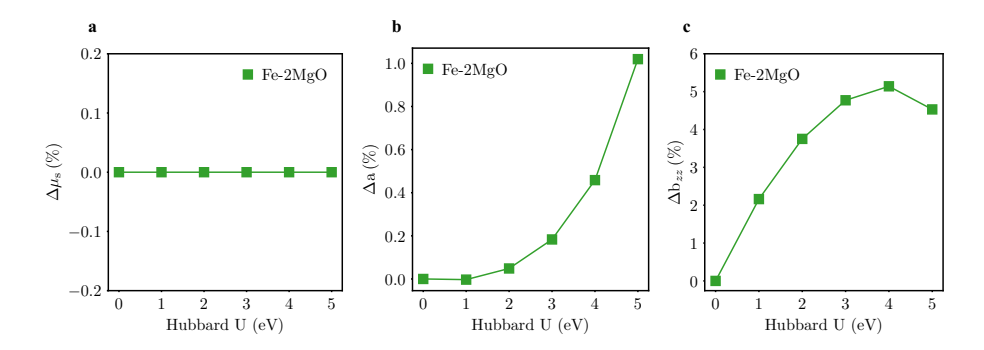


Figure A.4.: Effect of the Hubbard-*U* correction on the properties of the Fe adatom on the oxygen-top position for two layers of MgO. (a) Change in the spin moment. (b) Change in the Fermi contact contribution to the hyperfine interaction. (c) Change in the dipolar contribution to the hyperfine interaction.

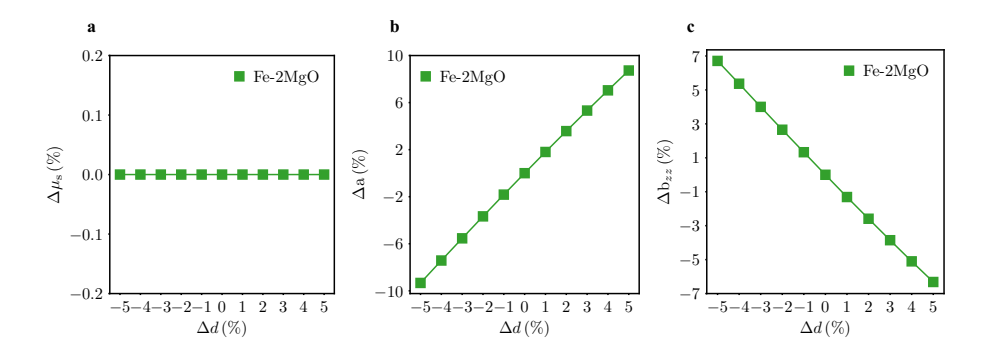


Figure A.5.: Effect of changing the bond length on the properties of the Fe adatom on the oxygen-top position for two layers of MgO. (a) Change in the spin moment. (b) Change in the Fermi contact contribution to the hyperfine interaction. (c) Change in the dipolar contribution to the hyperfine interaction. The previously optimized geometry was kept fixed, and only the position of the Fe adatom was changed.

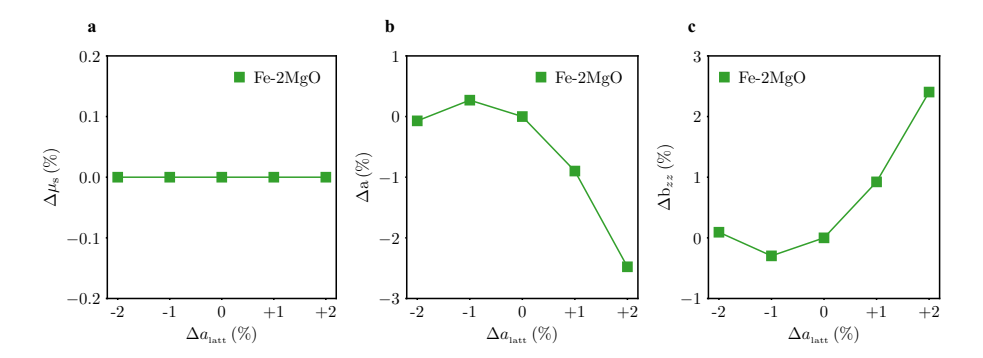


Figure A.6.: Effect of changing the lattice constant on the properties of the Fe adatom on the oxygen-top position for two layers of MgO. (a) Change in the spin moment. (b) Change in the Fermi contact contribution to the hyperfine interaction. (c) Change in the dipolar contribution to the hyperfine interaction. The geometry was optimized for each value of the lattice constant.

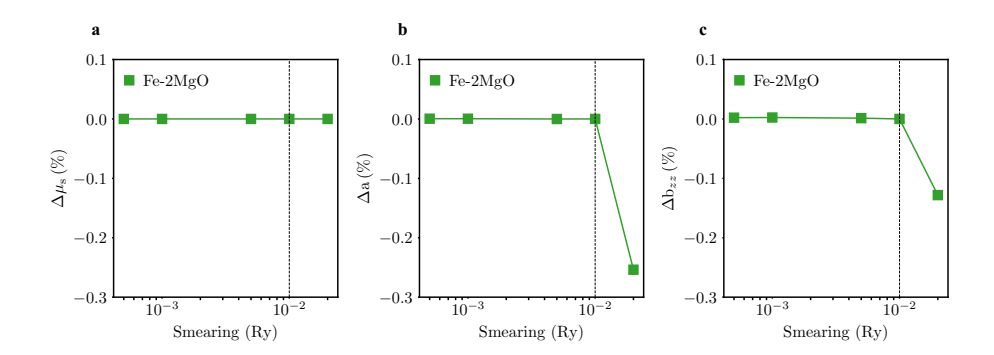


Figure A.7.: Effect of the smearing parameter on the properties of the Fe adatom on the oxygen-top position for two layers of MgO. (a) Change in the spin moment. (b) Change in the Fermi contact contribution to the hyperfine interaction. (c) Change in the dipolar contribution to the hyperfine interaction. The vertical dashed line indicates the value used for systematic calculations.

B. Appendix-chapter 5

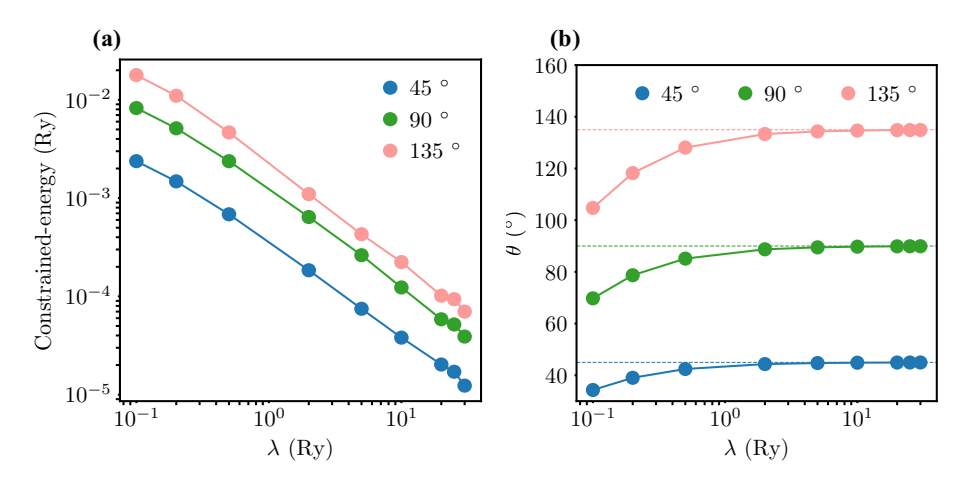


Figure B.1.: Effect of the penalty term (λ) on the properties of noncollinear states of free-standing Fe dimers (Fe-Fe distance 2.0 Å). (a) Constrained-energy (penalty energy), corresponding to different input opening angles between the two Fe spin moments. (b) The self-consistent opening angle between magnetic moments of the two atoms of Fe dimer corresponding to different input opening angles.

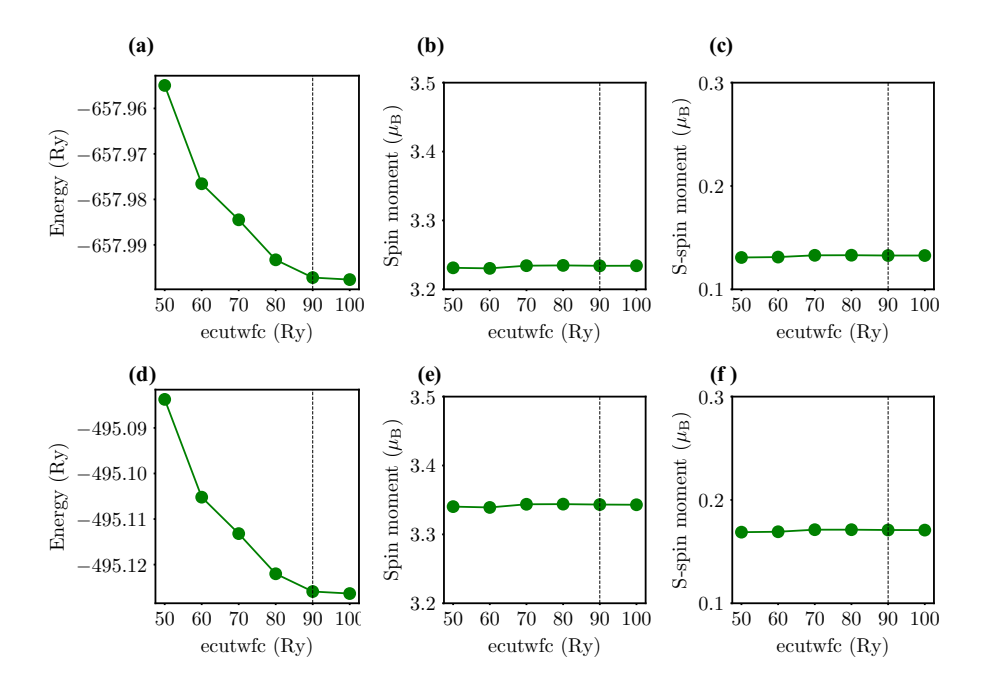


Figure B.2.: Effect of the kinetic energy cutoff for the wavefunctions ('ecutwfc') on the basic properties of free-standing ferromagnetic Fe dimer (Fe-Fe distance 2.0 Å). Results obtained with PAW (a-c) and with USPP (d-f). (a,d) Total energy. (b,e) Fe net spin moment. (c,f) Fe s-orbital projected moment. The cutoff for the density is ecutrho = 8*ecutwfc. Fe1 and Fe2 are equivalent.

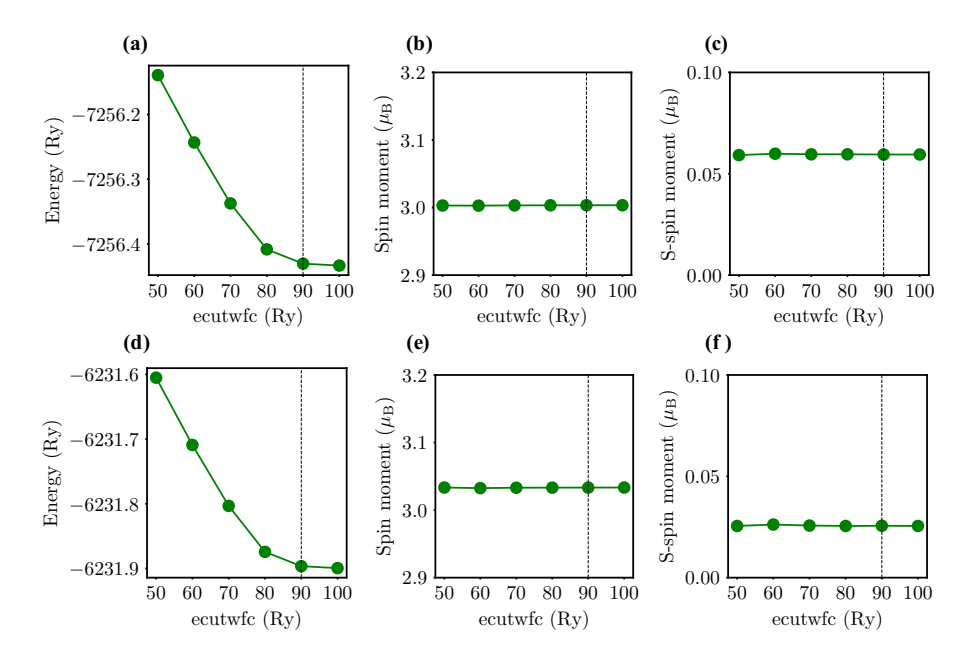


Figure B.3.: Effect of the kinetic energy cutoff for the wavefunctions ('ecutwfc') on the basic properties of ferromagnetic Fe dimers in structure 1 on the MgO bilayer. Results obtained with PAW (a-c) and with USPPs (d-f). (a,d) Total energy. (b,e) Fe net spin moment. (c,f) Fe s-orbital projected moment. Fe1 and Fe2 in structure 1 they are equivalent.

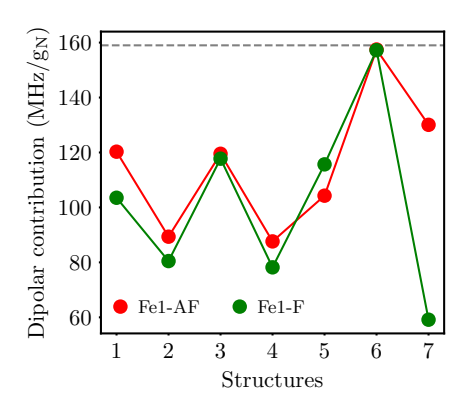


Figure B.4.: Dipolar contributions to the hyperfine interaction for the different Fe dimer structures and magnetic states. The number identifies the Fe dimer structures.

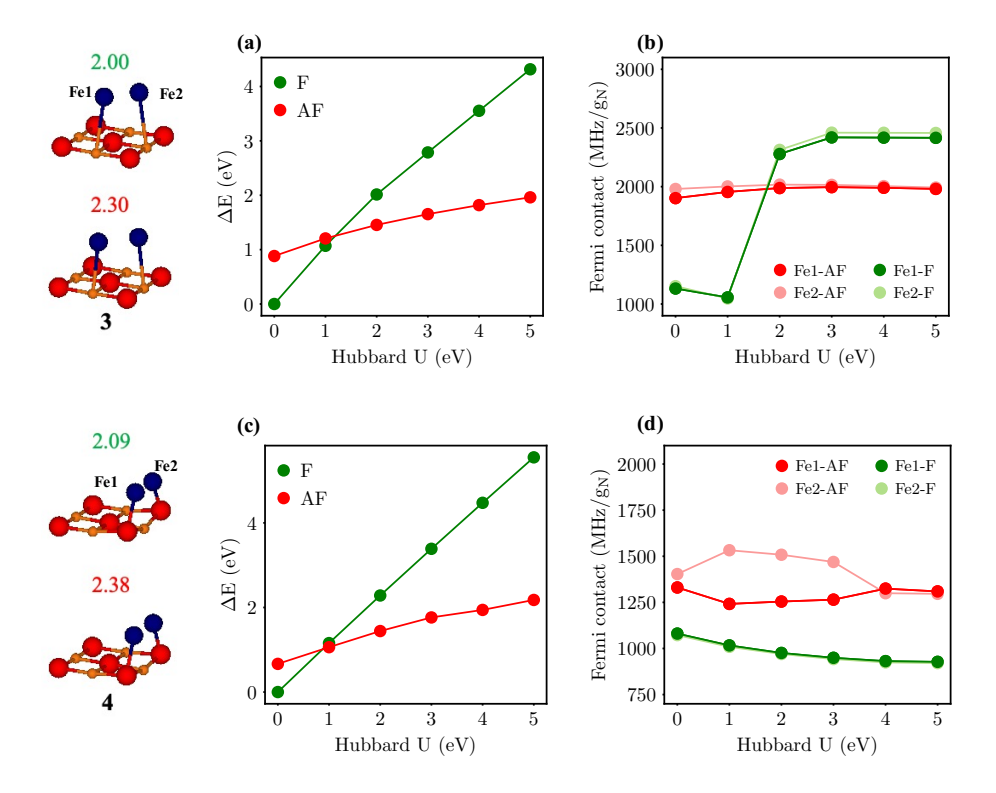


Figure B.5.: Effect of the Hubbard-U correction on the hyperfine fields of Fe dimers on the bilayer of MgO in structure 3 (a and b) and structure 4 (c and d) in the ferromagnetic (F) and antiferromagnetic (AF) states. (a,c) Total energy difference with respect to U=0 eV in the ferromagnetic state. (b,d) Fermi contact contribution to the hyperfine interaction. Fe1 and Fe2 in structure 3 they are equivalent.

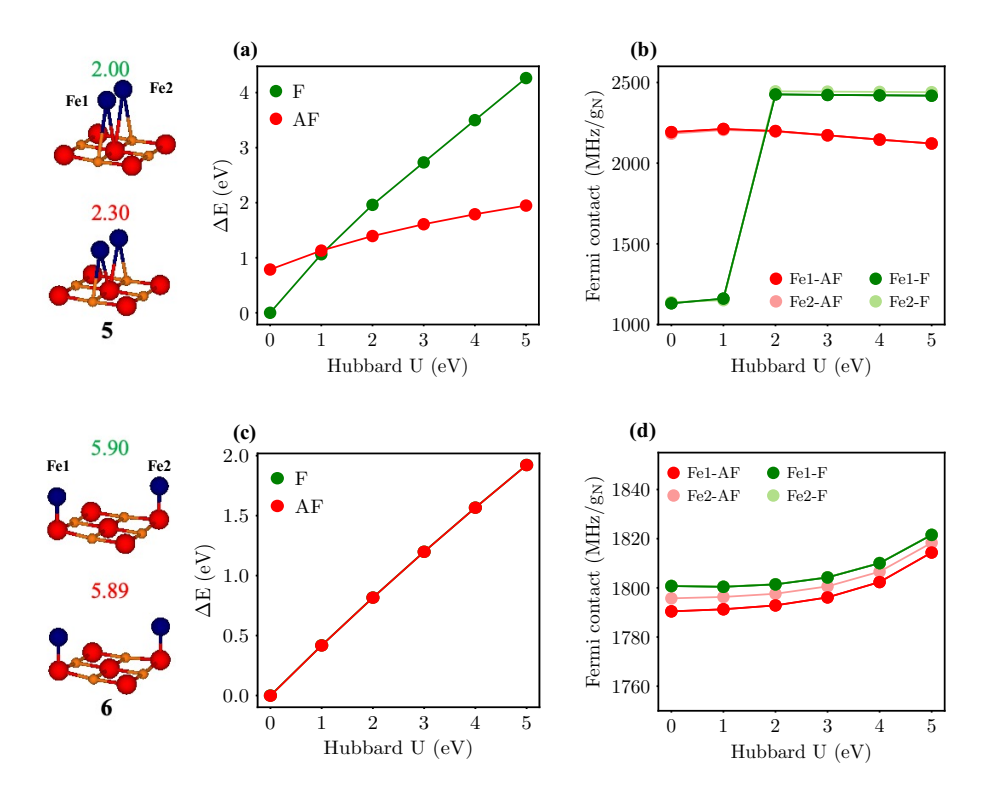


Figure B.6.: Effect of the Hubbard-U correction on the hyperfine fields of Fe dimers on the bilayer of MgO in structure 5 (a and b) and structure 6 (c and d) in the ferromagnetic (F) and antiferromagnetic (AF) states. (a,c) Total energy difference with respect to U=0 eV in the ferromagnetic state. (b,d) Fermi contact contribution to the hyperfine interaction. Fe1 and Fe2 in structures 5 and 6 they are equivalent.

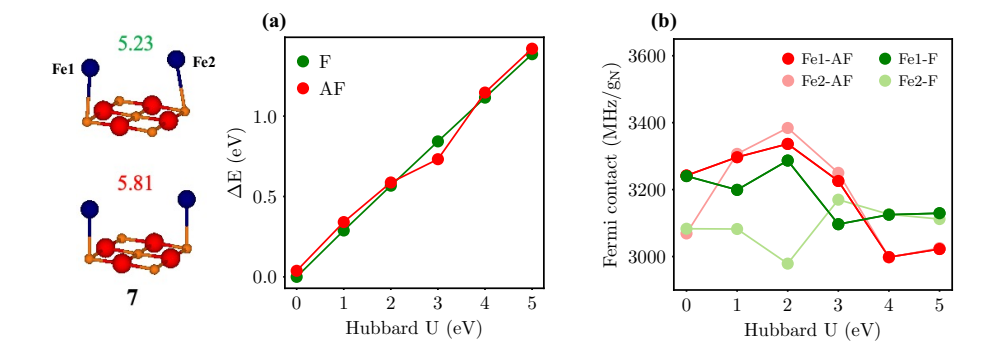


Figure B.7.: Effect of the Hubbard-U correction on the hyperfine fields of Fe dimers on the bilayer of MgO in structure 7 (a and b) in the ferromagnetic (F) and antiferromagnetic (AF) states. (a) Total energy difference with respect to U=0 eV in the ferromagnetic state. (b) Fermi contact contribution to the hyperfine interaction.

C. Appendix-chapter 6

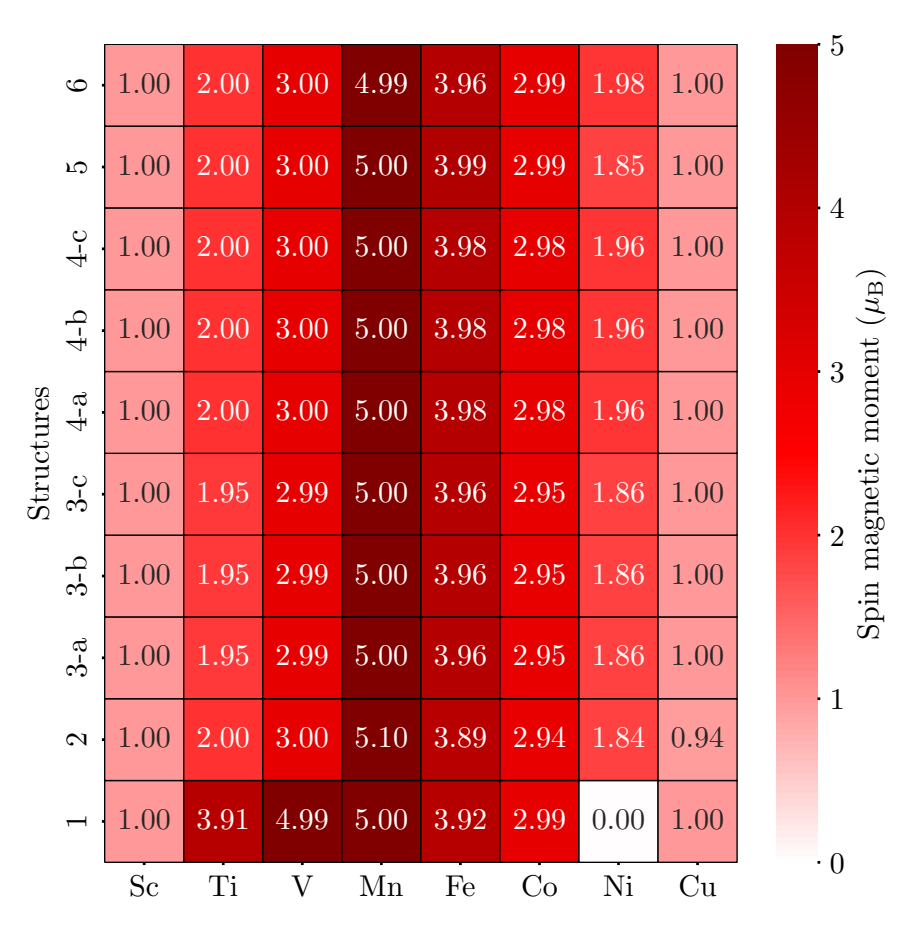


Figure C.1.: Spin magnetic moment of 3d adatom and 3d–O molecules on a bilayer of MgO. The structure number indicates a particular nanostructure with a specific orientation of the magnetization as illustrated in Fig. 6.4. Results obtained by LSDA + SOC + U + USPP calculations.

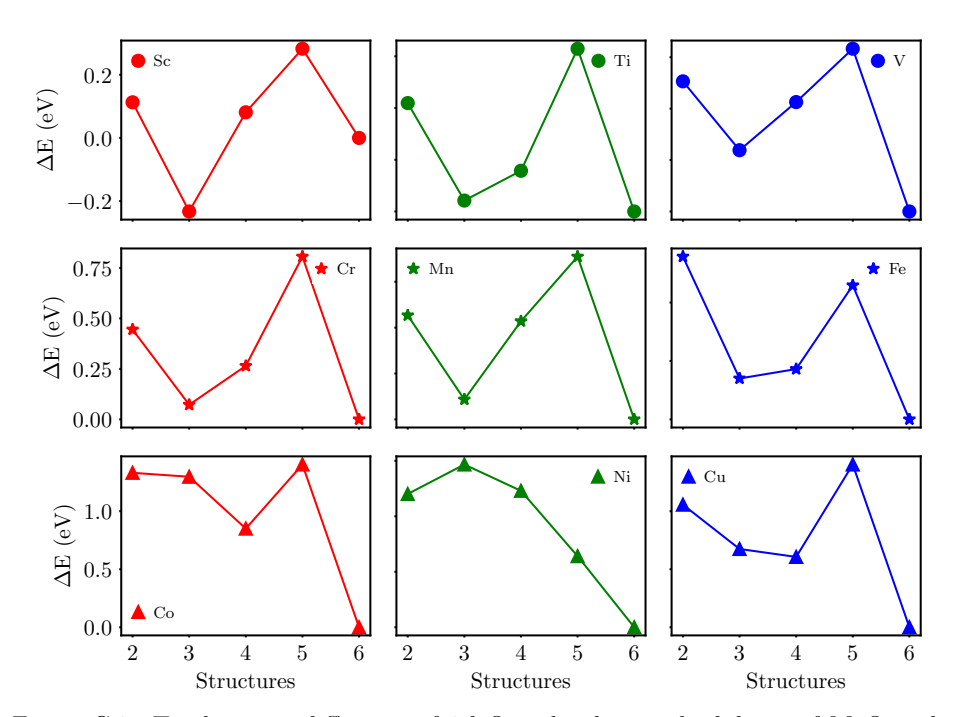


Figure C.2.: Total energy difference of 3d–O molecules on the bilayer of MgO with respect to structure 6, which is the most stable one. The structure number indicates a particular nanostructure illustrated in Fig. 6.1. Results obtained by GGA + U calculations.

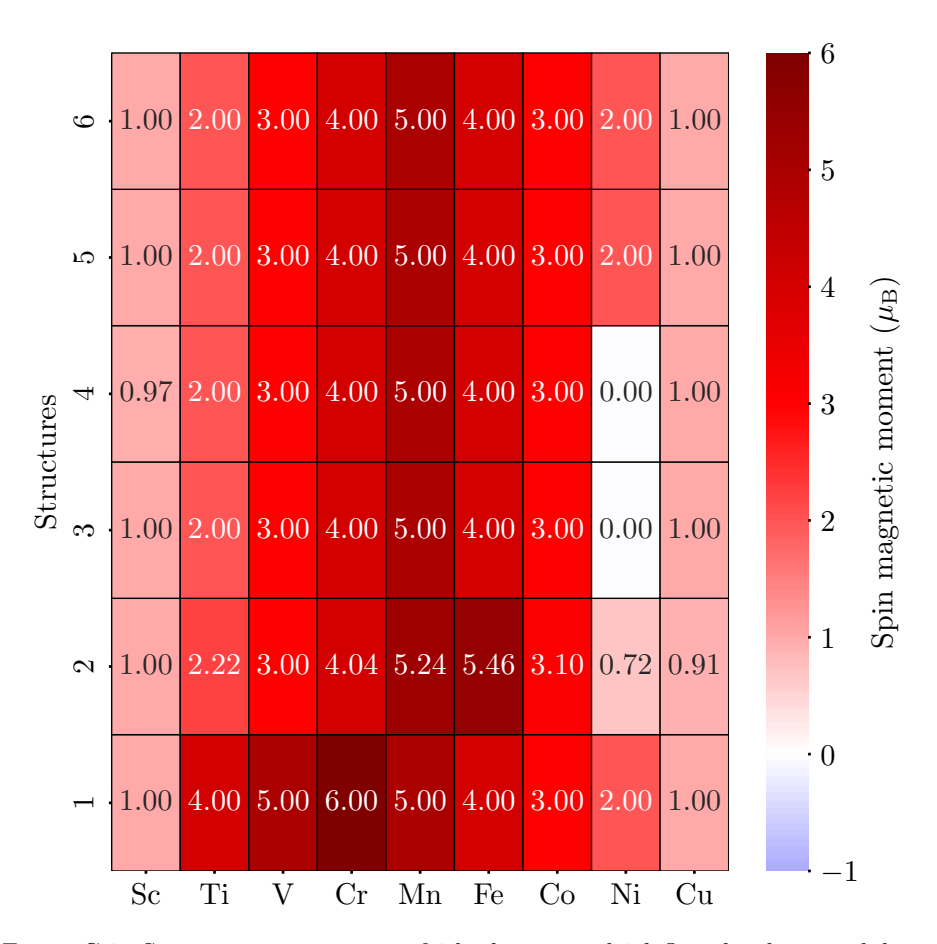


Figure C.3.: Spin magnetic moment of 3d adatoms and 3d–O molecules on a bilayer of MgO. The structure number indicates a particular nanostructure illustrated in Fig. 6.1. Here we use U = 6 eV. Results obtained by GGA + U calculations.

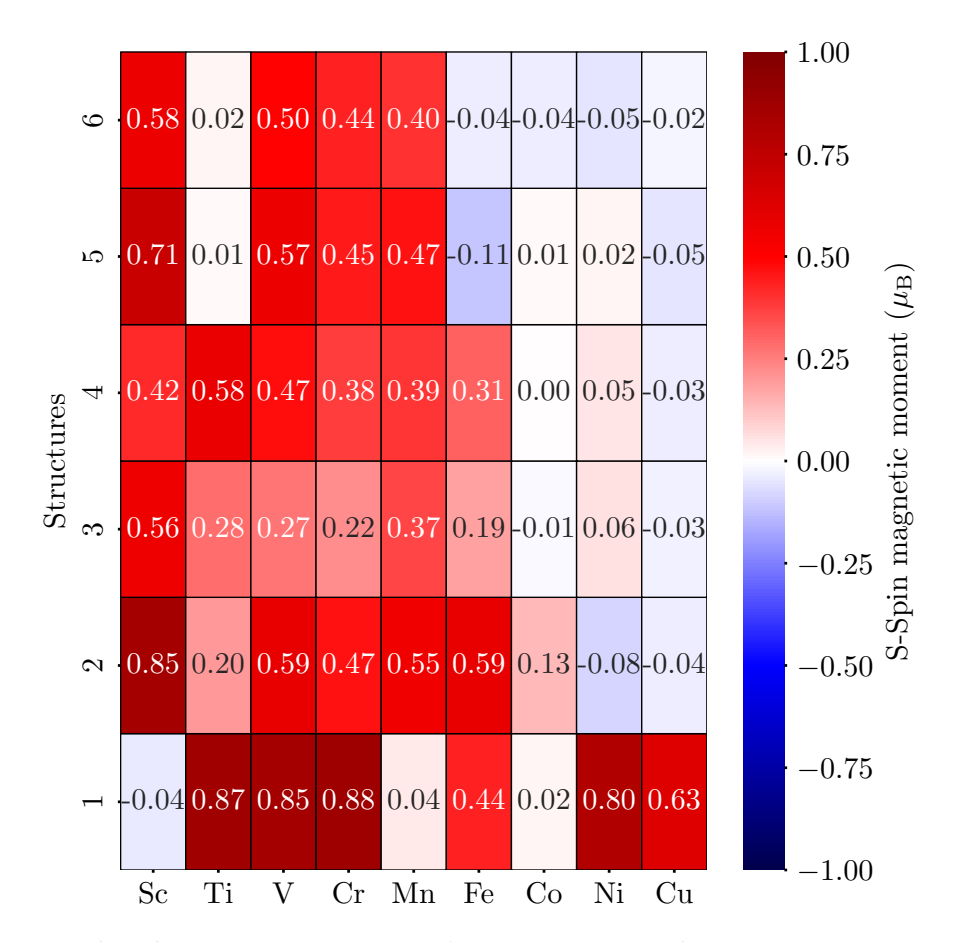


Figure C.4.: S-spin magnetic moment of 3d adatom and 3d–O molecules on a bilayer of MgO. The structure number indicates a particular nanostructure illustrated in Fig. 6.1. Here we used U = 6 eV. Results obtained by GGA + U calculations.

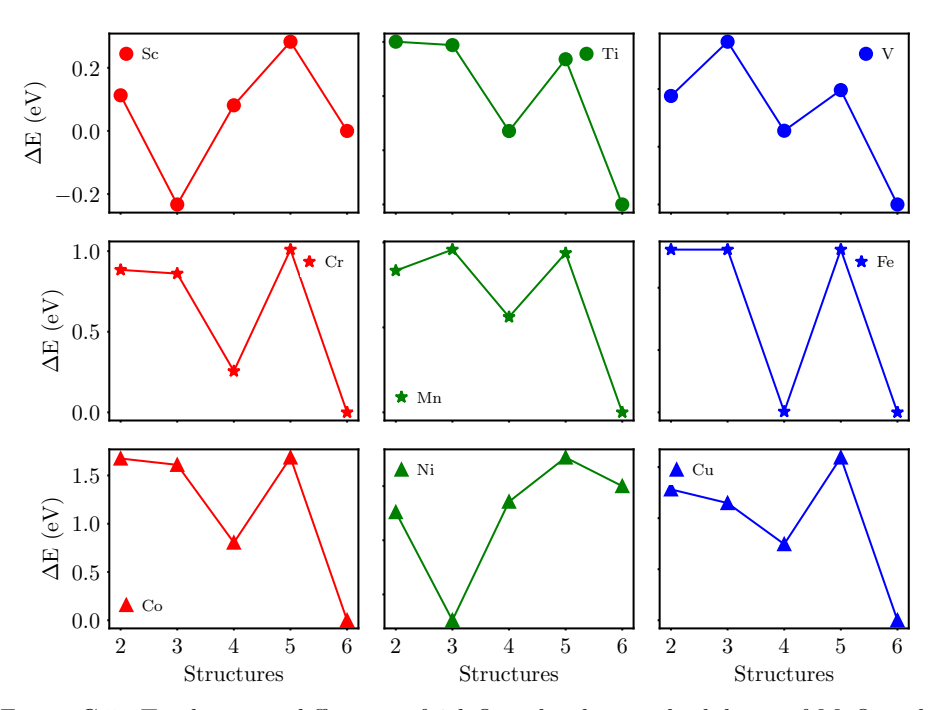


Figure C.5.: Total energy difference of 3d–O molecules on the bilayer of MgO with respect to structure 6, which is the most stable one. The structure number indicates a particular nanostructure illustrated in Fig. 6.1. Results obtained by GGA + PAW calculations.

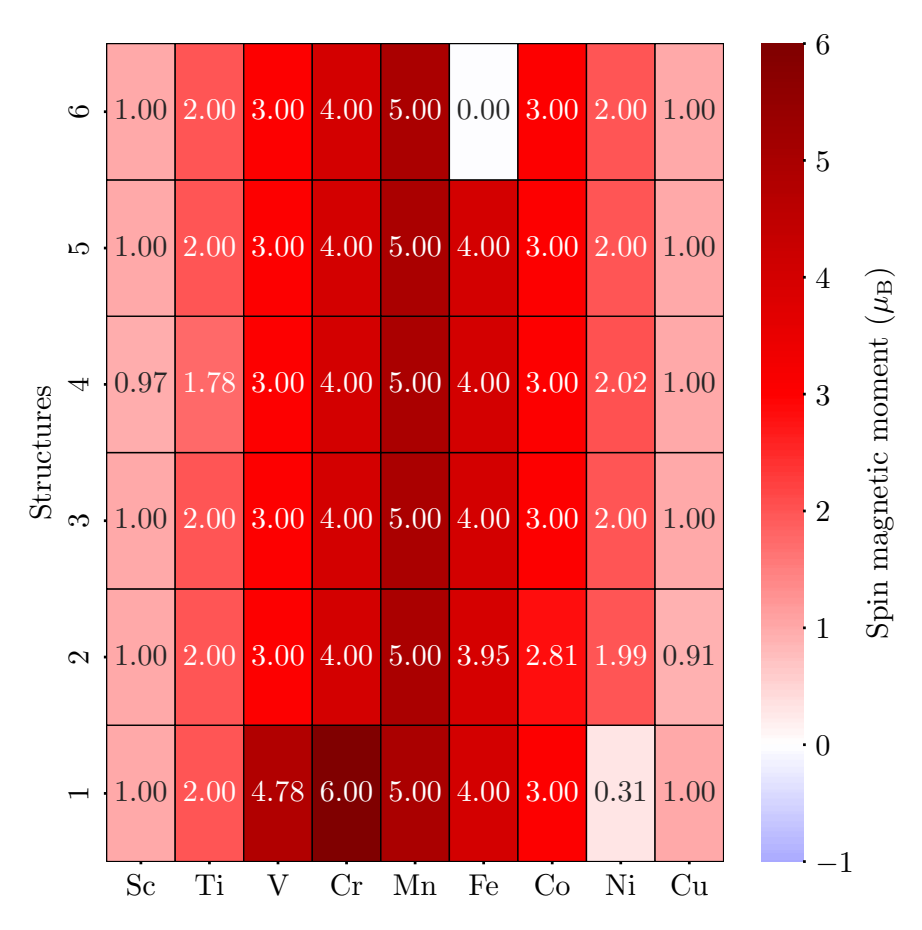


Figure C.6.: Spin magnetic moment of 3d adatom and 3d–O molecules on a bilayer of MgO. The structure number indicates a particular nanostructure illustrated in Fig. 6.1. Results obtained by GGA + PAW calculations.

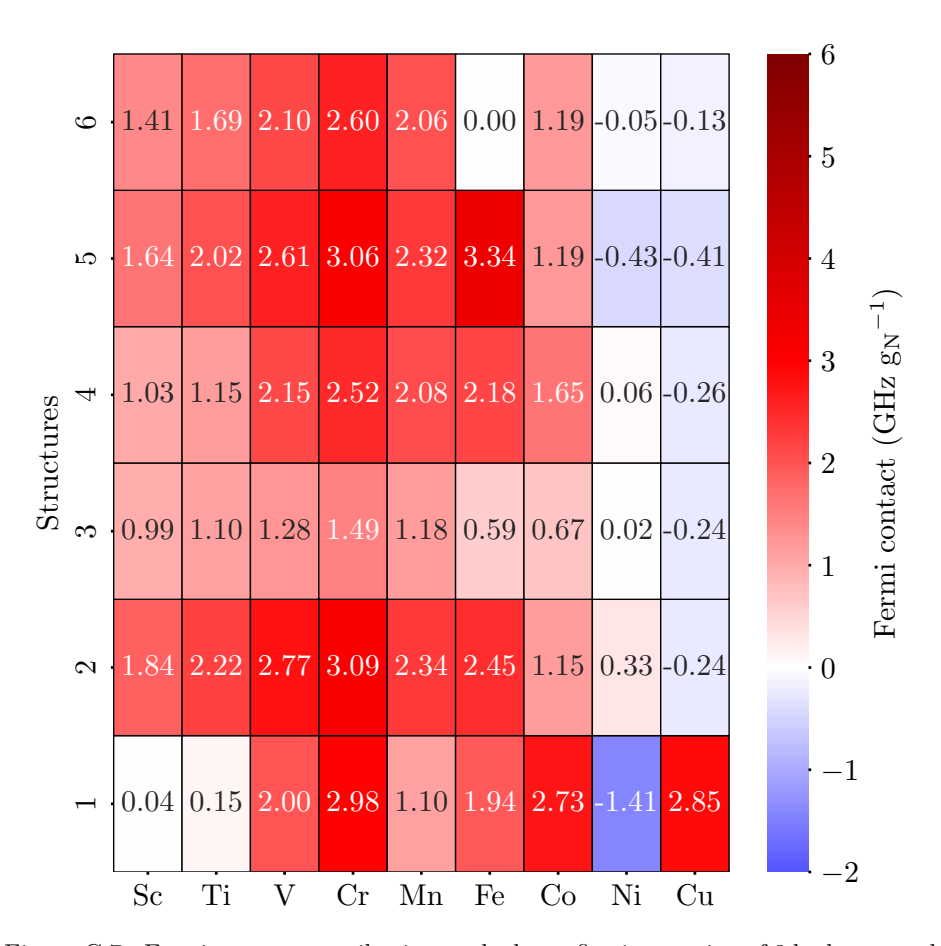


Figure C.7.: Fermi contact contribution to the hyperfine interaction of 3d adatom and 3d–O molecules on a bilayer of MgO. The structure number indicates a particular nanostructure illustrated in Fig. 6.1. Results obtained by GGA + PAW calculations.

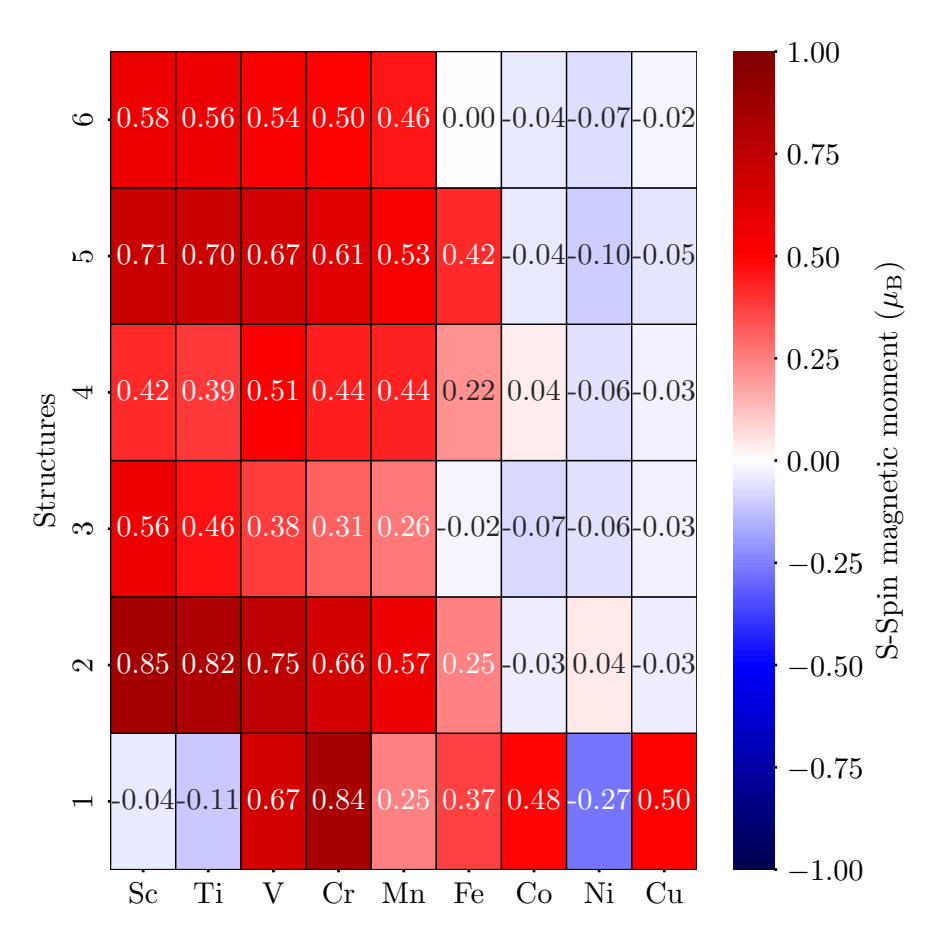


Figure C.8.: S-spin magnetic moment of 3d adatom and 3d–O molecules on a bilayer of MgO. The structure number indicates a particular nanostructure illustrated in Fig. 6.1. Results obtained by GGA + PAW calculations.

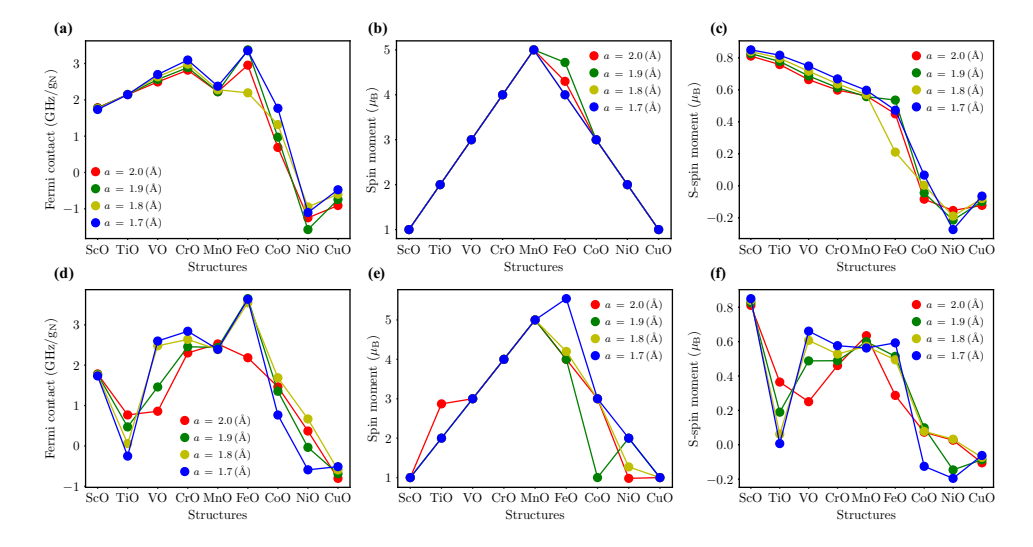


Figure C.9.: Effect of the Hubbard-U correction on the magnetic properties of the isolated 3d–O molecule, for U=0 (a, b, and c) and for U=6 eV (d, e, and f). (a,d) Fermi contact contribution to the hyperfine interaction. (b,e) Spin magnetic moment. (c,f) S-spin magnetic moment. Results obtained by GGA + PAW calculations.

D. Induced magnetization from multiple-scattering expansion

We invoke a multiple scattering formalism based on Green functions describing the propagation of the electron states from atom i to atom j. The theory is similar to the one utilized to explain the spin-mixing magnetoresistance in Refs. [190]–[193] or higher-order magnetic interactions in Refs. [194]–[197]. The spin density of atom i is obtained from the Green function as

$$\mathbf{m}_{i}^{\text{spin}}(\mathbf{r}) = -\frac{1}{\pi} \operatorname{Im} \int dE \ f(E) \operatorname{Tr}_{\text{spin}} \boldsymbol{\sigma} G_{ii}(\mathbf{r}, \mathbf{r}; E) \ . \tag{D.1}$$

Here \mathbf{r} is the electronic position measured with respect to the nuclear position of atom i, f(E) is the Fermi-Dirac distribution, $\boldsymbol{\sigma} = (\sigma_x, \sigma_y, \sigma_z)$ is the vector of Pauli matrices, and $G_{ii}(\mathbf{r}, \mathbf{r}; E)$ is the position-diagonal part of the electronic Green function at energy E. The total spin moment is obtained by integrating the spin density in a suitably-defined region around atom i.

$$\mathbf{m}_i = \int_{\Omega_i} d\mathbf{r} \, \mathbf{m}_i^{\text{spin}}(\mathbf{r}) , \quad \mathbf{S}_i = \frac{\mathbf{m}_i}{|\mathbf{m}_i|} ,$$
 (D.2)

from which we can also define its orientation \mathbf{S}_i . The Fermi contact and the dipolar contributions to the hyperfine interaction are defined in terms of the spin density in the vicinity of the nucleus, and we now seek to establish how this quantity is modified by changes in the magnetic state of nearby atoms. The Kohn-Sham hamiltonian can be written as

$$\mathcal{H} = \mathcal{H}^{0} + \sum_{i} B_{i}^{xc}(\mathbf{r}) \mathbf{S}_{i} \cdot \boldsymbol{\sigma} = \mathcal{H}^{0} + \mathcal{H}^{mag} , \qquad (D.3)$$

where \mathcal{H}^0 collects contributions which do not depend on the spin orientations, and the exchange-correlation magnetic field $B_i^{\text{xc}}(\mathbf{r})$ for atom i is assumed to point along the orientation of the respective total spin moment \mathbf{S}_i . Here the spin-orbit interaction is neglected for simplicity.

As shown in e.g. Ref. [194], we can make use of the Dyson equation to also separate the Green function as

$$G = G^{0} + G^{0} \mathcal{H}^{\text{mag}} G^{0} + G^{0} \mathcal{H}^{\text{mag}} G^{0} \mathcal{H}^{\text{mag}} G^{0} + \dots$$
 (D.4)

with the reference Green function $G^0 = (E - \mathcal{H}^0)^{-1}$. Keeping only the first magnetic term and using the definition for the spin density, Eq. D.1, we find

$$\mathbf{m}_{i}^{\text{spin}}(\mathbf{r}) = -\frac{1}{\pi} \operatorname{Im} \int dE \ f(E) \sum_{i} \int d\mathbf{r}' \ G_{ij}^{0}(\mathbf{r}, \mathbf{r}'; E) \ B_{j}^{\text{xc}}(\mathbf{r}') \ \mathbf{S}_{j} \ G_{ji}^{0}(\mathbf{r}', \mathbf{r}; E) + \dots \ (D.5)$$

Projecting on the orientation of the spin moment of atom i and integrating out the spatial dependence in combination with the projector $\mathcal{P}_i(\mathbf{r})$ defining the hyperfine interaction (this could be to extract the Fermi contact or the dipolar contributions) we find

 $\int d\mathbf{r} \, \mathcal{P}_i(\mathbf{r}) \, \mathbf{m}_i^{\text{spin}}(\mathbf{r}) \cdot \mathbf{S}_i = A_i + \sum_{j \neq i} A_{ij} \, \mathbf{S}_i \cdot \mathbf{S}_j . \tag{D.6}$

Although this result was obtained using only the lowest-order contribution, taking higher-order terms into account will only modify the definitions of the coefficients but not the dependence on the relative orientations of the spin moments.

E. List of scientific contributions

Journal articles related to this thesis

- [1] S. Shehada, M. dos Santos Dias, M. Abusaa, and S. Lounis, "Interplay of magnetic states and hyperfine fields of iron dimers on mgo(001)," *Journal of Physics: Condensed Matter*, vol. 34, no. 38, pp. 1–12, 2022.
- [2] S. Shehada, M. dos Santos Dias, F. S. M. Guimarães, M. Abusaa, and S. Lounis, "Trends in the hyperfine interactions of magnetic adatoms on thin insulating layers," npj Computational Materials, vol. 7, no. 1, pp. 1–10, 2021.

Journal articles unrelated to this thesis

- H. K. Khanfar, A. Qasrawi, and S. R. Shehada, "Negative capacitance effect in ag/α-in2se3/cds/cdse/c dual band stop filters," *Journal of Electronic Materials*, vol. 48, no. 1, pp. 244–251, 2019.
- [2] A. Qasrawi and S. R. Shehada, "Dielectric dispersion in inse/cds bilayers," *Physica E: Low-dimensional Systems and Nanostructures*, vol. 103, pp. 151–155, 2018.
- [3] M. AbuSaa, A. Qasrawi, and S. R. Shehada, "Dielectric and optoelectronic properties of inse/cds/cdse heterojunctions," *Journal of Electronic Materials*, vol. 47, no. 11, pp. 6583–6590, 2018.

Invited talk

[1] S. Shehada, M. dos Santos Dias, F. S. M. Guimarães, M. Abusaa, and S. Lounis, "Hyperfine fields of magnetic adatoms on ultrathin insulating films," in *Frühjahrstagung der Deutschen Physikalischen Gesellschaft*, DPG Spring Meeting, Germany, Mar. 2021.

Contributed talks

[1] S. Shehada, M. Abusaa, and H. K. Khanfar, "Fabrication and characterization of wide band photo-conductor array," in *The Second Palestinian International Graduate Conference on Natural, Medical and Health Sciences and Humanities*, An-Najah National University, Palestine, Apr. 2017.

- [2] S. Shehada, M. Abusaa, and H. K. Khanfar, "Fabrication and characterization of wide band photo-conductor array," in Sixth Palestinian Conference on Modern Trends in Mathematics and Physics, Palestine Technical University-Kadoorie, Tulkarm-Palestine, Aug. 2018.
- [3] S. Shehada, M. dos Santos Dias, F. S. M. Guimarães, M. Abusaa, and S. Lounis, "Hyperfine fields of magnetic adatoms on mgo/ag(001)," in 4th Palestinian German Science Bridge Cooperation Workshop, Ramallah-Palestine, Apr. 2019.
- [4] S. Shehada, M. dos Santos Dias, F. S. M. Guimarães, M. Abusaa, and S. Lounis, "Hyperfine fields of magnetic adatoms on ultrathin insulating films," in *Palestinian German Science Bridge Fellows Competition*, Ramallah-Palestine, Jul. 2020.
- [5] S. Shehada, M. dos Santos Dias, M. Abusaa, and S. Lounis, "Interplay of magnetic states and hyperfine fields of iron dimers on mgo(001)," in Frühjahrstagung der Deutschen Physikalischen Gesellschaft der Sektion Kondensierte Materie, SKM21, Germany, Sep. 2021.
- [6] S. Shehada, M. dos Santos Dias, F. S. M. Guimarães, M. Abusaa, and S. Lounis, "Hyperfine fields of magnetic adatoms on ultrathin insulating films," in 3rd International Conference on Hyperfine Interactions and their Applications, HYPERFINE-2021, Brasov-Romania, Sep. 2021.
- [7] S. Shehada, M. dos Santos Dias, F. S. M. Guimarães, M. Abusaa, and S. Lounis, "Hyperfine fields of magnetic adatoms on ultrathin insulating films," in *Palestinian-German Science bridge (PGSB) Seminar*, Jülich, Germany, Feb. 2022.
- [8] S. Shehada, M. dos Santos Dias, F. S. M. Guimarães, M. Abusaa, and S. Lounis, "Hyperfine fields of magnetic impurities in bulk ag, on ag(001) and on mgo/ag(001)," in *Quantum Theory of Materials seminar*, PGI/IAS, Jülich, Germany, May 2019.
- [9] S. Shehada, M. dos Santos Dias, M. Abusaa, and S. Lounis, "Interplay of magnetic states and hyperfine fields of iron dimers on mgo(001)," in *The 24th International Colloquium on Magnetic Films and Surfaces*, ICMFS-2022, Okinawa-Japan, Jul. 2022.
- [10] S. Shehada, M. dos Santos Dias, M. Abusaa, and S. Lounis, "Interplay of magnetic states and hyperfine fields of iron dimers on mgo(001)," in *The Joint European Magnetic Symposia*, JEMS-2022, Warsaw-Poland, Jul. 2022.
- [11] S. Shehada, M. dos Santos Dias, M. Abusaa, and S. Lounis, "Interplay of magnetic states and hyperfine fields of iron dimers on mgo(001)," in *Palestinian Conference on Modern Trends in Mathematics and Physics VII*, Birzeit University-Palestine, Aug. 2022.

[12] S. Shehada, M. dos Santos Dias, M. Abusaa, and S. Lounis, "Interplay of magnetic states and hyperfine fields of iron dimers on mgo(001)," in Frühjahrstagung der Deutschen Physikalischen Gesellschaft, DPG Spring Meeting, Germany, Sep. 2022.

Posters

- [1] S. Shehada, M. dos Santos Dias, F. S. M. Guimarães, M. Abusaa, and S. Lounis, Hyperfine fields of magnetic adatoms on ultrathin insulating films. Germany: Frühjahrstagung der Deutschen Physikalischen Gesellschaft, Mar. 2021.
- [2] S. Shehada, M. dos Santos Dias, F. S. M. Guimarães, M. Abusaa, and S. Lounis, Hyperfine fields of magnetic adatoms on MgO/Ag(001). Ramallah-Palestine, Apr. 2019.
- [3] S. Shehada, M. dos Santos Dias, M. Abusaa, and S. Lounis, *Interplay of magnetic states and hyperfine fields of iron dimers on MgO(001)*. Lausanne-Switzerland: *PSI-K Conference*, Aug. 2022.
- [4] S. Shehada, M. dos Santos Dias, F. S. M. Guimarães, M. Abusaa, and S. Lounis, Hyperfine fields of magnetic adatoms on MgO/Ag(001). Germany: Frühjahrstagung der Deutschen Physikalischen Gesellschaft, Apr. 2019.
- [5] S. Shehada, M. Abusaa, and H. K. Khanfar, Exploring Demarcation levels in Laser excited photodiode arrays. Arab American University-Palestine: Fifth Palestinian Conference on Modern trends in Mathematics and Physics, Aug. 2016.

References

- [1] M. T. Mądzik, S. Asaad, A. Youssry, et al., "Precision tomography of a three-qubit donor quantum processor in silicon," Nature, vol. 601, no. 7644, pp. 348–353, 2022 (cit. on pp. 1, 2, 25).
- [2] A. Yang, M. Steger, T. Sekiguchi, et al., "Simultaneous subsecond hyperpolarization of the nuclear and electron spins of phosphorus in silicon by optical pumping of exciton transitions," Phys. Rev. Lett., vol. 102, p. 257401, 25 2009 (cit. on pp. 1, 2, 25).
- [3] B. B. Blinov, D. Leibfried, C. Monroe, and D. J. Wineland, "Quantum computing with trapped ion hyperfine qubits," *Quantum Inf. Process.*, vol. 3, no. 1-5, pp. 45–59, 2004 (cit. on pp. 1, 2, 25).
- [4] C. J. Ballance, T. P. Harty, N. M. Linke, M. A. Sepiol, and D. M. Lucas, "High-fidelity quantum logic gates using trapped-ion hyperfine qubits," *Phys. Rev. Lett.*, vol. 117, p. 060 504, 6 2016 (cit. on pp. 1, 2, 25).
- [5] S. Thiele, F. Balestro, R. Ballou, S. Klyatskaya, M. Ruben, and W. Wernsdorfer, "Electrically driven nuclear spin resonance in single-molecule magnets," *Science*, vol. 344, no. 6188, pp. 1135–1138, 2014, ISSN: 0036-8075 (cit. on pp. 1, 2, 25).
- [6] R. Vincent, S. Klyatskaya, M. Ruben, W. Wernsdorfer, and F. Balestro, "Electronic read-out of a single nuclear spin using a molecular spin transistor," Nature, vol. 488, no. 7411, pp. 357–360, 2012 (cit. on pp. 1, 2, 25).
- [7] F. D. Natterer, K. Yang, W. Paul, et al., "Reading and writing single-atom magnets," Nature, vol. 543, no. 7644, pp. 226–228, 2017 (cit. on pp. 1, 2, 25, 59, 75).
- [8] I. G. Rau, S. Baumann, S. Rusponi, et al., "Reaching the magnetic anisotropy limit of a 3d metal atom," Science, vol. 344, no. 6187, pp. 988–992, 2014, ISSN: 0036-8075 (cit. on pp. 1, 2, 4, 25, 29, 58, 59, 61, 65).
- [9] D.-J. Choi, N. Lorente, J. Wiebe, K. von Bergmann, A. F. Otte, and A. J. Heinrich, "Colloquium: Atomic spin chains on surfaces," Rev. Mod. Phys., vol. 91, p. 041 001, 4 2019 (cit. on p. 1).
- [10] Y. Chen, Y. Bae, and A. J. Heinrich, "Harnessing the quantum behavior of spins on surfaces," *Advanced Materials*, p. 2107534, 2022 (cit. on p. 1).
- [11] Y. Wang, Y. Chen, H. T. Bui, et al., "An electron-spin qubit platform assembled atom-by-atom on a surface," arXiv preprint arXiv:2108.09880, 2021 (cit. on p. 1).
- [12] G. Binnig, H. Rohrer, C. Gerber, and E. Weibel, "Surface studies by scanning tunneling microscopy," *Physical review letters*, vol. 49, no. 1, p. 57, 1982 (cit. on p. 1).

- [13] G. Binnig and H. Rohrer, "Scanning tunneling microscopy," Surface science, vol. 126, no. 1-3, pp. 236–244, 1983 (cit. on p. 1).
- [14] G. Binnig and H. Rohrer, "Scanning tunneling microscopy—from birth to adolescence," reviews of modern physics, vol. 59, no. 3, p. 615, 1987 (cit. on p. 1).
- [15] R. Wiesendanger, "Spin mapping at the nanoscale and atomic scale," Rev. Mod. Phys., vol. 81, no. 4, p. 1495, 2009 (cit. on p. 1).
- [16] F. Delgado and J. Fernández-Rossier, "Spin decoherence of magnetic atoms on surfaces," *Prog. Surf. Sci.*, vol. 92, no. 1, pp. 40–82, 2017, ISSN: 0079-6816 (cit. on p. 2).
- [17] J. Ibanez-Azpiroz, M. dos Santos Dias, S. Blügel, and S. Lounis, "Zero-point spin-fluctuations of single adatoms," *Nano letters*, vol. 16, no. 7, pp. 4305–4311, 2016 (cit. on p. 2).
- [18] J. Ibañez-Azpiroz, M. d. S. Dias, S. Blügel, and S. Lounis, "Longitudinal and transverse spin relaxation times of magnetic single adatoms: An ab initio analysis," *Phys. Rev. B*, vol. 96, p. 144410, 14 2017 (cit. on p. 2).
- [19] J. Ibañez-Azpiroz, M. dos Santos Dias, S. Blügel, and S. Lounis, "Spin-fluctuation and spin-relaxation effects of single adatoms from first principles," *Journal of Physics: Condensed Matter*, vol. 30, no. 34, p. 343 002, 2018 (cit. on p. 2).
- [20] J. Bouaziz, J. Ibañez-Azpiroz, F. S. Guimarães, and S. Lounis, "Zero-point magnetic exchange interactions," *Physical review research*, vol. 2, no. 4, p. 043 357, 2020 (cit. on p. 2).
- [21] H. Garai-Marin, M. dos Santos Dias, S. Lounis, J. Ibañez-Azpiroz, and A. Eiguren, "Microscopic theory of spin relaxation of a single fe adatom coupled to substrate vibrations," *Physical Review B*, vol. 107, no. 14, p. 144417, 2023 (cit. on pp. 2, 75).
- [22] C. F. Hirjibehedin, C. P. Lutz, and A. J. Heinrich, "Spin coupling in engineered atomic structures," *Science*, vol. 312, no. 5776, pp. 1021–1024, 2006 (cit. on pp. 2, 25, 37).
- [23] C. F. Hirjibehedin, C.-Y. Lin, A. F. Otte, et al., "Large magnetic anisotropy of a single atomic spin embedded in a surface molecular network," *Science*, vol. 317, no. 5842, pp. 1199–1203, 2007, ISSN: 0036-8075 (cit. on pp. 2, 25, 37, 58).
- [24] A. F. Otte, M. Ternes, K. Von Bergmann, et al., "The role of magnetic anisotropy in the kondo effect," Nat. Phys., vol. 4, no. 11, pp. 847–850, 2008 (cit. on pp. 2, 25, 37).
- [25] S. Loth, K. von Bergmann, M. Ternes, A. F. Otte, C. P. Lutz, and A. J. Heinrich, "Controlling the state of quantum spins with electric currents," *Nat. Phys.*, vol. 6, no. 5, pp. 340–344, 2010 (cit. on pp. 2, 25, 37).

- [26] S. Loth, M. Etzkorn, C. P. Lutz, D. M. Eigler, and A. J. Heinrich, "Measurement of fast electron spin relaxation times with atomic resolution," *Science*, vol. 329, no. 5999, pp. 1628–1630, 2010, ISSN: 0036-8075 (cit. on pp. 2, 25, 37).
- [27] S. Loth, S. Baumann, C. P. Lutz, D. M. Eigler, and A. J. Heinrich, "Bistability in atomic-scale antiferromagnets," *Science*, vol. 335, no. 6065, pp. 196–199, 2012, ISSN: 0036-8075 (cit. on pp. 2, 25, 37, 58).
- [28] F. D. Natterer, F. ç. Patthey, and H. Brune, "Ring state for single transition metal atoms on boron nitride on rh(111)," *Phys. Rev. Lett.*, vol. 109, p. 066 101, 6 2012 (cit. on pp. 2, 25, 37).
- [29] Z. Li, H.-Y. T. Chen, K. Schouteden, et al., "Self-doping of ultrathin insulating films by transition metal atoms," Phys. Rev. Lett., vol. 112, p. 026 102, 2 2014 (cit. on pp. 2, 35).
- [30] P. Jacobson, T. Herden, M. Muenks, et al., "Quantum engineering of spin and anisotropy in magnetic molecular junctions," Nat. Commun., vol. 6, no. 1, pp. 1–6, 2015 (cit. on pp. 2, 25, 37).
- [31] I. Gallardo, A. Arnau, F. Delgado, et al., "Large effect of metal substrate on magnetic anisotropy of co on hexagonal boron nitride," New J. Phys., vol. 21, no. 7, p. 073 053, 2019 (cit. on pp. 2, 25, 37).
- [32] R. Rejali, D. Coffey, J. Gobeil, J. W. González, F. Delgado, and A. F. Otte, "Complete reversal of the atomic unquenched orbital moment by a single electron," *npj Quantum Mater.*, vol. 5, p. 60, 2020, ISSN: 2397-4648 (cit. on pp. 2, 25, 37).
- [33] S. Baumann, W. Paul, T. Choi, C. P. Lutz, A. Ardavan, and A. J. Heinrich, "Electron paramagnetic resonance of individual atoms on a surface," *Science*, vol. 350, no. 6259, pp. 417–420, 2015, ISSN: 0036-8075 (cit. on pp. 2, 25, 29, 59).
- [34] S. Baumann, F. Donati, S. Stepanow, et al., "Origin of perpendicular magnetic anisotropy and large orbital moment in fe atoms on mgo," Phys. Rev. Lett., vol. 115, p. 237 202, 23 2015 (cit. on pp. 2, 25, 29, 56, 58, 59).
- [35] W. Paul, K. Yang, S. Baumann, et al., "Control of the millisecond spin lifetime of an electrically probed atom," Nat. Phys., vol. 13, pp. 403–407, 2017, ISSN: 1745-2473 (cit. on pp. 2, 25, 29, 59).
- [36] K. Yang, Y. Bae, W. Paul, et al., "Engineering the eigenstates of coupled spin-1/2 atoms on a surface," Phys. Rev. Lett., vol. 119, p. 227 206, 22 2017 (cit. on pp. 2, 25, 29, 59).
- [37] F. Donati, S. Rusponi, S. Stepanow, et al., "Magnetic remanence in single atoms," Science, vol. 352, no. 6283, pp. 318–321, 2016, ISSN: 0036-8075 (cit. on pp. 2, 25, 59, 75).

- [38] P. R. Forrester, F. Patthey, E. Fernandes, D. P. Sblendorio, H. Brune, and F. D. Natterer, "Quantum state manipulation of single atom magnets using the hyperfine interaction," *Phys. Rev. B*, vol. 100, p. 180 405, 18 2019 (cit. on pp. 2, 25, 59).
- [39] T. Choi, W. Paul, S. Rolf-Pissarczyk, et al., "Atomic-scale sensing of the magnetic dipolar field from single atoms," *Nature nanotechnology*, vol. 12, no. 5, pp. 420–424, 2017 (cit. on pp. 2, 25, 52, 59).
- [40] K. Yang, S.-H. Phark, Y. Bae, et al., "Probing resonating valence bond states in artificial quantum magnets," *Nature communications*, vol. 12, no. 1, pp. 1–7, 2021 (cit. on pp. 2, 25, 52, 59).
- [41] P. Willke, K. Yang, Y. Bae, A. J. Heinrich, and C. P. Lutz, "Magnetic resonance imaging of single atoms on a surface," *Nat. Phys.*, vol. 15, no. 10, pp. 1005–1010, 2019 (cit. on pp. 2, 25, 59).
- [42] P. Willke, Y. Bae, K. Yang, et al., "Hyperfine interaction of individual atoms on a surface," Science, vol. 362, no. 6412, pp. 336–339, 2018, ISSN: 0036-8075 (cit. on pp. 2, 3, 25, 29, 31, 32, 35, 45, 52, 55, 59).
- [43] K. Yang, P. Willke, Y. Bae, et al., "Electrically controlled nuclear polarization of individual atoms," Nat. Nanotechnol., vol. 13, no. 12, pp. 1120–1125, 2018 (cit. on pp. 2, 25, 29, 31, 32, 59).
- [44] J. Kim, K. Noh, Y. Chen, et al., "Anisotropic hyperfine interaction of surface-adsorbed single atoms," Nano Letters, vol. 22, no. 23, pp. 9766–9772, 2022 (cit. on pp. 2, 25, 29, 35, 59).
- [45] L. Farinacci, L. M. Veldman, P. Willke, and S. Otte, "Experimental determination of a single atom ground state orbital through hyperfine anisotropy," *Nano Letters*, vol. 22, no. 21, pp. 8470–8474, 2022 (cit. on pp. 2, 25, 29, 35, 59).
- [46] X. Zhang, C. Wolf, Y. Wang, et al., "Electron spin resonance of single iron phthalocyanine molecules and role of their non-localized spins in magnetic interactions," *Nature Chemistry*, vol. 14, no. 1, pp. 59–65, 2022 (cit. on pp. 2, 25, 59).
- [47] P. Willke, T. Bilgeri, X. Zhang, et al., "Coherent spin control of single molecules on a surface," ACS nano, vol. 15, no. 11, pp. 17959–17965, 2021 (cit. on pp. 2, 25, 59).
- [48] J. Kim, W.-j. Jang, T. H. Bui, et al., "Spin resonance amplitude and frequency of a single atom on a surface in a vector magnetic field," *Physical Review B*, vol. 104, no. 17, p. 174 408, 2021 (cit. on pp. 2, 25, 35, 59).
- [49] M. Steinbrecher, W. M. J. van Weerdenburg, E. F. Walraven, et al., "Quantifying the interplay between fine structure and geometry of an individual molecule on a surface," *Phys. Rev. B*, vol. 103, p. 155405, 152021 (cit. on pp. 2, 25, 35, 59).

- [50] A. Singha, D. Sostina, C. Wolf, et al., "Mapping orbital-resolved magnetism in single lanthanide atoms," ACS nano, vol. 15, no. 10, pp. 16162–16171, 2021 (cit. on pp. 2, 25, 59).
- [51] A. Singha, P. Willke, T. Bilgeri, et al., "Engineering atomic-scale magnetic fields by dysprosium single atom magnets," Nature Communications, vol. 12, no. 1, pp. 1–6, 2021 (cit. on pp. 2, 25, 59, 75).
- [52] K. Yang, W. Paul, S.-H. Phark, et al., "Coherent spin manipulation of individual atoms on a surface," Science, vol. 366, no. 6464, pp. 509–512, 2019, ISSN: 0036-8075 (cit. on pp. 2, 25, 29, 59).
- [53] S. Kovarik, R. Robles, R. Schlitz, et al., "Electron paramagnetic resonance of alkali metal atoms and dimers on ultrathin mgo," Nano Letters, 2022 (cit. on pp. 2, 25, 59).
- [54] A. A. Khajetoorians, S. Lounis, B. Chilian, et al., "Itinerant nature of atom-magnetization excitation by tunneling electrons," Phys. Rev. Lett., vol. 106, no. 3, p. 037 205, 2011 (cit. on p. 2).
- [55] A. A. Khajetoorians, J. Wiebe, B. Chilian, and R. Wiesendanger, "Realizing all-spin-based logic operations atom by atom," *Science*, vol. 332, no. 6033, pp. 1062–1064, 2011 (cit. on pp. 2, 58).
- [56] A. A. Khajetoorians, J. Wiebe, B. Chilian, S. Lounis, S. Blügel, and R. Wiesendanger, "Atom-by-atom engineering and magnetometry of tailored nanomagnets," *Nat. Phys.*, vol. 8, no. 6, pp. 497–503, 2012 (cit. on p. 2).
- [57] A. A. Khajetoorians, B. Baxevanis, C. Hübner, et al., "Current-driven spin dynamics of artificially constructed quantum magnets," *Science*, vol. 339, no. 6115, pp. 55–59, 2013, ISSN: 0036-8075 (cit. on pp. 2, 58).
- [58] J. Hermenau, J. Ibañez-Azpiroz, C. Hübner, et al., "A gateway towards non-collinear spin processing using three-atom magnets with strong substrate coupling," Nat. Commun., vol. 8, no. 1, p. 642, 2017 (cit. on p. 2).
- [59] S. Blügel, H. Akai, R. Zeller, and P. H. Dederichs, "Hyperfine fields of 3d and 4d impurities in nickel," *Phys. Rev. B*, vol. 35, pp. 3271–3283, 7 1987 (cit. on pp. 2, 14, 17).
- [60] C. G. Van de Walle and P. E. Blöchl, "First-principles calculations of hyperfine parameters," *Phys. Rev. B*, vol. 47, pp. 4244–4255, 8 1993 (cit. on pp. 2, 14).
- [61] H. Akai, M. Akai, S. Blügel, et al., "Theory of Hyperfine Interactions in Metals," Prog. Theor. Phys. Suppl., vol. 101, pp. 11–77, 1990, ISSN: 0375-9687 (cit. on pp. 2, 14, 28).
- [62] G. A. Webb, Modern Magnetic Resonance: Part 1: Applications in Chemistry, Biological and Marine Sciences, Part 2: Applications in Medical and Pharmaceutical Sciences, Part 3: Applications in Materials Science and Food Science. Springer Science & Business Media, 2007 (cit. on pp. 2, 25, 45).

- [63] T. Choi, W. Paul, S. Rolf-Pissarczyk, et al., "Atomic-scale sensing of the magnetic dipolar field from single atoms," Nat. Nanotechnol., vol. 12, pp. 420–424, 2017, ISSN: 1748-3387 (cit. on pp. 2, 25, 29).
- [64] P. Willke, W. Paul, F. D. Natterer, et al., "Probing quantum coherence in single-atom electron spin resonance," Sci. Adv., vol. 4, no. 2, eaaq1543, 2018 (cit. on pp. 2, 25, 29).
- [65] Y. Bae, K. Yang, P. Willke, T. Choi, A. J. Heinrich, and C. P. Lutz, "Enhanced quantum coherence in exchange coupled spins via singlet-triplet transitions," Sci. Adv., vol. 4, no. 11, eaau4159, 2018 (cit. on pp. 2, 25, 29).
- [66] P. Willke, A. Singha, X. Zhang, et al., "Tuning single-atom electron spin resonance in a vector magnetic field," Nano Lett., vol. 19, no. 11, pp. 8201–8206, 2019 (cit. on pp. 2, 25, 29).
- [67] T. S. Seifert, S. Kovarik, D. M. Juraschek, N. A. Spaldin, P. Gambardella, and S. Stepanow, "Longitudinal and transverse electron paramagnetic resonance in a scanning tunneling microscope," *Sci. Adv.*, vol. 6, no. 40, eabc5511, 2020 (cit. on pp. 2, 3, 25, 29).
- [68] T. S. Seifert, S. Kovarik, P. Gambardella, and S. Stepanow, "Accurate measurement of atomic magnetic moments by minimizing the tip magnetic field in stm-based electron paramagnetic resonance," *Phys. Rev. Research*, vol. 3, p. 043 185, 4 2021 (cit. on pp. 2, 25).
- [69] Y. Manassen, R. Hamers, J. Demuth, and A. Castellano Jr, "Direct observation of the precession of individual paramagnetic spins on oxidized silicon surfaces," *Physical review letters*, vol. 62, no. 21, p. 2531, 1989 (cit. on p. 2).
- [70] Y. Manassen, "Scanning probe microscopy and magnetic resonance," *Advanced Materials*, vol. 6, no. 5, pp. 401–404, 1994 (cit. on p. 2).
- [71] A. V. Balatsky, M. Nishijima, and Y. Manassen, "Electron spin resonance-scanning tunneling microscopy," Adv. Phys., vol. 61, no. 2, pp. 117–152, 2012 (cit. on pp. 2, 25).
- [72] Y. Manassen, M. Averbukh, and M. Morgenstern, "Analyzing multiple encounter as a possible origin of electron spin resonance signals in scanning tunneling microscopy on si (111) featuring c and o defects," *Surface science*, vol. 623, pp. 47–54, 2014 (cit. on p. 2).
- [73] A. Caso, B. Horovitz, and L. Arrachea, "Model for electron spin resonance in stm noise," *Phys. Rev. B*, vol. 89, p. 075412, 7 2014 (cit. on pp. 3, 25).
- [74] P. Berggren and J. Fransson, "Electron paramagnetic resonance of single magnetic moment on a surface," Sci. Rep., vol. 6, p. 25584, 2016, ISSN: 2045-2322 (cit. on pp. 3, 25).
- [75] J. L. Lado, A. Ferrón, and J. Fernández-Rossier, "Exchange mechanism for electron paramagnetic resonance of individual adatoms," *Phys. Rev. B*, vol. 96, p. 205 420, 20 2017 (cit. on pp. 3, 25).

- [76] J. Reina Gálvez, C. Wolf, F. Delgado, and N. Lorente, "Cotunneling mechanism for all-electrical electron spin resonance of single adsorbed atoms," *Phys. Rev.* B, vol. 100, p. 035 411, 3 2019 (cit. on pp. 3, 25).
- [77] C. Wolf, F. Delgado, J. Reina, and N. Lorente, "Efficient ab initio multiplet calculations for magnetic adatoms on MgO," J. Phys. Chem. A., vol. 124, no. 11, pp. 2318–2327, 2020 (cit. on pp. 3, 25).
- [78] F. Delgado and N. Lorente, "A theoretical review on the single-impurity electron spin resonance on surfaces," *Progress in Surface Science*, p. 100625, 2021 (cit. on pp. 3, 25).
- [79] P. Hohenberg and W. Kohn, "Inhomogeneous electron gas," Phys. Rev., vol. 136, B864–B871, 3B Nov. 1964 (cit. on pp. 4, 6–8).
- [80] W. Kohn and L. J. Sham, "Self-consistent equations including exchange and correlation effects," *Phys. Rev.*, vol. 140, A1133–A1138, 4A Nov. 1965 (cit. on pp. 4, 6, 8, 10).
- [81] P. A. M. Dirac, "The quantum theory of the electron," Proceedings of the Royal Society of London. Series A, Containing Papers of a Mathematical and Physical Character, vol. 117, no. 778, pp. 610–624, 1928 (cit. on pp. 4, 14, 17).
- [82] P. A. M. Dirac, "The quantum theory of the electron. part ii," *Proceedings of the Royal Society of London. Series A, Containing Papers of a Mathematical and Physical Character*, vol. 118, no. 779, pp. 351–361, 1928 (cit. on pp. 4, 14, 17).
- [83] J. C. Villanueva, "How many atoms are there in the universe," *Universe Today*, vol. 30, 2009 (cit. on p. 6).
- [84] D. Hartree, "Mathematical proceedings of the cambridge philosophical society," 3, Cambridge University Press, vol. 24, 1928, pp. 426–437 (cit. on p. 6).
- [85] V. Fock, "Approach method for solving the quantum mechanical multibody problem," *journal for physics*, vol. 61, no. 1, pp. 126–148, 1930 (cit. on p. 6).
- [86] C. Møller and M. S. Plesset, "Note on an approximation treatment for many-electron systems," *Physical review*, vol. 46, no. 7, p. 618, 1934 (cit. on p. 6).
- [87] A. Szabo and N. S. Ostlund, Modern quantum chemistry: introduction to advanced electronic structure theory. Courier Corporation, 2012 (cit. on p. 6).
- [88] J. Čížek, "On the correlation problem in atomic and molecular systems. calculation of wavefunction components in ursell-type expansion using quantum-field theoretical methods," *The Journal of Chemical Physics*, vol. 45, no. 11, pp. 4256–4266, 1966 (cit. on p. 6).
- [89] G. Czycholl, Theoretical solid state physics: from classical models to modern research topics. Springer-Verlag, 2007 (cit. on p. 6).
- [90] M. Born and R. Oppenheimer, "Zur quantentheorie der molekeln," *Annalen der Physik*, vol. 389, no. 20, pp. 457–484, 1927 (cit. on p. 7).

- [91] U. von Barth and L. Hedin, "A local exchange-correlation potential for the spin polarized case. i," *Journal of Physics C: Solid State Physics*, vol. 5, no. 13, pp. 1629–1642, Jul. 1972 (cit. on p. 9).
- [92] R. Parr and W. Yang, "International series of monographs on chemistry 16," Oxford University Press, New York, Clarendon Press, Oxford, 1989 (cit. on p. 9).
- [93] O. Gunnarsson and B. I. Lundqvist, Phys. Rev. B, vol. 13, pp. 4274–4298, 10 May 1976 (cit. on p. 10).
- [94] D. Wortmann, S. Heinze, P. Kurz, G. Bihlmayer, and S. Blügel, "Resolving complex atomic-scale spin structures by spin-polarized scanning tunneling microscopy," *Physical review letters*, vol. 86, no. 18, p. 4132, 2001 (cit. on p. 10).
- [95] P. Kurz, F. Förster, L. Nordström, G. Bihlmayer, and S. Blügel, "Ab initio treatment of noncollinear magnets with the full-potential linearized augmented plane wave method," *Physical Review B*, vol. 69, no. 2, p. 024415, 2004 (cit. on p. 10).
- [96] S. H. Vosko, L. Wilk, and M. Nusair, "Accurate spin-dependent electron liquid correlation energies for local spin density calculations: A critical analysis," *Canadian Journal of physics*, vol. 58, no. 8, pp. 1200–1211, 1980 (cit. on p. 10).
- [97] P. A. Dirac, "Mathematical proceedings of the cambridge philosophical society," 3, Cambridge University Press, vol. 26, 1930, pp. 376–385 (cit. on p. 10).
- [98] G. Ortiz and P. Ballone, "Correlation energy, structure factor, radial distribution function, and momentum distribution of the spin-polarized uniform electron gas," *Phys. Rev. B*, vol. 50, pp. 1391–1405, 3 Jul. 1994 (cit. on p. 10).
- [99] K. Capelle, "A bird's-eye view of density-functional theory," *Brazilian journal of physics*, vol. 36, pp. 1318–1343, 2006 (cit. on p. 11).
- [100] J. P. Perdew and A. Zunger, "Self-interaction correction to density-functional approximations for many-electron systems," *Phys. Rev. B*, vol. 23, pp. 5048– 5079, 10 May 1981 (cit. on pp. 11, 60).
- [101] A. D. Becke, "Density-functional exchange-energy approximation with correct asymptotic behavior," *Phys. Rev. A*, vol. 38, pp. 3098–3100, 6 Sep. 1988 (cit. on p. 11).
- [102] L. J. Sham, "Computational methods in band theory: Proceedings of a conference held at the ibm thomas j. watson research center, yorktown heights, new york, may 14–15, 1970, under the joint sponsorship of ibm and the american physical society," in P. M. Marcus, J. F. Janak, and A. R. Williams, Eds. Boston, MA: Springer US, 1971, pp. 458–468, ISBN: 978-1-4684-1890-3 (cit. on p. 11).
- [103] R. O. Jones, "Density functional theory: Its origins, rise to prominence, and future," *Rev. Mod. Phys.*, vol. 87, pp. 897–923, 3 Aug. 2015 (cit. on p. 11).

- [104] J. P. Perdew, K. Burke, and M. Ernzerhof, "Generalized gradient approximation made simple," *Phys. Rev. Lett.*, vol. 77, pp. 3865–3868, 18 1996 (cit. on pp. 11, 26).
- [105] V. I. Anisimov, J. Zaanen, and O. K. Andersen, "Band theory and mott insulators: Hubbard u instead of stoner i," *Physical Review B*, vol. 44, no. 3, p. 943, 1991 (cit. on pp. 11, 12).
- [106] V. I. Anisimov, F. Aryasetiawan, and A. Lichtenstein, "First-principles calculations of the electronic structure and spectra of strongly correlated systems: The lda+ u method," *Journal of Physics: Condensed Matter*, vol. 9, no. 4, p. 767, 1997 (cit. on p. 11).
- [107] S. L. Dudarev, G. A. Botton, S. Y. Savrasov, C. J. Humphreys, and A. P. Sutton, "Electron-energy-loss spectra and the structural stability of nickel oxide: An LSda+u study," *Phys. Rev. B*, vol. 57, pp. 1505–1509, 3 1998 (cit. on pp. 11, 12, 26).
- [108] A. G. Petukhov, I. I. Mazin, L. Chioncel, and A. I. Lichtenstein, "Correlated metals and the LDA + U method," *Phys. Rev. B*, vol. 67, p. 153106, 15 Apr. 2003 (cit. on p. 11).
- [109] M. Cococcioni and S. de Gironcoli, "Linear response approach to the calculation of the effective interaction parameters in the LDA + U method," *Phys. Rev. B*, vol. 71, p. 035 105, 3 2005 (cit. on pp. 11, 12, 26).
- [110] A. Rohrbach, J. Hafner, and G. Kresse, "Electronic correlation effects in transition-metal sulfides," *Journal of Physics: Condensed Matter*, vol. 15, no. 6, p. 979, 2003 (cit. on p. 11).
- [111] N. F. Mott, "The basis of the electron theory of metals, with special reference to the transition metals," *Proceedings of the Physical Society. Section A*, vol. 62, no. 7, p. 416, 1949 (cit. on p. 12).
- [112] J. H. de Boer and E. J. Verwey, "Semi-conductors with partially and with completely filled 3d-lattice bands," *Proceedings of the Physical Society (1926-1948)*, vol. 49, no. 4S, p. 59, 1937 (cit. on p. 12).
- [113] A. Oleś, "Correlation effects in the cohesion and magnetic properties of transition metals," *Physical Review B*, vol. 23, no. 1, p. 271, 1981 (cit. on p. 12).
- [114] A. Oles and G. Stollhoff, "Correlation effects in ferromagnetism of transition metals," *Physical Review B*, vol. 29, no. 1, p. 314, 1984 (cit. on p. 12).
- [115] J. Hubbard, "Electron correlations in narrow energy bands," *Proceedings of the Royal Society of London. Series A. Mathematical and Physical Sciences*, vol. 276, no. 1365, pp. 238–257, 1963 (cit. on p. 12).
- [116] J. Hubbard, "Electron correlations in narrow energy bands. ii. the degenerate band case," *Proceedings of the Royal Society of London. Series A. Mathematical and Physical Sciences*, vol. 277, no. 1369, pp. 237–259, 1964 (cit. on p. 12).

- [117] J. Hubbard, "Electron correlations in narrow energy bands iii. an improved solution," *Proceedings of the Royal Society of London. Series A. Mathematical and Physical Sciences*, vol. 281, no. 1386, pp. 401–419, 1964 (cit. on p. 12).
- [118] V. I. Anisimov, I. Solovyev, M. Korotin, M. Czyżyk, and G. Sawatzky, "Density-functional theory and nio photoemission spectra," *Physical Review B*, vol. 48, no. 23, p. 16929, 1993 (cit. on p. 12).
- [119] I. Solovyev, P. Dederichs, and V. Anisimov, "Corrected atomic limit in the local-density approximation and the electronic structure of d impurities in rb," *Physical Review B*, vol. 50, no. 23, p. 16861, 1994 (cit. on p. 12).
- [120] A. Liechtenstein, V. I. Anisimov, and J. Zaanen, "Density-functional theory and strong interactions: Orbital ordering in mott-hubbard insulators," *Physical Review B*, vol. 52, no. 8, R5467, 1995 (cit. on pp. 12, 60).
- [121] F. Bloch, "Über die quantenmechanik der elektronen in kristallgittern," Zeitschrift für physik, vol. 52, no. 7, pp. 555–600, 1929 (cit. on p. 12).
- [122] U. Von Barth and C. Gelatt, "Validity of the frozen-core approximation and pseudopotential theory for cohesive energy calculations," *Physical Review B*, vol. 21, no. 6, p. 2222, 1980 (cit. on pp. 13, 15).
- [123] W. E. Pickett, "Pseudopotential methods in condensed matter applications," Computer Physics Reports, vol. 9, no. 3, pp. 115–197, 1989 (cit. on pp. 13, 15).
- [124] P. Schwerdtfeger, "The pseudopotential approximation in electronic structure theory," *ChemPhysChem*, vol. 12, no. 17, pp. 3143–3155, 2011 (cit. on pp. 13, 15).
- [125] D. Hamann, M. Schlüter, and C. Chiang, "Norm-conserving pseudopotentials," *Physical Review Letters*, vol. 43, no. 20, p. 1494, 1979 (cit. on p. 13).
- [126] G. B. Bachelet, D. R. Hamann, and M. Schlüter, "Pseudopotentials that work: From h to pu," *Physical Review B*, vol. 26, no. 8, p. 4199, 1982 (cit. on p. 13).
- [127] D. Vanderbilt, "Soft self-consistent pseudopotentials in a generalized eigenvalue formalism," *Physical review B*, vol. 41, no. 11, p. 7892, 1990 (cit. on pp. 13, 45, 60).
- [128] P. E. Blöchl, "Projector augmented-wave method," *Physical review B*, vol. 50, no. 24, p. 17953, 1994 (cit. on p. 13).
- [129] G. Kresse and D. Joubert, "From ultrasoft pseudopotentials to the projector augmented-wave method," *Physical review b*, vol. 59, no. 3, p. 1758, 1999 (cit. on p. 13).
- [130] E. Rashba, "Properties of semiconductors with an extremum loop. i. cyclotron and combinational resonance in a magnetic field perpendicular to the plane of the loop," Sov. Phys.-Solid State, vol. 2, p. 1109, 1960 (cit. on p. 14).
- [131] Y. A. Bychkov and E. I. Rashba, "Oscillatory effects and the magnetic susceptibility of carriers in inversion layers," *Journal of physics C: Solid state physics*, vol. 17, no. 33, p. 6039, 1984 (cit. on p. 14).

- [132] Y. A. Bychkov and É. I. Rashba, "Properties of a 2d electron gas with lifted spectral degeneracy," *JETP lett*, vol. 39, no. 2, p. 78, 1984 (cit. on p. 14).
- [133] R. M. Martin, *Electronic structure: basic theory and practical methods*. Cambridge university press, 2020 (cit. on p. 14).
- [134] P. Strange, Relativistic Quantum Mechanics: with applications in condensed matter and atomic physics. Cambridge University Press, 1998 (cit. on p. 14).
- [135] M. Weissbluth, Atoms and molecules. Elsevier, 2012 (cit. on pp. 14, 17, 19).
- [136] D. Koelling and B. Harmon, "A technique for relativistic spin-polarised calculations," *Journal of Physics C: Solid State Physics*, vol. 10, no. 16, p. 3107, 1977 (cit. on p. 14).
- [137] A. MacDonald, W. Picket, and D. Koelling, "A linearised relativistic augmented-plane-wave method utilising approximate pure spin basis functions," *Journal of Physics C: Solid State Physics*, vol. 13, no. 14, p. 2675, 1980 (cit. on p. 14).
- [138] P. Giannozzi, S. Baroni, N. Bonini, et al., "Quantum espresso: A modular and open-source software project for quantum simulations of materials," J. Phys.: Condens. Matter, vol. 21, no. 39, p. 395 502, 2009 (cit. on pp. 15, 25).
- [139] P. Giannozzi, O. Andreussi, T. Brumme, et al., "Advanced capabilities for materials modelling with quantum ESPRESSO," J. Phys.: Condens. Matter, vol. 29, no. 46, p. 465 901, 2017 (cit. on pp. 15, 25).
- [140] P. Giannozzi, O. Baseggio, P. Bonfà, et al., "Quantum espresso toward the exascale," *The Journal of chemical physics*, vol. 152, no. 15, p. 154 105, 2020 (cit. on pp. 15, 25).
- [141] A. D. Corso, "Pseudopotentials periodic table: From h to pu," *Comput. Mater. Sci.*, vol. 95, pp. 337–350, 2014, ISSN: 0927-0256 (cit. on pp. 15, 26).
- [142] A. Dal Corso and A. M. Conte, "Spin-orbit coupling with ultrasoft pseudopotentials: Application to au and pt," *Physical Review B*, vol. 71, no. 11, p. 115 106, 2005 (cit. on pp. 15, 60, 61).
- [143] A. Dal Corso, "Pseudopotentials periodic table: From h to pu," Computational Materials Science, vol. 95, pp. 337–350, 2014 (cit. on pp. 15, 60, 61).
- [144] C. J. Pickard and F. Mauri, "All-electron magnetic response with pseudopotentials: Nmr chemical shifts," *Phys. Rev. B*, vol. 63, p. 245 101, 24 2001 (cit. on pp. 15, 26).
- [145] G. Breit and F. Doermann, "The hyperfine structure of s and p terms of two electron atoms with special reference to li+," *Physical Review*, vol. 36, no. 12, p. 1732, 1930 (cit. on p. 17).
- [146] A. M. Stoneham, Theory of defects in solids: electronic structure of defects in insulators and semiconductors. Oxford University Press, 2001 (cit. on p. 17).
- [147] S. Blinder, "The hyperfine interaction hamiltonian," *Journal of Molecular Spectroscopy*, vol. 5, no. 1-6, pp. 17–23, 1961 (cit. on p. 17).

- [148] W. A. Coish, "Spins in quantum dots: Hyperfine interaction, transport, and coherent control," Ph.D. dissertation, University of Basel, 2008 (cit. on p. 17).
- [149] M. Yulikov, M. Sterrer, M. Heyde, et al., "Binding of single gold atoms on thin mgo(001) films," Phys. Rev. Lett., vol. 96, p. 146 804, 14 2006 (cit. on pp. 22, 26, 71).
- [150] E. D. Hedegård, J. Kongsted, and S. P. A. Sauer, "Validating and analyzing epr hyperfine coupling constants with density functional theory," *J. Chem. Theory Comput*, vol. 9, no. 5, pp. 2380–2388, 2013 (cit. on pp. 22, 26, 40, 57, 71).
- [151] S. Shehada, M. dos Santos Dias, F. S. M. Guimarães, M. Abusaa, and S. Lounis, "Trends in the hyperfine interactions of magnetic adatoms on thin insulating layers," *npj Computational Materials*, vol. 7, no. 1, pp. 1–10, 2021 (cit. on pp. 24, 45, 49).
- [152] P. E. Blöchl, "Projector augmented-wave method," Phys. Rev. B, vol. 50, pp. 17953–17979, 24 1994 (cit. on p. 26).
- [153] M. Boiocchi, F. Caucia, M. Merli, D. Prella, and L. Ungaretti, "Crystal-chemical reasons for the immiscibility of periclase and wustite under lithospheric p, t conditions," Eur. J. Mineral., vol. 13, no. 5, pp. 871–881, 2001 (cit. on p. 26).
- [154] P. Fontana, J. Schefer, and D. Pettit, "Characterization of sodium chloride crystals grown in microgravity," J. Cryst. Growth, vol. 324, no. 1, pp. 207– 211, 2011 (cit. on p. 26).
- [155] B. S. Rao and S. Sanyal, "Structural and elastic properties of sodium halides at high pressure," *Phys. Rev. B*, vol. 42, no. 3, p. 1810, 1990 (cit. on p. 26).
- [156] U. Zachwieja and H. Jacobs, "Ammonothermalsynthese von kupfernitrid, cu3n," J. Less. Common. Met., vol. 161, no. 1, pp. 175–184, 1990 (cit. on p. 26).
- [157] J. C. Meyer, A. Chuvilin, G. Algara-Siller, J. Biskupek, and U. Kaiser, "Selective sputtering and atomic resolution imaging of atomically thin boron nitride membranes," *Nano Lett.*, vol. 9, no. 7, pp. 2683–2689, 2009 (cit. on p. 26).
- [158] S. E. Weber, B. K. Rao, P. Jena, et al., "Magnetism of free and supported vanadium clusters," J. Phys.: Condens. Matter, vol. 9, no. 48, pp. 10739– 10748, 1997 (cit. on p. 28).
- [159] A. Markovits, J. C. Paniagua, N. López, C. Minot, and F. Illas, "Adsorption energy and spin state of first-row transition metals adsorbed on mgo(100)," *Phys. Rev. B*, vol. 67, p. 115 417, 11 2003 (cit. on pp. 30, 31).
- [160] K. M. Neyman, C. Inntam, V. A. Nasluzov, R. Kosarev, and N. Rösch, "Adsorption of d-metal atoms on the regular mgo(001) surface: Density functional study of cluster models embedded in an elastic polarizable environment," Appl. Phys. A., vol. 78, no. 6, pp. 823–828, 2004, ISSN: 1432-0630 (cit. on p. 30).

- [161] S. Fernandez, A. Markovits, F. Fuster, and C. Minot, "First row transition metal atom adsorption on defect-free mgo(100) surface," *J. Phys. Chem. C.*, vol. 111, no. 18, pp. 6781–6788, 2007 (cit. on p. 30).
- [162] O. R. Albertini, A. Y. Liu, and B. A. Jones, "Site-dependent magnetism of ni adatoms on mgo/ag(001)," *Phys.Rev.B*, vol. 91, p. 214423, 21 2015 (cit. on p. 31).
- [163] H.-Y. T. Chen, L. Giordano, and G. Pacchioni, "Adsorption properties of two-dimensional nacl: A density functional theory study of the interaction of co, ag, and au atoms with nacl/au (111) ultrathin films," J. Phys. Chem. C., vol. 118, no. 23, pp. 12353–12363, 2014 (cit. on p. 35).
- [164] O. V. Yazyev and A. Pasquarello, "Metal adatoms on graphene and hexagonal boron nitride: Towards rational design of self-assembly templates," *Phys. Rev.* B, vol. 82, p. 045 407, 4 2010 (cit. on p. 39).
- [165] G. Pacchioni, L. Giordano, and M. Baistrocchi, "Charging of metal atoms on ultrathin MgO/Mo(100) films," *Phys. Rev. Lett.*, vol. 94, p. 226 104, 22 2005 (cit. on p. 40).
- [166] M. Sterrer, T. Risse, U. Martinez Pozzoni, et al., "Control of the charge state of metal atoms on thin mgo films," Phys. Rev. Lett., vol. 98, p. 096 107, 9 2007 (cit. on p. 40).
- [167] E. Fernandes, F. Donati, F. Patthey, S. Stavrić, Ž. Šljivančanin, and H. Brune, "Adsorption sites of individual metal atoms on ultrathin mgo(100) films," *Phys. Rev. B*, vol. 96, p. 045 419, 4 2017 (cit. on p. 40).
- [168] M. Munzarová and M. Kaupp, "A critical validation of density functional and coupled-cluster approaches for the calculation of epr hyperfine coupling constants in transition metal complexes," J. Phys. Chem. A., vol. 103, no. 48, pp. 9966–9983, 1999 (cit. on pp. 40, 57).
- [169] S. Shehada, M. dos Santos Dias, M. Abusaa, and S. Lounis, "Interplay of magnetic states and hyperfine fields of iron dimers on mgo (001)," *Journal of Physics: Condensed Matter*, vol. 34, no. 38, p. 385 802, 2022 (cit. on p. 44).
- [170] P. Bertrand, Electron Paramagnetic Resonance Spectroscopy. Springer, 2020 (cit. on p. 45).
- [171] P.-W. Ma and S. L. Dudarev, "Constrained density functional for noncollinear magnetism," *Phys. Rev. B*, vol. 91, p. 054 420, 5 2015 (cit. on pp. 45, 47, 61).
- [172] P. Gambardella, S. Rusponi, M. Veronese, et al., "Giant magnetic anisotropy of single cobalt atoms and nanoparticles," science, vol. 300, no. 5622, pp. 1130–1133, 2003 (cit. on p. 58).
- [173] P. Bło ński, A. Lehnert, S. Dennler, et al., "Magnetocrystalline anisotropy energy of co and fe adatoms on the (111) surfaces of pd and rh," *Phys. Rev. B*, vol. 81, p. 104426, 10 Mar. 2010 (cit. on p. 58).

- [174] F. Donati, Q. Dubout, G. Autès, et al., "Magnetic moment and anisotropy of individual co atoms on graphene," Phys. Rev. Lett., vol. 111, p. 236 801, 23 Dec. 2013 (cit. on p. 58).
- [175] J. Hu and R. Wu, "Giant magnetic anisotropy of transition-metal dimers on defected graphene," *Nano letters*, vol. 14, no. 4, pp. 1853–1858, 2014 (cit. on pp. 58, 59).
- [176] I. Beljakov, V. Meded, F. Symalla, et al., "Spin-crossover and massive anisotropy switching of 5d transition metal atoms on graphene nanoflakes," Nano letters, vol. 14, no. 6, pp. 3364–3368, 2014 (cit. on pp. 58, 59).
- [177] R. Xiao, D. Fritsch, M. D. Kuz'min, et al., "Co dimers on hexagonal carbon rings proposed as subnanometer magnetic storage bits," *Phys. Rev. Lett.*, vol. 103, p. 187 201, 18 Oct. 2009 (cit. on pp. 58, 59).
- [178] A. A. Khajetoorians and J. Wiebe, "Hitting the limit of magnetic anisotropy," *Science*, vol. 344, no. 6187, pp. 976–977, 2014 (cit. on pp. 58, 59).
- [179] X. Ou, H. Wang, F. Fan, Z. Li, and H. Wu, "Giant magnetic anisotropy of co, ru, and os adatoms on mgo (001) surface," *Physical Review Letters*, vol. 115, no. 25, p. 257 201, 2015 (cit. on pp. 59, 65).
- [180] D.-s. Wang, R. Wu, and A. Freeman, "First-principles theory of surface magnetocrystalline anisotropy and the diatomic-pair model," *Physical Review B*, vol. 47, no. 22, p. 14932, 1993 (cit. on p. 63).
- [181] H. Brooks, "Ferromagnetic anisotropy and the itinerant electron model," *Physical Review*, vol. 58, no. 10, p. 909, 1940 (cit. on p. 63).
- [182] P. Bruno, "Tight-binding approach to the orbital magnetic moment and magnetocrystalline anisotropy of transition-metal monolayers," *Physical Review B*, vol. 39, no. 1, p. 865, 1989 (cit. on p. 63).
- [183] D. Dai, H. Xiang, and M.-H. Whangbo, "Effects of spin-orbit coupling on magnetic properties of discrete and extended magnetic systems," *Journal of computational chemistry*, vol. 29, no. 13, pp. 2187–2209, 2008 (cit. on p. 63).
- [184] J. J. Sakurai and E. D. Commins, *Modern quantum mechanics, revised edition*, 1995 (cit. on p. 63).
- [185] Y. Lu, X. Zuo, M. Feng, and T. Zhou, "Magnetic anisotropy in the boron nitride monolayer doped by 3d transitional metal substitutes at boron-site," *Journal of Applied Physics*, vol. 113, no. 17, p. 17C304, 2013 (cit. on p. 63).
- [186] B. Shao, M. Feng, and X. Zuo, "Carrier-dependent magnetic anisotropy of cobalt doped titanium dioxide," *Scientific Reports*, vol. 4, no. 1, pp. 1–6, 2014 (cit. on p. 63).
- [187] G. Van Der Laan, "M2, 3 absorption spectroscopy of 3d transition-metal compounds," *Journal of Physics: Condensed Matter*, vol. 3, no. 38, p. 7443, 1991 (cit. on p. 63).

- [188] F. Donati, M. Pivetta, C. Wolf, et al., "Correlation between electronic configuration and magnetic stability in dysprosium single atom magnets," Nano Letters, vol. 21, no. 19, pp. 8266–8273, 2021 (cit. on p. 75).
- [189] R. Baltic, M. Pivetta, F. Donati, et al., "Superlattice of single atom magnets on graphene," Nano letters, vol. 16, no. 12, pp. 7610–7615, 2016 (cit. on p. 75).
- [190] D. M. Crum, M. Bouhassoune, J. Bouaziz, B. Schweflinghaus, S. Blügel, and S. Lounis, "Perpendicular reading of single confined magnetic skyrmions," Nat. Commun., vol. 6, no. 111, p. 8541, 2015, ISSN: 2041-1723 (cit. on p. 99).
- [191] I. L. Fernandes, M. Bouhassoune, and S. Lounis, "Defect-implantation for the all-electrical detection of non-collinear spin-textures," *Nature Commun.*, vol. 11, no. 1, pp. 1–9, 2020 (cit. on p. 99).
- [192] M. Bouhassoune and S. Lounis, "Friedel oscillations induced by magnetic skyrmions: From scattering properties to all-electrical detection," *Nanomaterials*, vol. 11, no. 1, 2021, ISSN: 2079-4991 (cit. on p. 99).
- [193] I. Lima Fernandes, S. Blügel, and S. Lounis, "Spin-orbit enabled all-electrical readout of chiral spin-textures," *Nature communications*, vol. 13, no. 1, pp. 1–10, 2022 (cit. on p. 99).
- [194] S. Brinker, M. dos Santos Dias, and S. Lounis, "The chiral biquadratic pair interaction," New Journal of Physics, vol. 21, no. 8, p. 083 015, 2019 (cit. on p. 99).
- [195] S. Grytsiuk, J.-P. Hanke, M. Hoffmann, et al., "Topological-chiral magnetic interactions driven by emergent orbital magnetism," *Nature Communications*, vol. 11, no. 1, pp. 1–7, 2020, ISSN: 2041-1723 (cit. on p. 99).
- [196] S. Lounis, "Multiple-scattering approach for multi-spin chiral magnetic interactions: Application to the one- and two-dimensional Rashba electron gas," *New Journal of Physics*, vol. 22, no. 10, p. 103 003, 2020 (cit. on p. 99).
- [197] M. dos Santos Dias, S. Brinker, A. Lászlóffy, et al., "Reply to "comment on 'proper and improper chiral magnetic interactions' "," Phys. Rev. B, vol. 105, p. 026 402, 2 2022 (cit. on p. 99).

Band / Volume 260

Crystal and Magnetic Structure of CrAs under Extreme Conditions

A. Eich (2022), viii, 235 pp ISBN: 978-3-95806-655-7

Band / Volume 261

Applications of transcription factor-based biosensors for strain development and evolutionary engineering

R. G. Stella (2022), x, 128 pp ISBN: 978-3-95806-657-1

Band / Volume 262

Strömungsmechanische Simulation und experimentelle Validierung des kryogenen Wasserstoff-Moderators für die Europäische Spallationsneutronenquelle ESS

Y. Beßler (2022), XXIV, 154, xxxiii pp

ISBN: 978-3-95806-660-1

Band / Volume 263

9th Georgian-German School and Workshop in Basic Science September 12 – 16, 2022 | Kutaisi, Tbilisi | Georgia

A. Kacharava, E. Portius, N. J. Shah, H. Ströher (2022)

ISBN: 978-3-95806-664-9

Band / Volume 264

Self-assembly of Au-Fe₃O₄ dumbbell nanoparticles

N. Nandakumaran (2022), xiv, 234 pp

ISBN: 978-3-95806-666-3

Band / Volume 265

Time-resolved and three-dimensional characterisation of magnetic states in nanoscale materials in the transmission electron microscope

T. Weßels (2023), xx, 211 pp ISBN: 978-3-95806-685-4

Band / Volume 266

Dissecting iron and heme regulatory networks and adaptation to heme stress in *Corynebacterium glutamicum*

A. Krüger (2023), IV, 274 pp ISBN: 978-3-95806-686-1

Band / Volume 267

Morphological and functional characterization of layer 5 neurons in rat medial prefrontal cortex, their synaptic microcircuitry and serotonin modulation

R. Rama (2023), 116 pp ISBN: 978-3-95806-688-5 Band / Volume 268

Magnetic and transport studies of the parent and Fe doped Hexagonal-Mn₃Ge Weyl semimetal

V. Rai (2023), xviii, 156 pp ISBN: 978-3-95806-695-3

Band / Volume 269

The complex inositol metabolism of *Corynebacterium glutamicum* and its application for the production of rare inositols

P. Ramp (2023), VI, 161 pp ISBN: 978-3-95806-699-1

Band / Volume 270

Spin- and orbital-dependent band structure of unconventional topological semimetals

K. Hagiwara (2023), v, 115 pp ISBN: 978-3-95806-701-1

Band / Volume 271

Neutron scattering

Experimental Manuals of the JCNS Laboratory Course held at Forschungszentrum Jülich and at the Heinz-Maier-Leibnitz Zentrum Garching edited by T. Brückel, S. Förster, K. Friese, M. Kruteva, M. Zobel and R. Zorn (2023), ca 150 pp

ISBN: 978-3-95806-705-9

Band / Volume 272

Ab-initio investigation of the interplay between the hyperfine interaction and complex magnetism at the nanoscale

S. R. S. Shehada (2023), ix, xi, 119 pp

ISBN: 978-3-95806-718-9

Weitere Schriften des Verlags im Forschungszentrum Jülich unter http://www.zb1.fz-juelich.de/verlagextern1/index.asp

Schlüsseltechnologien / Key Technologies Band / Volume 272 ISBN 978-3-95806-718-9

